University of Dundee

University of Dundee

DOCTOR OF PHILOSOPHY

Elastic Characterization of ex vivo Human Prostate Tissue Using Vibration Optical Coherence Elastography and Second Harmonic Generation Microscopy

Ling, Yuting

Award date:
2018

Link to publication

General rights
Copyright and moral rights for the publications made accessible in the public portal are retained by the authors and/or other copyright owners and it is a condition of accessing publications that users recognise and abide by the legal requirements associated with these rights.

- Users may download and print one copy of any publication from the public portal for the purpose of private study or research.
- You may not further distribute the material or use it for any profit-making activity or commercial gain
- You may freely distribute the URL identifying the publication in the public portal

Take down policy
If you believe that this document breaches copyright please contact us providing details, and we will remove access to the work immediately and investigate your claim.

Download date: 24. Apr. 2022

University of Dundee

Elastic Characterization of *ex vivo* Human Prostate Tissue Using Vibration Optical Coherence Elastography and Second Harmonic Generation Microscopy

Yuting Ling

June 2018

A thesis submitted for the degree of

Doctor of Philosophy

of University of Dundee

School of Science and Engineering

Table of Contents

List of Figures

List of Tables

List of Abbreviations

AFM	atomic-force microscopy
ANOVA	analysis of variance
ARF	acoustic radiation force
ASAP	atypical small acinar proliferation
BPH	benign prostatic hyperplasia
CAHiD	Centre for Anatomy and Human Identification
CT	computerised tomography
DRE	digital rectal examination
DWE	diffusion-weighted image
EAU	European Association of Urology
ECM	extracellular matrix
ERSPC	European Randomized Study of Screening for Prostate Cancer
FD-OCT	frequency domain optical coherence tomography
FFT	fast Fourier transform
FN	false negative
FP	false positive
FT-SHG	Fourier transform second harmonic generation
FWHM	full width at half maximum
H&E	haematoxylin and eosin
ISUP	International Society of Urological Pathology
MRE	magnetic resonance elastography
MRI	magnetic resonance imaging
NA	numerical aperture
NBF	neutral buffered formalin
NHS	National Health Service
NPV	negative predictive value
OCE	optical coherence elastography
OCT	optical coherence tomography
PCa	prostate cancer
PCUK	Prostate Cancer UK
PCRMP	Prostate Cancer Risk Management Programme
PhS-OCT	phase sensitive optical coherence tomography
PIN	prostatic intraepithelial neoplasia

PLCO	Prostate, Lung, Colorectal and Ovarian
PMT	photomultiplier
PPV	positive predictive value
PR	radical prostatectomy
ProtecT	Prostate Testing for Cancer and Treatment
PSA	prostate-specific antigen
ROC	Receiver operating characteristic
ROI	regions of interest
RP	radical prostatectomy
SAW	surface acoustic wave
SD-OCT	spectral domain optical coherence tomography
SE	strain elastography
SHG	second harmonic generation
SEM	electron microscopy
SLD	superluminecent Diode
SMC	smooth muscle cells
SNR	signal to noise ratio
SW	shear wave
SWE	shear wave elastography
TACS	tumour-associated collagen signatures
TAM	tumour associated macrophages
TD-OCT	time domain optical coherence tomography
TE	transient elastography
THG	third harmonic generation
TN	true negative
TP	true positive
TRUS	trans-rectal ultrasound
US	ultrasound

Acknowledgements

This research journey would have been impossible without the motivation and support that I received from many brilliant people. It has been an unforgettable challenge and an amazing experience doing my PhD and I thank them wholeheartedly.

First and foremost, I would like to express my sincere gratitude to my enthusiastic supervisor Professor Zhihong Huang, who took a chance on me as an intern in her Optical Coherence Elastography (OCE) Lab that led to a PhD. Zhihong, thank you for having faith in me for the interdisciplinary research, even though I came with a background in biology. I especially thank Zhihong for giving me so many wonderful opportunities, for her continuous support and encouragement, and for her tremendous guidance throughout my PhD study and related research.

I am profoundly grateful to Dr Chunhui Li, for introducing me to this exciting field of research, for being a fantastic mentor and supervisor, and for all the support and encouragement she gave me. Without her faith in my lab work and constant feedback, this PhD work would not have been achieved. Many thanks to Chunhui for always being there for me during various stages of my PhD and related research. I feel privileged to work with a person like her in my life.

My special words of thanks should also go to Professor Ghulam Nabi, especially for being so dedicated to his role as my clinical supervisor, and for sharing his invaluable clinical experience on prostate cancer as a urological surgeon. His continuous guidance and immense knowledge has always been my inspiration in this interdisciplinary research.

Many thanks also to Dr David McGloin. With his guidance, I attended SUPA Graduate School especially courses for technical training and professional development during the first year of my PhD. These courses and workshops equipped me with the academic skills for the start of research across biology, physics, statistics, and writing. I am especially grateful to David for his encouragement, advice and supervisory role for my PhD study.

I gratefully acknowledge the funding received towards my PhD from the Scottish Universities Physics Alliance (SUPA) PhD studentship. I also greatly appreciate the grants from Prostate Cancer UK (PCUK) for funding this project.

My deep appreciation goes to my fellow lab mates for the days we were working in the labs and for all the fun we had together. I am especially grateful to Dr Guangying Guan for the continuous assistance in the performance maintenance and optimisation of our

OCE systems. To Simian, Cheng, Scott, Kairui, Nhan, Shaozhen, Catherine, Naief, Ying-Ting, and Xiaoxi, thank you for the excellent work and valuable companionship that made an invaluable contribution towards my PhD study. A big thank you to the collaborators: Dr Roos Eisma, Ms Robyn Duncan, Dr Jeffrey Huang, and Professor Ruikang Wang, for the support received through the collaborative work.

Special thanks to Dr Stephen Lang for his histopathological assistance throughout the clinical study and for the use of the microscope in the Department of Pathology (Ninewells Hospital and Medical School), to Dr Paul Appleton for his valuable input and patience while I was utilizing the multiphoton microscope in the Dundee Imaging Facility (School of Life Sciences), to Dr Sharon King for the use of the digital slide scanner in the Tayside Tissue Bank (Ninewells Hospital and Medical School), and to Mr Patrick Carena, Mr Campbell Kevin, and Mr Duncan Kirkcaldy in Medical Physics (Ninewells Hospital and Medical School) for the efforts in helping build a clinical friendly OCE system.

Thank you to the lovely nurses, clinicians, and pathologists who have contributed to this study in Ninewells Hospital. Most importantly, I want to express our sincere gratitude to the patients who consented to participate in this clinical study. Without their understanding and precious support it would not be possible to conduct this research. I delicate this thesis to them.

To all my dear friends, thank you for supporting me through this entire research journey, for cheering me up when I was upset, and for being so helpful in numerous ways. Special thanks to my friends in Dundee, Wendy, Jenny, Kuhn, Fiona, Yuanhao, Yiming, Chenlin, Tingyi, Valerie, Rachel, Anu, Markus, Keith, Brogan, Yan, Jinjiang, Duo, Mingkai, Yubo, Guan, Shengli, Panpan and many more for making me feel so welcome and warm here. Their timely help and friendship shall always be remembered.

Finally, I am indebted to my family for always believing in me and encouraging me to peruse my dreams. Heartfelt thanks goes to my Mum and Dad for always teaching me to stay positive and for supporting me spiritually throughout writing this thesis and my life in general. To a very special friend of mine, my husband, Kanheng, thank you for always being with me during the happy and hard moments, for reminding me to keep smile and be brave, and also for being an incredible lab mate. I greatly value his care for me and deeply appreciate his contribution to our family. My deep appreciation also goes to my mother in law and father in law for their everlasting love and care. Thank you for making me feel so beloved. I owe my deepest gratitude to them all.

Declaration

I, Yuting Ling, hereby declare that I am the author of this thesis; that I have consulted all references cited; that I have done all the work recorded by this thesis; and that it has not been previously accepted for a higher degree.

Yuting Ling

Statement

This is to certify that Yuting Ling has done this research under my supervision and that she has fulfilled the conditions of Ordinance 39 of the University of Dundee, so that she is qualified to submit for the Degree of Doctor of Philosophy.

Professor Zhihong Huang

Copyright

Attention is drawn to the fact that copyright of this thesis rests with its author. This copy of the thesis has been supplied on the condition that anyone who consults it is understood to recognise that its copyright rests with the author and that no quotation from this thesis and no information derived from it may be published without the prior written consent of the author.

This thesis may not be consulted, photocopied or lent by any library without the permission of the author for a period of three years from the date of acceptance of the thesis.

Abstract

Prostate cancer (PCa), the most common cancer in men across the UK, is a multifocal disease with characteristic heterogeneity and foci that can range from low-grade indolent to aggressive disease. In current clinical care, the well-established diagnosis for PCa is trans-rectal ultrasound (TRUS) guided biopsies. The TRUS procedure follows by the Gleason scoring that usually requires the expertise of a trained histopathologist. However, an inter-observer variation exists between two histopathologists besides a large discrepancy existing on initial biopsy and after the final radical prostatectomy. Therefore, a reliable diagnosis is of high demand to make an optimal decision for PCa treatment. This research work aims to apply two emerging optical imaging modalities to quantitatively evaluate the degree of malignancy.

This research thesis presents the vibration optical coherence elastography (OCE) to quantify the tissue stiffness on a microscopic scale. A feasibility study of ten patients suspected with PCa was designed to scan TRUS guided biopsies with the vibration OCE. Meanwhile, the effect of fixatives on the tissue stiffness was studied with five different tissues preserved in the fixatives along a controlled timeline. A subsequent clinical study involving 60 more patients was conducted to follow the feasibility study, which leads to a large clinical study containing a total of 840 core biopsies. Additionally, the second harmonic generation (SHG) microscopy focused on the cells and surrounding matrix within the prostate tissue. The SHG study with 42 core biopsies was intended to investigate the reason of stiffness increase of the cancerous tissue in the prostate.

The experimental results indicates that the vibration OCE is capable to provide 2D and 3D high-resolution elastogram of biopsies with different malignancies. Moreover, a high diagnostic accuracy of differentiating malignant biopsies from benign ones is confirmed, as well as a significant difference in Young's modulus of biopsies of different Gleason scores. For SHG, distinct patterns of collagen distribution are shown for PCa of different Gleason scores, along with a ratio of anisotropic to isotropic (A: I ratio) that correlates with the disease aggressiveness. To sum up, the two techniques described in this research thesis are complementary, where one depicts the stiffness of prostate tissues and the other illustrates the orientation of collagen structure around the cancerous lesion. With further development, these approaches may help *in vivo* diagnosis of PCa quantitatively and characterise grade of cancer as well.

Chapter 1. Introduction

Prostate adenocarcinoma (PCa) is the most common cancer in men in the UK. In routine clinical care, PCa is suspected if men have a raised serum prostate-specific antigen (PSA) level and/or abnormal digital rectal examination (DRE). Conventional ultrasound is a popular clinical imaging technique for lesion anatomy based on the acoustic properties of soft tissues, but many soft tissues can share similar ultrasonic echogenicity. In prostate ultrasound imaging, trans-rectal ultrasound (TRUS) guided biopsy is already in use clinically around the world to guide prostate biopsies. Besides that it is always a frightening and painful procedure for the patients, tumours of prostate may be invisible or barely invisible in standard ultrasound examinations. The sensitivity and specificity in detecting PCa is about 40-50% for conventional TRUS B-mode imaging [1]. This leads to unreliable assessment of the tumour volume [2] and cancer staging [3, 4].

The cancer staging is usually confirmed by the histopathologic verification under microscope using Gleason scoring system [5] as a gold standard. The scoring method is largely relied on the knowledge and experience of the histopathologists. Generally, a higher Gleason score means a more aggressive tumour and a worse prognosis. Notwithstanding an inter-observer variation exists between two histopathologists besides a large discrepancy existing on initial biopsy and after the final radical prostatectomy (RP). Cohen *et al*. [3] conducted a meta-analysis of 14839 patients worldwide, who were diagnosed of PCa with TRUS biopsy and then underwent RP. It was found that only 58% of the patients in whom the RP grade was accurately predicted. In addition, it is controversial about the sensitivity and specificity of the technique, as well as associated risks of overdiagnosis and overtreatment. Therefore, a quantitative diagnosis is of high demand to make an optimal decision for PCa treatment.

Many soft tissues can share similar echogenicity and intensity in ultrasound and magnetic resonance imaging (MRI), but they may have different mechanical properties. The differing elasticity of soft tissue has been an established practice for centuries to differentiate healthy from diseased tissue, especially in breast and prostate tissue. PCa was traditionally diagnosed with DRE of the prostate by feeling the stiffness alteration in the prostate. For the establishment of a quantitative diagnosis using the mechanical properties of the prostate, a direct mechanical evaluation of prostate elasticity was first investigated by Krouskop *et al*. [6] with displacement loading experiments. It was found

that tissue from PCa has a measurable elevated Young's modulus compared with the normal prostate glandular tissue. Elastography enables deeper tissue elasticity imaging based on the assumption that soft tissue is a linear elastic solid with isotropic mechanical properties [7, 8]. Ultrasound elastography has become a commonly used approach for clinical elasticity imaging [9]. However, it depends largely on the performing skills of the operator. Moreover, many cancer foci in the prostate gland has very small size less than 1 mm [10], whilst the spatial scales of current elastography techniques limit the ability to identify such small lesions. Alternatively, optical imaging techniques can break the limit of ultrasound and MRI to realize micro-scale resolution [11].

Optical coherence tomography (OCT) is an emerging optical imaging technique which works similar to ultrasound except that OCT uses near-infrared light rather than acoustical waves. OCT enables micro-scale spatial resolution and millimetre-scale imaging depth [11]. Elastography with OCT to detect tissue deformation is termed as optical coherence elastography (OCE). Phase-sensitive (PhS) method has been widely utilized to detect the displacement owing to a large displacement dynamic range. To generate mechanical stimulation, the compression method is the most commonly used one to implement in OCE. However, the lack of direct measurement of the absolute elasticity has limited its potential clinical applications. Both surface acoustic wave (SAW) and shear wave (SW) method can provide quantitative evaluation of tissue stiffness, but the lateral resolution is lower due to the long wavelength of the mechanical wave.

In this study, a novel vibration OCE method was adapted from Guan *et al*.[12] by combining PhS-OCE configuration with a magnetic shaker. This method was capable to provide quantitative Young's modulus of biological tissues with a high spatial resolution. Thus it might be suitable for the early PCa detection. Therefore, the vibration OCE method was applied in a large clinical study to evaluate the degree of malignancy in the men suspected with PCa. Moreover, it is not well understood about the stiffness change of the TRUS biopsy tissues embedded in the neutral buffered formalin (NBF) in the routine clinical care for PCa patients. Hereby, the effect of fixatives on the tissue stiffness was also studied in this research thesis along a controlled timeline with vibration OCE.

Extracellular matrix (ECM) remodelling is significant in cancer progression with collagen as the dominant structural component providing mechanical strength and flexibility of tissue. A novel technique that can identify and characterize features of the epithelial-stromal microenvironment is of great diagnostic potential and interest. Second harmonic generation (SHG) has been widely used for biomedical researches [14, 18, 22, 25]. In

biological tissues, only non-centrosymmetric structures are capable to emit SHG light, and such structure like collagen which is a main loading component in most tissues. In the normal prostate ECM, collagen type I and type III are the major structural components [5, 6]. In this study, the purpose of using this technique is to investigate the role of collagen in the prostate elasticity change, and possibly in cancer progression.

1.1 Research Aims

The overall objective of this research thesis is to implement two emerging optical imaging modalities to quantitatively evaluate the degree of malignancy. This goal is achieved by the following three aspects of original work.

1. Studying the impact of fixatives on the tissue stiffness using vibration OCE.
2. Estimating the diagnostic accuracy of vibration OCE in detection and grade characterisation of PCa with *ex vivo* prostate biopsies.
3. Investigating the cells and surrounding matrix using SHG microscopy to uncover the relationship between the collagen orientation and the degree of malignancy.

1.2 Structure of Thesis

Chapter 2. Prostate Cancer and Technical Background

This chapter will provide a literature background for this research project. The first part is the introduction of PCa including the gold standard Gleason scoring system and the current diagnostic methods such as the PSA serum test and DRE. In the second part, a brief review is provided on the tissue biomechanics of prostate, theory of elastography, and current elastography techniques in clinical trials to detect prostate disease, namely strain and shear wave elastography. At last, the theory and development of OCT and OCE technique is reviewed. The pros and cons will be compared and summarized for the current OCE methods including SAW, SW and compression elastography.

Chapter 3. Evaluation of Fixative Effects on Tissue Stiffness with Vibration Optical Coherence Elastography

In the case of PCa diagnosis, the TRUS biopsy tissues is deposited in 10% formalin before the histopathological procedure. In this chapter, the effects of tissue preservation (10% formalin and Thiel fluids) on the elastic properties of five different kinds of fresh tissues will be studied. Understanding the effects of storage and preservation conditions on the mechanical properties of soft tissue has both clinical and experimental significance. The system configuration of the vibration OCE will be detailed including the applied parameters and the scanning protocol, as well as the principle of stiffness quantification. Briefly, a magnetic shaker stimulates vibration to the sample and the sample deformation is detected by the PhS OCT. For scanning the sample, the tissue elasticity was measured within a controlled timeline of 6 months. This method is proved to be capable to depict that the formalin solution has an ascending impact on the tissue elasticity, but the elasticity of the tissues in Thiel solution remains almost constant. Meanwhile, it reveals the optimal time for the tissues to achieve full fixation. Therefore, the findings of this chapter forms a basis for performing vibration OCE to evaluate the degree of malignancy using *ex vivo* prostate biopsies embedded in the formalin.

Chapter 4. Elastic Quantification of Biopsies from Men Suspected with Prostate Cancer Using Vibration Optical Coherence Elastography

Chapter 4 describes a large clinical study of implementing vibration OCE to evaluate the degree of malignancy. This study recruited 70 patients suspected with PCa who underwent TRUS biopsy before the histopathological process. Both 2D and 3D scanning was performed on each biopsy with vibration OCE method. The results showed that stiffness of cancer tissue was approximately 57.63% higher than that of benign ones. A high diagnostic accuracy of vibration OCE method is confirmed in the detection and characterisation of PCa. Using histology as a reference standard and 600kPa as a cut-off threshold, the data analysis showed sensitivity and specificity of 89.6% and 99.8% respectively. Furthermore, there is a significant difference noticed in Young's modulus of different Gleason scores estimated by vibration OCE.

Chapter 5. Second Harmonic Generation Imaging of Collagen Orientation in Prostate Biopsies from Men Suspected with Prostate Cancer

In this chapter, the collagen assembly in prostate tissue was investigated with SHG microscopy. It was intended to investigate the reason of stiffness increase of the cancerous tissue in the prostate with a total of 42 core biopsies. A novel technique such as SHG that can identify and characterize features of the epithelial-stromal microenvironment is of great diagnostic potential and interest. The results present the normal area of prostate biopsy with a papillary pattern, while the malignant foci with a reticular pattern. Distinct patterns of collagen distribution were seen for different Gleason grade disease. A parameter (A:I ratio) based on the ratio between anisotropically and isotropically aligned collagen fibres was applied to compute the regularity in collagen fibre orientation. This ratio was found to be correlated with the disease aggressiveness, i.e. the collagen fibres tended to be more oriented/anisotropic when PCa became more aggressive.

Chapter 6. Conclusion and Perspectives

A final summary will draw in this chapter to present the complementary role of these two imaging techniques in identifying PCa and evaluating malignancy. Vibration OCE has been proved to be a potential method of high diagnostic accuracy in depicting the tissue stiffness related to the gold standard. Meanwhile, SHG microscopy has been capable to illustrate the orientation of collagen structure around the cancerous lesion which will be helpful to understand PCa progression. This chapter will also summarise the limitation of this research work and potential future works.

1.3 Publications Arising from This Work

Peer-reviewed journal papers

1. **Yuting Ling**, Chunhui Li, Kanheng Zhou, Guangying Guan, Paul L Appleton, Stephen Lang, David McGloin, Zhihong Huang and Ghulam Nabi. Microscale characterization of prostate biopsies tissues using optical coherence elastography and second harmonic generation imaging. *Laboratory Investigation.* 2017;98:380.

2. **Yuting Ling**, Chunhui Li, Kairui Feng, Scott Palmer, Paul L Appleton, Stephen Lang, David McGloin, Zhihong Huang and Ghulam Nabi. Second harmonic generation (SHG) imaging of cancer heterogeneity in ultrasound guided biopsies of prostate in men suspected with prostate cancer. *J. Biophoton.* 2017 Jun;10(6-7):911-8.

3. **Yuting Ling**, Chunhui Li, Kairui Feng, Robyn Duncan, Roos Eisma, Zhihong Huang and Ghulam Nabi. Effects of fixation and preservation on tissue elastic properties measured by quantitative optical coherence elastography (OCE). *Journal of biomechanics*. 2016 May 3;49(7):1009-15.

4. Chunhui Li, Guangying Guan, **Yuting Ling**, Ying-ting Hsu, Shaozhen Song, Jeffrey T. J. Huang, Stephen Lang, Zhihong Huang and Ghulam Nabi. Detection and characterisation of biopsy tissue using quantitative optical coherence elastography (OCE) in men with suspected prostate cancer. *Cancer letters.* 2015 Feb 1;357(1):121-8.

Conference oral presentations

1. **Yuting Ling**, Chunhui Li, Kanheng Zhou, Guangying Guan, Stephen Lang, David McGloin, Ghulam Nabi and Zhihong Huang. 'Quantitative Assessment of the Mechanical Properties of Prostate Tissue with Optical Coherence Elastography' at SPIE BiOS 'Therapeutics and Diagnostics in Urology 2018', January 27 – February 1, 2018, *San Francisco*, California, USA.
2. **Yuting Ling**, Chunhui Li, Paul L Appleton, Stephen Lang, David McGloin, Zhihong Huang and Ghulam Nabi. 'Evaluation of cancer malignancy in prostate biopsies using second harmonic generation (SHG) microscopy' at BMLA Laser and Aesthetics Conference 2017, May 17-19, 2017, *The Lowry Theatre*, Manchester, UK.
3. **Yuting Ling**, Chunhui Li, Guangying Guan, Ying-ting Hsu, Shaozhen Song, Jeffrey T. J. Huang, Stephen Lang, Zhihong Huang and Ghulam Nabi. 'Detection and

characterization of biopsy tissue using quantitative optical coherence elastography (OCE) in men with suspected prostate cancer' at the Prostate Cancer UK 'Making Progress: Research Network Day', October 23, 2015, *Royal College of Physicians*, London, UK.

Conference poster presentations

1. **Yuting Ling**, Chunhui Li, Kanheng Zhou, Guangying Guan, Stephen Lang, David McGloin, Ghulam Nabi and Zhihong Huang. 'Microstructural Elastographic Characterisation of Prostate Biopsies Tissues using Optical Coherence Elastography' at Photonex Scotland 'Advances in photonic techniques for biomedical sciences', June 14, 2017, *University of Strathclyde*, Glasgow, UK.
2. **Yuting Ling**, Chunhui Li, Kairui Feng, Scott Palmer, Paul L Appleton, Stephen Lang, David McGloin, Ghulam Nabi and Zhihong Huang. 'Characterisation of heterogeneity in prostate biopsies using optical coherence elastography and second harmonic generation microscopy' at 'Biophotonic approaches: From molecules to living systems', August 22-23, 2016, *University of Dundee*, Dundee, UK.
3. **Yuting Ling**, Chunhui Li, Kairui Feng, Scott Palmer, Paul L Appleton, Stephen Lang, David McGloin, Zhihong Huang and Ghulam Nabi. 'Second harmonic generation (SHG) imaging of cancer heterogeneity in ultrasound guided biopsies of prostate in men suspected with prostate cancer' at Photonex Scotland 'Advances in photonic tools and techniques for the life sciences', June 8, 2016, *Heriot-Watt University*, Edinburgh, UK.
4. **Yuting Ling**, Chunhui Li, Guangying Guan, Stephen Lang, David McGloin, Ghulam Nabi and Zhihong Huang. 'Quantitative optical coherence elastography – current applications in clinical and biomedical research' at the 6th SU2P Annual Symposium, March 23-24, 2015, *University of St. Andrews*, St. Andrews, UK.

Chapter 2. Prostate Cancer and Technical Background

This chapter aims at providing a literature background for this research project using optical coherence elastography to characterize the mechanical properties of prostate biopsies. It will be divided into several sections below.

1. The first section starts with the introduction of prostate cancer from the histological and pathological point of view including the gold standard Gleason scoring system, and followed by comparing the advantage and disadvantage of the current diagnostic methods. The lack of a reliable diagnostic method was highlighted as a clinical evidence and triggers the motivation of this study that the employment of elastography might be a potential diagnostic technique.

2. Prostate elastography intends to achieve a more accurate diagnosis objectively by providing quantitative mechanical properties. This section includes a brief description of tissue biomechanics of prostate, theory of elastography, and different elastography techniques that have already been researched in prostate disease. The reported evidence of performance will also be summarised and compared in this section. This section lays a foundation of using elasticity as a biomarker for this research project.

3. An alternative elastography is optical coherence elastography equipped with a much higher resolution than current clinical elastography techniques. It is a novel, safe, and non-invasive optical imaging elastography, aiming at early detection of subtle changes in diseased tissues. The theory and development of this technique will be provided in this section. Further description of the system setup used in this research project will be given in detail in Chapter 3.

2.1 Prostate Cancer

The prostate is an exocrine gland situated at the origin of the urethra, beneath a man's bladder, and toward the front of the rectum. The prostate secretes fluid that nourishes and protects sperm. The fluid makes up around 20 to 30 percent of semen. During ejaculation, the muscles of prostate help to expel the semen. It is approximately the size of a large walnut and weighs between 20 and 30 grams, while an enlarged prostate can weigh up to 100 grams. The prostate gland is composed of three zones: central, peripheral and

transitional zones. The peripheral zone of the prostate gland is where majority of PCa originate. PCa can develop when cells in the prostate start to grow in an uncontrolled way. The most common kind of PCa (approximately 95%) is adenocarcinoma which starts in some of the cells that line the prostate – called glandular epithelial cells. The aggressiveness of PCa is characterized by Gleason score based upon the cell pattern under the microscope in the current clinical care. It is given by n + m, where n is the dominant pattern of the tumour, and m is the next-most frequent pattern. Generally, a higher Gleason score means more advance the cancer, and a worse prognosis.

2.1.1 Histology and pathology of prostate cancer

Microenvironment

The normal prostate gland is composed of epithelial and stromal cells [13]. Pathogenesis of PCa is not yet well understood. It usually begins with the transformation of normal cells to carcinoma cells, and continues with tumour growth, invasion and metastasis. Tumour stroma is different from the stroma in normal tissue. Considerable evidence [14-16] has shown that a new reactive stroma forms to enhance tumorigenesis during PCa progression. As illustrated in Figure 2.1, secretory luminal and basal cells in the normal human prostate gland are confined by basement membrane, and surrounded stroma is consisted of extracellular matrix (ECM), fibroblasts, smooth muscle cells (SMC), immune cells, nerves and blood vessels. PCa cells proliferate and invade through basement membrane into the host stroma followed by ECM remodelling and basement membrane degradation. The disruption creates a new stromal microenvironment termed ‘reactive stroma’ to support cancer cell survival, proliferation and migration, and induces angiogenesis. In the new formed stroma, stromal cell is substituted by myofibroblasts, the order of ECM is disturbed with increased angiogenesis, collagen deposition, and influx of tumour associated macrophages (TAM).

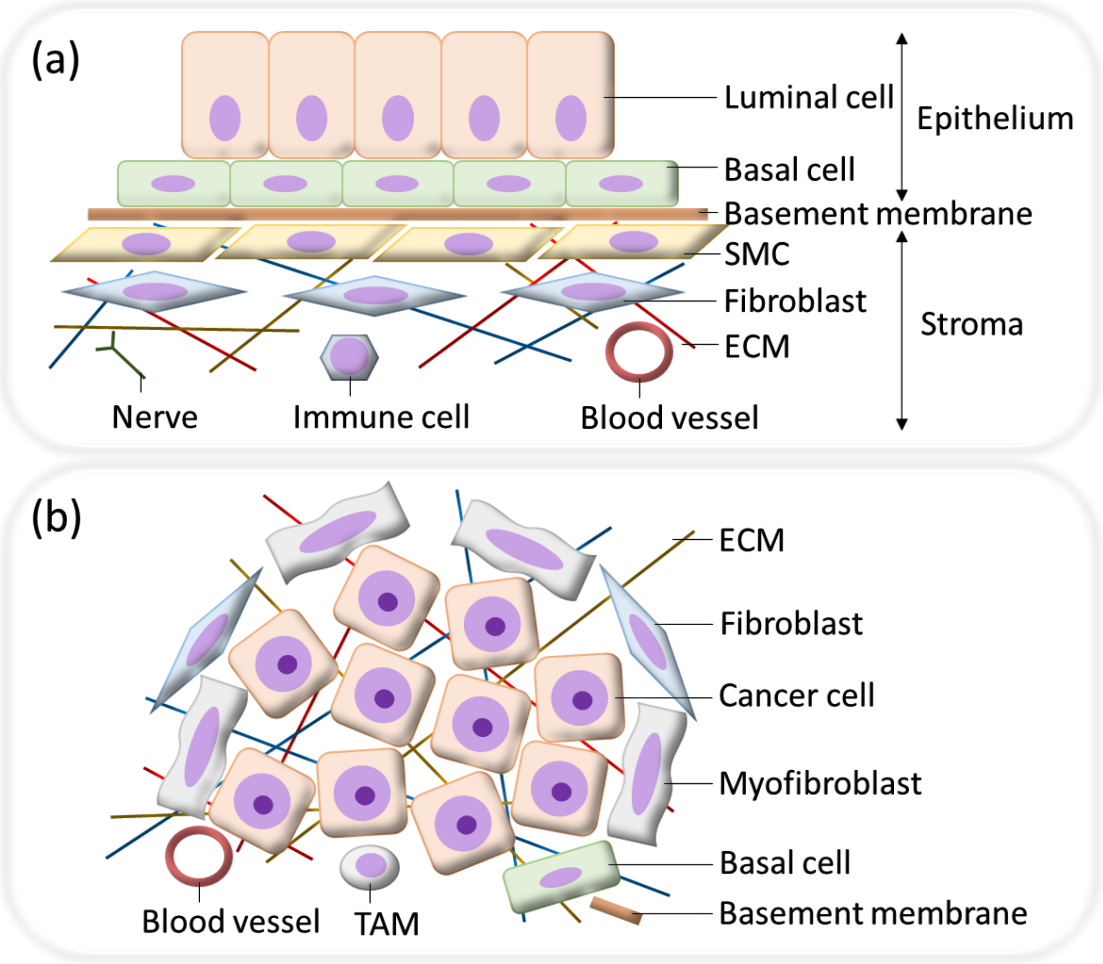

Figure 2.1 Sketch of the microenvironment of (a) normal prostate gland, and (b) prostate cancer (PCa). Smooth muscle cells (SMC), extracellular matrix (ECM), tumour associated macrophages (TAM).

Classification systems

Gleason system has been the single most powerful prognostic factor for PCa since the introduction of this system by Gleason et al. based on a study of 270 patients [17] upon the architectural pattern of the glands of the prostate tumour under the microscope. Each pattern has a corresponding Gleason grade of 1 to 5 where Gleason 1 is the most well-differentiated tumour pattern while Gleason 5 is the least. A higher Gleason score/grade means a more aggressive tumour and a worse prognosis. By 1974, Gleason and his team expanded to 1032 men in a following study [18]. The histologic and clinical diagnosis of PCa as well as its treatment has evolved since the original system, therefore urological pathologists have been adapting Gleason system to accommodate the changing practice of contemporary medicine. An International Society of Urological Pathology (ISUP) consensus has been held in 2005 [19] and 2014 [20] to address the controversial areas and improve the overall Gleason system. The difference of the original and modified Gleason

systems is compared in Figure 2.2. As most of the tumours typically have two histological patterns, a Gleason score is reported as a mathematical equation (n+m) where n is the predominant pattern of the tumour (greater than 50% of the total pattern), and m is the next-most prevalent.

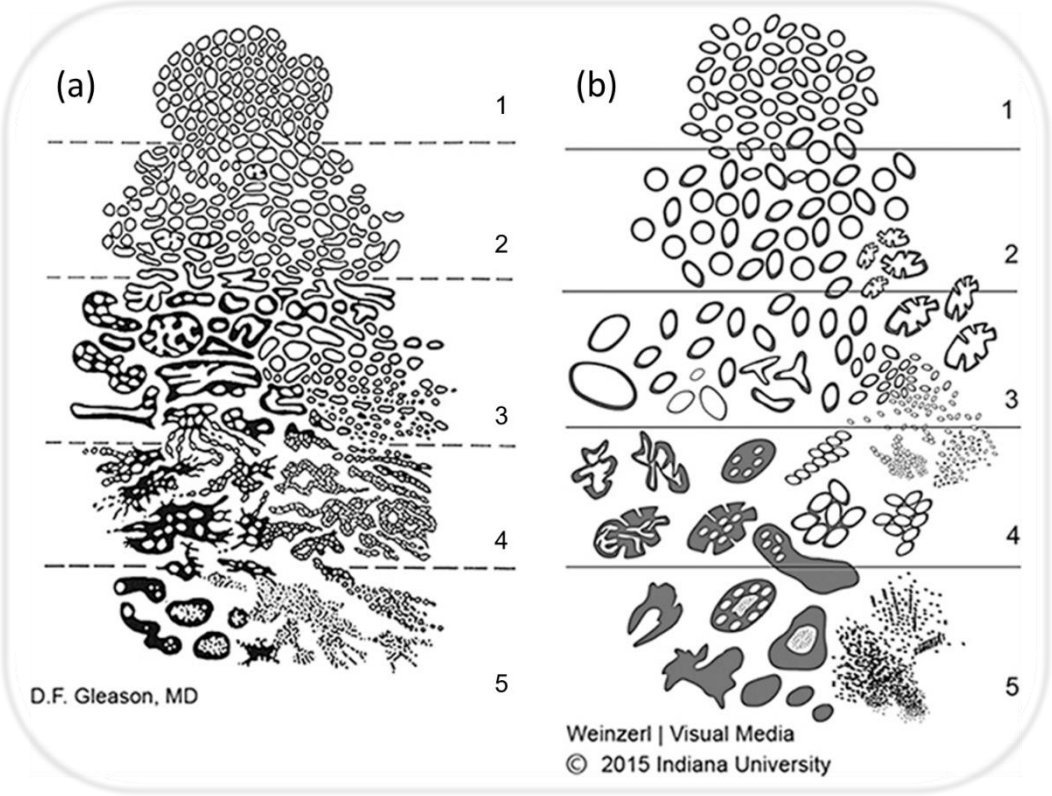

Figure 2.2 Comparison of original (a) and 2015 modified ISUP (b) Gleason schematic diagrams of histologic patterns of prostate adenocarcinoma. Adapted from Epstein et al. 2016 [20].

Alternatively, the term Gleason score can be assigned in the form of the final sum of n and m. If the latter is presented, the number can range from 2 to 10. In today's practice, the lowest score assigned on prostate biopsy is Gleason 3+3=6 [20], which is in the middle of the range. This could make some patients assume that a diagnosis of Gleason score 6 on biopsy is serious and expect that treatment is necessary, thus overtreatment can happen. In the current application of the Gleason system, Gleason 3+4 and 4+3 are often considered the same prognostic group (Gleason score 7), whereas the latter is more poorly differentiated cancer. A contemporary grading system with *Grade Groups 1-5* [20] for PCa was recently proposed by Epstein et al. in 2013 based on data from John Hopkins Hospital with a more accurate grade stratification than the current Gleason system. They validated the accuracy of the new system with the outcomes in a multi-institutional study with 20845 radical prostatectomy (RP) cases [21]. It is recommended by ISUP and the

World Health Organization (WHO) to report the Grade group in conjunction with the overall or global Gleason score of a prostate biopsy or RP to increase the prognostic accuracy and simplify the procedure. The details of stratification and corresponding histological description of each grade group is listed in the table below.

Table 2.1 Histological definition of new five-tier grading system. Adapted from [20].

Grade group	Gleason score	Histological definition
1	6 (3+3)	-Only individual discrete well-formed glands
2	7 (3+4)	-Predominantly well-formed glands with lesser component of poorly formed, fused, cribriform glands
3	7 (4+3)	-Predominantly poorly formed, fused, cribriform glands with lesser component of well-formed glands
4	8 (4+4 or 3+5 or 5+3)	-Only poorly formed, fused, cribriform glands or -Predominantly well-formed glands and lesser component lacking glands -Predominantly lacking glands and lesser component of well-formed glands
5	9-10 (4+5 or 5+4 or 5+5)	-Lack of gland formation (or with necrosis) with or without poorly formed, fused, cribriform glands

2.1.2 Diagnosis of prostate cancer

According to Prostate Cancer UK (PCUK), PCa is the most common cancer in males in UK. Every day, about 130 men are diagnosed with PCa across UK and two men die from PCa in Scotland. PCa often grows slowly and there may be no warning signs in the early PCa. If symptoms emerge, many are like those caused by an enlarged prostate, such as trouble urinating, blood in the urine or semen, and pain in the lower back, hips or thighs. PCa is commonly diagnosed in the men aged 50 and over, especially between 65 and 69. It is of great significance of screening and diagnosis of early PCa to identify curable lesion in time before spreading outside the prostate. Although there are screening programmes for breast, cervical and bowel cancer in the UK, no test is reliable enough to be used as part of a screening programme for PCa. The European Association of Urology (EAU) [22] is still against systematic population-based screening in the latest 2016 guidelines on

PCa in Europe. The benefits and drawbacks of a potential screening program for PCa need to be revaluated.

Current protocol for diagnosis

Figure 2.3 is a flowchart of the routine clinical care for PCa. If men have a raised serum prostate-specific antigen (PSA) level, the patients are referred to clinics to have a digital rectal examination (DRE). Abnormal DRE results can indicate that the patients might be suspected with PCa. Then physicians perform a trans-rectal ultrasound (TRUS), which is followed by pathological examination using Gleason scoring system and Grade groups. The patients with a positive TRUS biopsy are further scheduled magnetic resonance imaging (MRI) or computerised tomography (CT) scans to confirm the size of the tumour and whether it has been spread to other parts of the body. In this section, the main diagnostic methods will be introduced, as well as the pros and cons of each method.

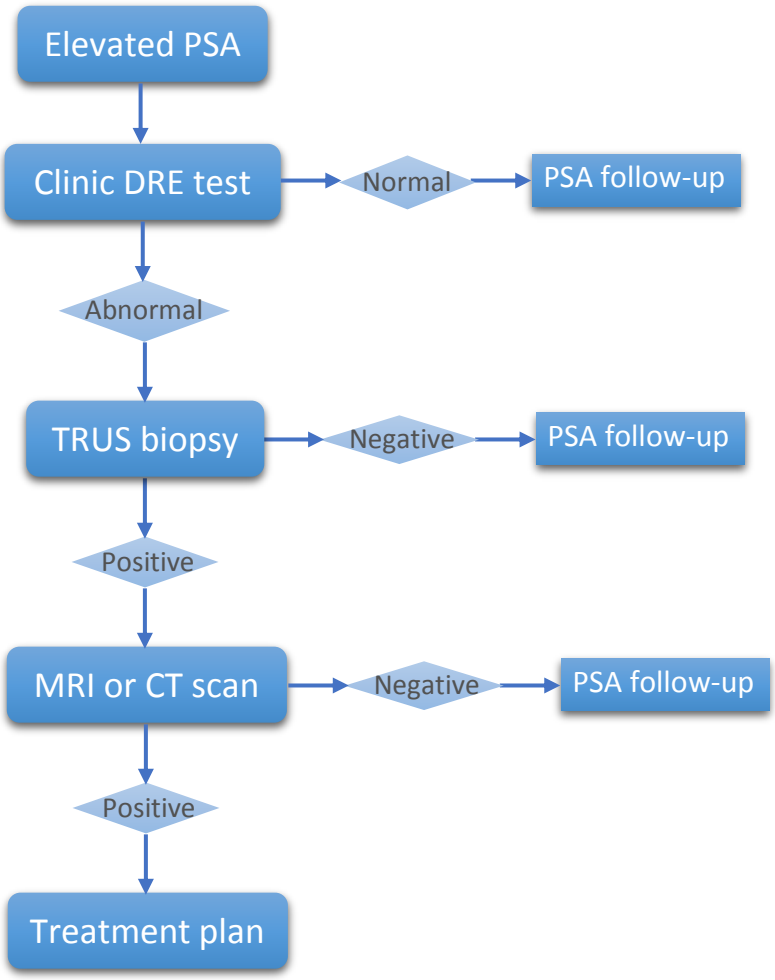

Figure 2.3 Current diagnostic protocol for PCa.

Prostate specific antigen

Serum prostate specific antigen (PSA) testing, a blood test to measure the amount of PSA in the serum, was introduced in the late 1980s. It is often recommended for men over 50 or of a higher risk of genetics and ethnicity. A man with a family history of PCa or breast cancer are more likely to get PCa, and the risk of PCa might be higher for the black men than other men. PSA is a glycoprotein produced by the secretory epithelial cells of both benign and malignant prostate gland so it is normal for all men to have a small amount of PSA in their blood. An elevated PSA level may be a sign of PCa, but it also can be caused by advancing age or other conditions such as prostatic hyperplasia, prostatitis, or prostate trauma. Studies [23, 24] have shown controversial results of PCa screening with the PSA test and have generated conflicting recommendations. Moreover, there are significant PCa with PSA levels lower than the normal threshold.

There are two well-designed large randomized trials regarding PSA screening: the Prostate, Lung, Colorectal and Ovarian (PLCO) screening trial [25, 26] in the United States and the European Randomized Study of Screening for Prostate Cancer (ERSPC) [27, 28] initiated in Netherlands and Belgium. Both trials launched the PSA screening in 1993, but ERSPC had six other countries (Sweden, Finland, Italy, Spain, Switzerland, and France) that participated into the study between 1994 and 2003. It was reported in the PLCO's results that the PSA screening cannot reduce mortality, and organized screening has no benefits outweighing opportunistic screening. Although ERSPC showed the PSA test could reduce the death risks by 20% in a report at 9 years' follow-up [27], but this needs to be balanced against the harms like overdiagnosis and overtreatment.

A disparity exists between these two studies because there were some differences between the two trials. First of all, the ERSPC study is more sensitive to find PCa due to a lower cut-off level (3.0 ng/mL), while the PLCO study used 4.0 ng/mL. Moreover, different screening protocols and threshold values of PSA were used in the different countries of the ERSPC study, and the heterogeneity of data is the main limitation. Also, 46% of the control group in the PLCO study had at least one PSA test prior to trial entry, and 78% in the screened group [29]. These data suggest that there would be less difference between two groups in the PLCO study. Notwithstanding, a lower level of contamination was noticed in ERSPC than in PLCO [29].

In summary, many organisations in different countries recommend against a national screening programme for PCa based on several reasons.

Firstly, the PSA test is not accurate enough to justify a national screening programme. A low threshold value will lead to increased morbidity, but the absolute reduction in mortality of PCa is not significant.

Secondly, the main downside of PSA screening is overdiagnosis that means cancers are identified in men but will never cause any symptoms or shorten life [30]. Due to the disease nature of PCa, the PSA test is unable to differentiate between indolent and aggressive PCa. Diagnosing aggressive cancers is lifesaving, but diagnosing indolent PCa can lead to problematic overtreatment that is worse than the disease itself. PCa is so slow-growing that many men might die with PCa instead of from PCa.

Thirdly, a false-positive result can cause great anxiety to the patients and often triggers an unnecessary prostate biopsy. In fact, there is about 75% of men with a raised PSA level do not have PCa [27]. A population-wide screening programme using the PSA test also means many men would have biopsies unnecessarily and complications [31, 32] including infection, erectile dysfunction, urinary, and bowel problems.

Last but not least, although ERSPC has showed a decrease in the number with increased years of follow-up study [27, 28], 781 men would need to be screened and 27 additional men would receive unnecessary treatment to save one man from PCa in a report at 13 years' follow-up [28].

Therefore, more research is needed to determine the trade-offs of a screening programme. Given the evidence against a national screening programme, the National Health Service (NHS) provides a Prostate Cancer Risk Management Programme (PCRMP) which allows patients to make the decision whether to go for a PSA test after informing the possible benefits and harms of the PSA test. Furthermore, the results published from Prostate Testing for Cancer and Treatment (ProtecT) trial [33-35] provide further perspective about survival and quality of life for patients diagnosed by PSA screening.

Trans-rectal ultrasound guided biopsy

A further test to diagnose PCa is trans-rectal ultrasound (TRUS) guided biopsy as illustrated in Figure 2.4 (a). This procedure is followed by evaluation of the tumour volume and aggressiveness under the microscope by the pathologists. TRUS imaging is based on increased brightness with respect to the strength of the echo. Prostate biopsy is currently the most reliable way to confirm PCa. Because the conventional grey-scale TRUS is insensitive to identify the small lesion, it normally requires about 12 small

samples of tissue from different part of the prostate as demonstrated in Figure 2.4 (b). Since the establishment of TRUS sextant biopsy method in 1989 [36], there has been a strong research focus on accurately characterising patients for effective management. Increasing cores of biopsy could result in a higher detection rate without considering risks and complications.

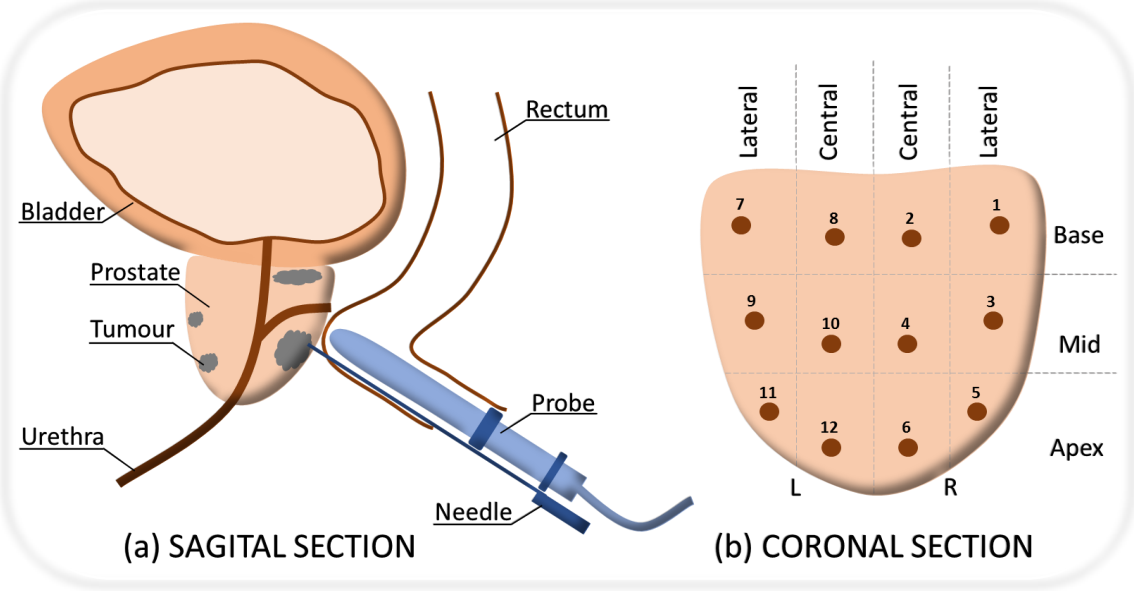

Figure 2.4 Schematic diagrams of (a) the trans-rectal ultrasound biopsy (TRUS) for the man suspected with prostate cancer (PCa) and (b) the standard 12 core biopsy.

Eichler et al. [37] compared across different biopsy schemes and concluded that the protocol with 12 cores that compromised the adverse events could detect 31% more cancers than the sextant cores. Nevertheless, there has been a large disparity existing between Gleason score on the initial biopsies and after the final RP. Cohen et al. [3] conducted a meta-analysis of 14839 patients worldwide, who were diagnosed of PCa with TRUS biopsy and then underwent RP. It was found that only 58% of the patients in whom the RP grade was accurately predicted. Serefoglu et al. [4] evaluated the false-negative risk from 90 patients and found that only 43.3% of patients had the same Gleason score of preoperative biopsy and postoperative specimen with the false-negative rate of more than 30%. A healthcare challenge remains that the improvement of the accuracy of detecting in the initial prostate biopsy would enable more appropriate therapy choices to be made and especially avoid unnecessary RP.

The other healthcare challenge is the complications of the prostate biopsy, though biopsy-related mortality is rare [32]. It is common to have typically minor complications after

the TRUS procedure such as pain and bleeding which are usually self-limiting and do not require intervention [32]. In a prospective cohort study [31] (Prostate Biopsy Effects: ProBE nested within ProtecT study in UK), one in five men at seven days after a first biopsy had reported a negative attitude to repeat biopsy due to unfavourable experience. At 35 days after biopsy, 43.6% of 984 men had pain, 65.8% of 976 men had haematuria, and 94.0% of 937 men had any infective/haemorrhagic symptoms. Moreover, the hospitalization rates for complications after the procedure have increased dramatically and the most common reason is infectious complications. It was reported [38] in a population based study of 75190 men who received TRUS biopsy in Ontario, Canada that 55.4% of men were misdiagnosed with PCa. The rate of hospitalization within 30 days of the procedure increased from 1.0% in 1996 to 4.1% in 2005 ($p < 0.0001$).

Scans and staging

Sometimes imaging modalities such as magnetic resonance imaging (MRI), computerised tomography (CT) scans or X-rays are utilized to confirm the size of the tumour and detect whether the cancer has spread outside the prostate. This helps accurately stage cancer and make an optimal decision for treatment.

The scan results are usually recorded using the tumour node metastasis (TNM) system, where the T stage represents the extent of the cancer has spread in and around the prostate (usually by DRE or MRI scan), the N stage represents whether the cancer has invaded to the regional lymph nodes (usually by MRI or CT scan), and the M stage represents whether the cancer has metastasised to other distant parts of the body (usually by bone scan). Moreover, the TNM stage is used to define if the cancer is localised (the cancer contains inside the prostate and possibly be T=T1 or T2, N=N0 or NX, M=M0 or MX), locally advanced (the cancer starts to break out of the prostate and possibly be T=T1 or T2, N=N1, M=M0 or T=T3 or T4, N=N0 or N1, M=M0), or advanced (the cancer spreads from the prostate to other parts of the body and possibly be any T or N stage, M=M1).

Another classification for localised PCa is the EAU risk groups [22] by combining the serum PSA, Gleason grade and clinical stage for biochemical recurrence after local treatment. Three risk groups are defined: low-risk (PSA<10 ng/mL and Gleason score<7 and clinical stage T1-2a), medium or intermediate-risk (PSA=10-20 ng/mL or Gleason score=7 or clinical stage T2b), and high-risk (PSA>20ng/mL or Gleason score>7 or clinical stage T2c or any PSA or Gleason score, clinical stage T3-4 or N1).

Digital rectal examination

Digital rectal examination (DRE) is a traditional modality to tell the difference by feeling the prostate through the wall of the rectum. It is one example of the standard medical practise, palpation, based on qualitative assessment of the size, shape and stiffness. As illustrated in Figure 2.5, the doctor wears a pair of glove, inserts one finger into the rectum with lubrication, and perceives the prostate to check for anything abnormal. PCa is much stiffer than normal prostate [6], and benign prostatic hyperplasia (BPH) is much larger. The underlying reason for DRE is that stiffness difference of tissue is correlated with pathological changes.

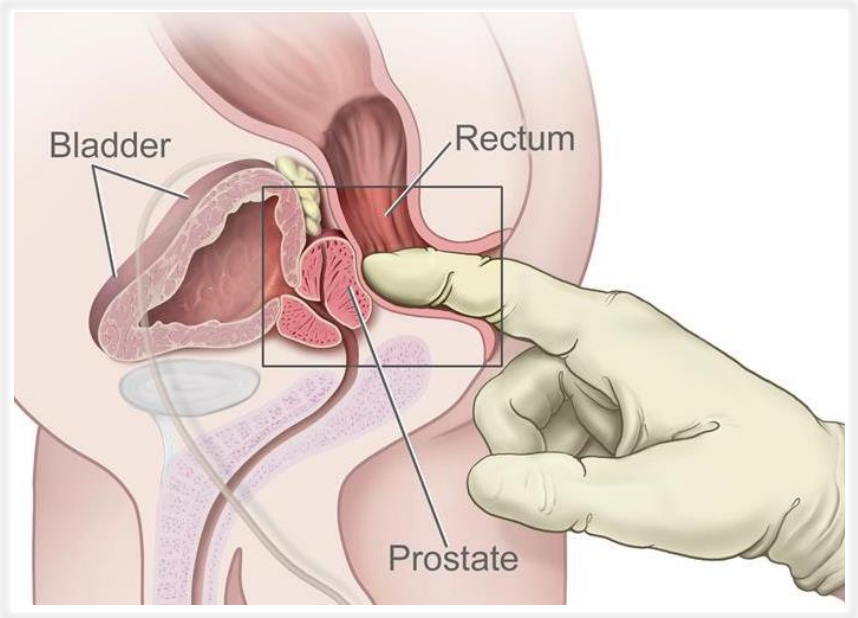

Figure 2.5 Illustration of digital rectal examination. Adapted from Wikipedia 2017 [39].

However, palpation is only suitable for superficial evaluation, but not capable to find a pathological lesion which is small in size or deep in body location. Though DRE can detect the prostate abnormity by feeling the prostate, it is highly dependent on the operator's experience and limited to the posterior part of the prostate. It was reported that only 20% cancers can be detected by DRE [40]. Also, same limitation as the PSA test, the DRE test is difficult to quantify the aggressiveness of the cancer and misdiagnosis can happen. Since the introduction of the PSA test into clinical practice in the late 1980s, the DRE test is commonly employed with the conjunction with the PSA test [41].

2.1.3 Summary of diagnostic methods

In summary, the differing elasticity of soft tissue has been an established practice for centuries to differentiate healthy from diseased tissue, especially in breast and prostate tissue. PCa was traditionally diagnosed with DRE of the prostate by feeling the stiffness alteration in the prostate. Conventional ultrasound is a popular clinical imaging technique for lesion anatomy based on the acoustic properties of soft tissues, but many soft tissues can share similar ultrasonic echogenicity. In prostate ultrasound imaging, TRUS is already in use clinically around the world to guide prostate biopsies. However, tumours of prostate may be invisible or barely invisible in standard ultrasound examinations, which leads to unreliable assessment of the tumour volume [2] and cancer staging [3, 4]. Other scanning methods such as MRI and CT are suitable for tumours larger than 3 mm, not sensitive to subtle changes of small tumour.

2.2 Prostate Elastography

The direct mechanical evaluation of prostate elasticity was investigated by Krouskop et al. [6] with displacement loading experiments. It was found that tissue from PCa has a measurable elevated Young's modulus compared with the normal prostate glandular tissue, and tissue from prostate with BPH is significantly softer than normal tissue. This was followed by a lot of work in the advancement of direct mechanical assessment of prostate samples using different indenters [42-44], but it has been the engineering changes to apply indenters *in vivo*. Therefore, there has been much more attention in sonoelastography (ultrasound elastography) techniques for visualizing anatomy as well as mechanical properties of soft tissues which can take advantage of the use of *in vivo* TRUS imaging and moreover overcome the shortcoming of conventional ultrasound.

The reported elasticity values of prostate vary over two orders of magnitude in the abovementioned literature. This is probably because of the variance in location of the tissue (e.g. central, peripheral, transitional zone) the tissue condition (e.g. healthy or malignant, *in vivo* or *ex vivo*, fresh or fixed in formalin), experimental conditions (e.g. precompression loading and ambient temperature for *ex vivo* study), frequency of mechanical excitation, and measurement method (e.g. mechanical assessment method, ultrasound, MRI).

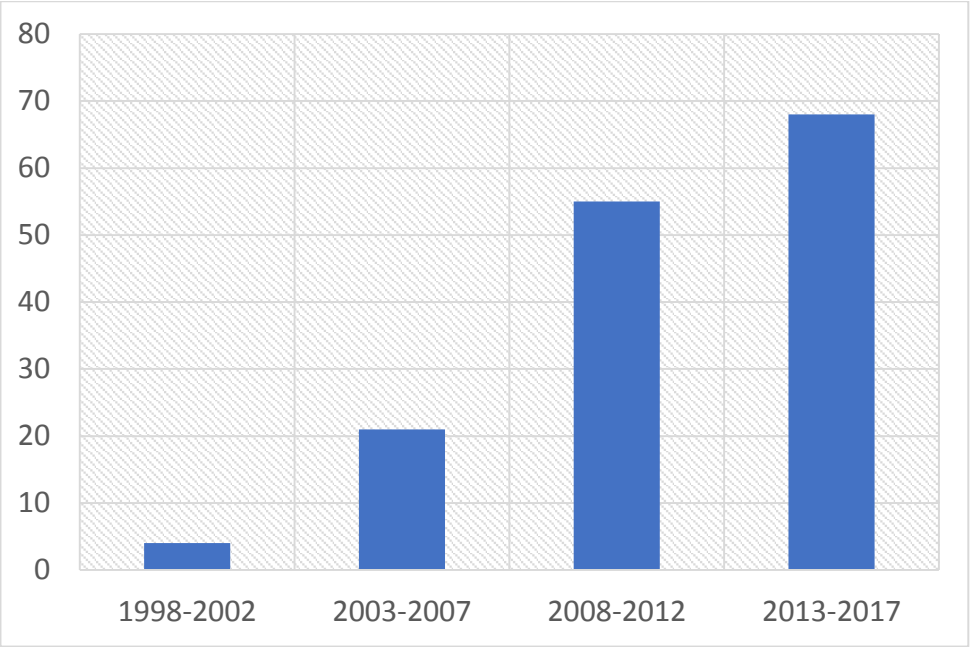

Figure 2.6 Number of elastography papers published on the area of prostate in the last 20 years.

A systematic review was performed by searching Web of Science database for English language publications in June 2017 using the key work 'elastography' and 'prostate'. There are 142 papers published excluding the ones with reply only. As the chart demonstrated in Figure 2.6, a substantial increase of interest has begun since 2008 to implement elastography using various excitation and measurement techniques to guide prostate biopsy *in vivo* and increase the diagnostic accuracy of PCa. The following contents will provide a brief review of tissue biomechanics, physics of elastography and main classifications regarding the application in prostate from research and clinical perspective.

2.2.1 Tissue biomechanics

Prostate is among the primary group of tissue called soft connective tissue. In contrary to hard tissue such as bone, the cells in soft tissue are separated by extracellular matrix (ECM). Soft tissue has high flexibility and soft mechanical properties owing to complex fibre-reinforced composite structures which tend to have preferred directions. Therefore, the mechanical behaviour of biological soft tissues is determined by the concentration and structural arrangement of constituents such as collagen and elastic fibres, the hydrated matrix of proteoglycans, etc. [45]. Among them, collagen is a protein predominant in the ECM and the main load carrying element [46, 47].

The tensile response of soft tissues is nonlinear stiffening as illustrated in Figure 2.7. It is a typical stress-strain curve for biological tissue, and soft tissues are presented to undergo large deformations before failure. At the very beginning of deformation, elastic fibres are mainly responsible for the stretching mechanism, and then collagen fibres involve in to bear loads by gradually lining up with the load direction. The tissue becomes stiff at higher stress with straightened collagen fibres until the ultimate tensile strength is reached and fibres begin to break.

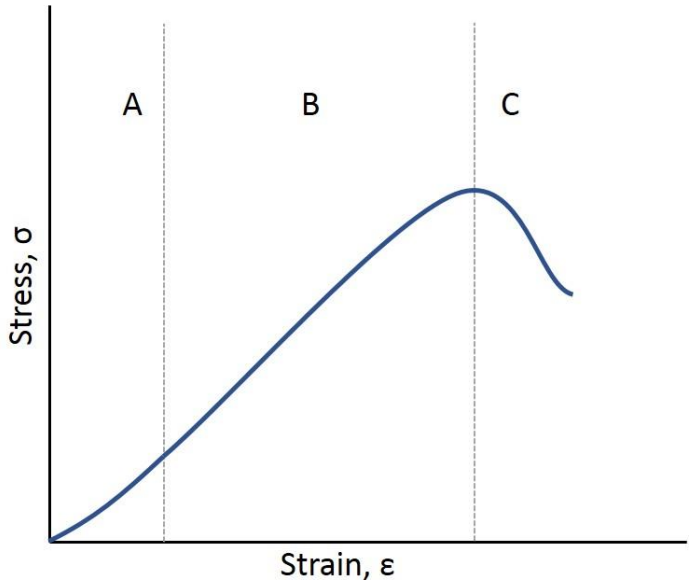

Figure 2.7 Schematic diagram of a typical stress-strain curve for biological tissue with three distinct regions: toe region (A), linear region (B), and failure region (C).

The tendency of a material to resist deformation when loaded is commonly termed as ‘stiffness’, ‘hardness’ or ‘elasticity’, which is the parameter elastography evaluates. Elastic behaviour is defined if a material deforms when loaded and returns to its original shape after the applied force is removed. In reality, many soft tissues exhibit both elastic and viscous behaviour, which is viscoelastic. Some recent studies [44, 48] have used viscoelastic models (Kelvin-Voigt and Kelvin-Voigt functional derivative) to characterize prostate mechanical response, but these are small studies with preliminary results.

Moreover, soft tissues are heterogeneous materials due to their complex composition in microscopic perspective. A complex mechanical system is required to fully characterize general soft tissues using a great number of parameters such as Young’s modulus, shear modulus, bulk modulus, nonlinearity, Poisson’s ratio, viscosity, anisotropy and heterogeneity indices, etc. However, in most practical cases, even one elasticity parameter

is adequate to address the pathological difference in most soft tissues, such as Young's modulus. This is the basis for manual palpation of cancer lesion in breast and prostate practice, where the variations of the Young's modulus of tissue are measured by perceiving the structural changes. Soft benign tissues have larger deformation whereas stiff cancer lesions have smaller deformation.

To yield quantitative information of tissue mechanics, proper assumptions are needed to simplify the comprehensive mechanical model of soft tissues. Using compression method, most commonly, the stress is assumed to be uniformly distributed throughout the sample. Also, tissue is approximated as a linear elastic solid with homogenous properties.

(1) 'Linear' means the strain of tissue is not of functional relationship to the stress for the level of strain typically less than 10% [6].

(2) Pure 'elastic' tissue (spring like) can be characterized with elastic modulus such as Young's modulus.

(3) Soft tissues of 'homogenous' properties assumes the tissue will stay the same with the orientation.

Given the assumption that the elastic modulus is independent of these variables, it shows a high correlation with the clinical data [1, 49] where elasticity could be a reliable biomarker for PCa using ultrasound elastography.

2.2.2 Principles

Elastography enables deeper tissue elasticity imaging by portraying information about the tissue stiffness or elasticity that is the resistance to the deformation. It was originally realised by ultrasound based technique called strain elastography. Given the assumption of soft tissue as a linear elastic solid with isotropic mechanical properties, the stress, σ, is the ratio of the applied loading force, F, to the cross-sectional area, A, over which the force is applied.

$$\sigma = \frac{F}{A} \qquad (1)$$

The resulting deformation is quantified by strain, ε, which is an engineering term to measure relative deformation. It is the ratio of the magnitude of the deformation, ΔL, divided by the original length, L, of the material or tissue as given in Eq. (1). The images of tissue strain are named elastograms.

$$\varepsilon = \frac{\Delta L}{L} \quad (2)$$

The difficulty to deform soft tissues via compression and shear is expressed by the Young's modulus, E, and the shear modulus, G. Herein E is the ratio of the stress over the strain in tensile/compression and G is that in shear. These moduli are typically calculated using two methods [7] as shown in Eq. (3) and (4) which are the principles for strain elastography (SE) and shear wave elastography (SWE), respectively. In strain imaging, displacement in the same direction as pulse propagation of compressive wave (longitudinal wave) is measured to calculate strain, while in shear wave speed imaging, the displacement of tissue in the orthogonal direction to the shear wave (transverse wave) propagation is measured to calculate their speed.

1) Quasi-static method which can calculate E using Hooke's law after externally applying stress, σ, and measuring strain, ε.

$$E = \frac{\sigma}{\varepsilon} \quad (3)$$

2) Dynamic method which can calculate E and G after propagating shear waves and measuring the propagation speed, c_s.

$$E = 2(1 + v)G = 3G = 3\rho {c_s}^2 \quad (4)$$

where the tissue density, ρ, differs for various tissue, and Poisson's ratio, v, is near 0.5 (between 0.490 and 0.499 [50] for an incompressible soft tissue due to the high water content of soft tissues.

To perform elastography imaging, two common elements are required: excitation and detection. Excitation of mechanical load or stress is achieved either by an internal physiological motion source or an external excitation source. The internal source includes cardiovascular pulsation and respiratory motion. The external source includes shear wave, surface acoustic wave (SAW) and acoustic radiation force (ARF). For detection of the tissue response, the deformation or displacement in tissue is measure, and then the tissue stiffness or elasticity can be calculated. The measurement can be performed using either magnetic resonance imaging (MRI), ultrasound imaging, X-ray or optical imaging. The classification of different elastography techniques can be based on both excitation and detection methods.

2.2.3 Ultrasound elastography

Ultrasonography has been widely used as a medical imaging technique for diagnosis in current clinical practice with many clinical applications, such as real-time visualization of internal organs and foetus. Ultrasound elastography provides images of tissue stiffness with the use of ultrasound. Quasi-static elastography or strain elastography (SE) was a pioneer elastography technique developed by Ophir Group in 1991 [8]. In quasi-static elastography, an external compression is applied to the tissue, and the morphology of the prostate tissue changes after the application of the compression wave. Softer tissue has more deformation (strain) than stiffer tissue does for a given applied force or stress. The conventional B-mode ultrasound images are compared pre- and post- the compression, which yields to a colour map of local tissue strain termed elastogram.

Since 2005, increasing availability of ultrasound elastography systems especially SE techniques has enabled large numbers of new applications in all sorts of tissues in clinical practice. Among them, the most common clinical applications are breast, liver, prostate, thyroid, lymph nodes, arterial wall and thrombosis [10]. Ultrasound elastography is generally categorized by the differences in the measured physical quantity, the excitation method, and the method of displaying the tissue response. In clinical practice, the most dominant ultrasound elastography techniques are classified as quasi-static elastography or strain elastography (SE), shear wave elastography (SWE) and transient elastography (TE) [51]. Among them, SE and SWE are most commonly used in prostate elastography [52].

Prostate strain elastography

In the scenario of prostate quasi-static elastography, a mechanical compression requires the operator to apply alternative pushes with the transrectal ultrasound transducer [1] or a saline-filled sheath around the transducer in endocavity applications [53]. The compression wave can be generated by manual compressions and decompressions of the prostate tissue. Instead, a more consistent and stable compression can be achieved by a water-filled balloon [54] placed between the probe and the rectal wall. This modified new elastography method can therefore improve the reproducibility of prostate imaging.

The elastogram is superimposed on the B-mode images as a colour map, and it typically utilizes blue colour to indicate region of low strain or stiff tissue, and red colour to be region of high strain or soft tissue as demonstrated on Figure 2.8. A stiff nodule larger than 5 mm diameter was noticed in Figure 2.8 marked with arrow [55] using SE, while it

was not noticeable in the standard grey-scale ultrasound image. Since SE is a qualitative technique, tissue stiffness is estimated by visualizing the difference in strain between adjacent areas without quantitative elastic analysis [56].

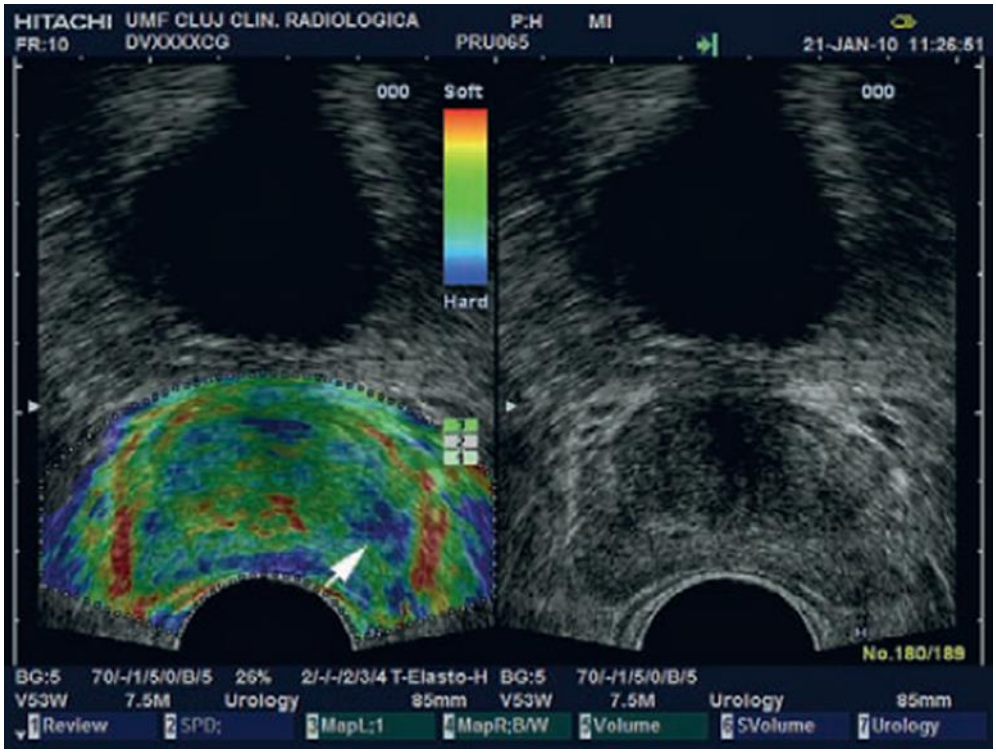

Figure 2.8 Strain elastography (SE) (left) and ultrasound (right) images of a prostate with a stiff and malignant nodule pointed by arrow. Adapted from Guirgiu et al. 2011 [55].

The first clinical study on the detection of PCa by real-time SE was performed by Cochlin et al. [49] in 2002. They applied real-time SE on any abnormal areas detected by grey-scale ultrasound and evaluated SE results with biopsy data in 100 patients. The sensitivity and specificity of elastography imaging for the detection of PCa were 51% and of 83%, respectively. Pallwein et al. [57] increased the number of recruited patients to 492 and compared the SE findings with systematic biopsy results. They reported a robust sensitivity of 87% and a specificity of 72%. However, several groups were not able to reproduce such promising results. More studies with inconsistent values reported for sensitivity and specificity are summarised in Table 2.2. Instead using histopathological needle biopsy data as a reference standard, a few studies [54, 58-61] have focused on assessing the efficacy of SE by comparing the findings to histopathological analysis of the whole mount sections after RP. Among them, Brock et al. [61] carried out a study in 229 patients with biopsy-proven PCa using grey-scale ultrasonography and real-time SE with a sensitivity and specificity of 18% and 50%, respectively.

Additionally, several groups have performed a meta-analysis to assess the accuracy of SE imaging in detection of PCa. Teng et al. [62] included six studies with 527 patients using biopsy as the reference standard. They reported that transrectal sonography had a pooled sensitivity of 62% and specificity of 79%. Zhang et al. [63] conducted another meta-analysis of data from seven studies with 508 patients using RP results as the reference standard. It was reported that real-time SE has a pooled sensitivity of 72% and specificity of 76%. Most SE imaging has shown promising results for PCa diagnosis over conventional grey-scale sonoultrasound. However, the technique has limited applications due to the inter- and intra-observer disparity.

Table 2.2 Summary of strain elastography studies assessing malignancy of masses in the prostate.

Year	Reference	Patients	Gold standard	Reference standard	Location	Sensitivity (%)	Specificity (%)	PPV (%)	NPV (%)	Accuracy (%)
2002	Cochlin et al. [49]	100	Biopsy	Colour pattern		**51**	**83**	72		
2008	Pallwein et al. [57]	492	Biopsy	Colour pattern		**86.9**	**71.9**	61.6	91.4	77
2008	Kamoi et al. [64]	107	Biopsy	Colour pattern		**68**	**81**	68	81	76
2008	Salomon et al. [59]	109	RP specimen	Colour pattern		**75.4**	**76.6**	87.8	59	76
2009	Ferrari et al.	84	Biopsy	Colour pattern		**51**	**75**	64	64	64
2010	Aigner et al. [65]	94	Biopsy	Colour pattern		**74**	**60**	39	93	
2010	Tsutsumi et al. [54]	55	RP specimen	Colour pattern	Anterior	**84**	**80**	75	87	
					Middle	**85**	**91**	79	94	
					Posterior	**60**	**96**	93	71	
2011	Brock et al. [66]	229	RP specimen	Colour pattern		**50.4**	**71.5**	75.8	43.6	59.1
2011	Giurgiu et al. [55]	65	Biopsy	Colour pattern		**67.9**	**62.2**	57.6	71.9	
2011	Zhang et al. [67]	83	Biopsy	Strain index		**74.5**	**83.3**			90
2012	Brock et al. [61]	178	Biopsy	Colour pattern		**60.8**	**68.4**	32.4	87.8	
2013	Brock et al. [68]	86	RP specimen	Colour pattern		**49**	**73.6**	77.8	50.7	61.8
2014	Zhu et al. [69]	56	RP specimen	Colour pattern		**67.6**	**89.5**			82.7

Positive predictive value (PPV), negative predictive value (NPV), radical prostatectomy (RP)

Prostate shear wave elastography

Shear wave elastography (SWE) is a more recent technique which can remove the bias with a quantitative elasticity assessment of the mechanical properties of soft tissues in real time [1]. It monitors the propagation of shear waves and estimates shear wave velocity through tissue [7]. Shear wave velocity is affected by the tissue stiffness and propagates faster in stiffer tissue than in softer tissue. There is no requirement for compression on the rectal wall to produce elastograms. Alternatively, an endorectal transducer is employed to generate shear wave remotely in the prostate. The external excitation sources can use the acoustic radiation force of a focused ultrasonic beam [1].

Then tissue stiffness can be derived by measuring the speed of the shear wave propagation [51]. Similar to SE, the colour-map elastogram of the shear wave velocity or the Young's modulus is displayed as overlay on the B-mode images. Figure 2.9 demonstrated two regions of interest (ROI) in both SWE and ultrasound images. One ROI was in the lateral peripheral zone with mean elasticity of 18.4 kPa, and the other ROI in the same sextant was located in the left base paramedian with mean elasticity of 54 kPa, whilst no difference was noticed between the two ROIs in the ultrasound B-mode images. The biopsy performed in the stiffest area revealed an 11 mm Gleason 7 adenocarcinoma [70].

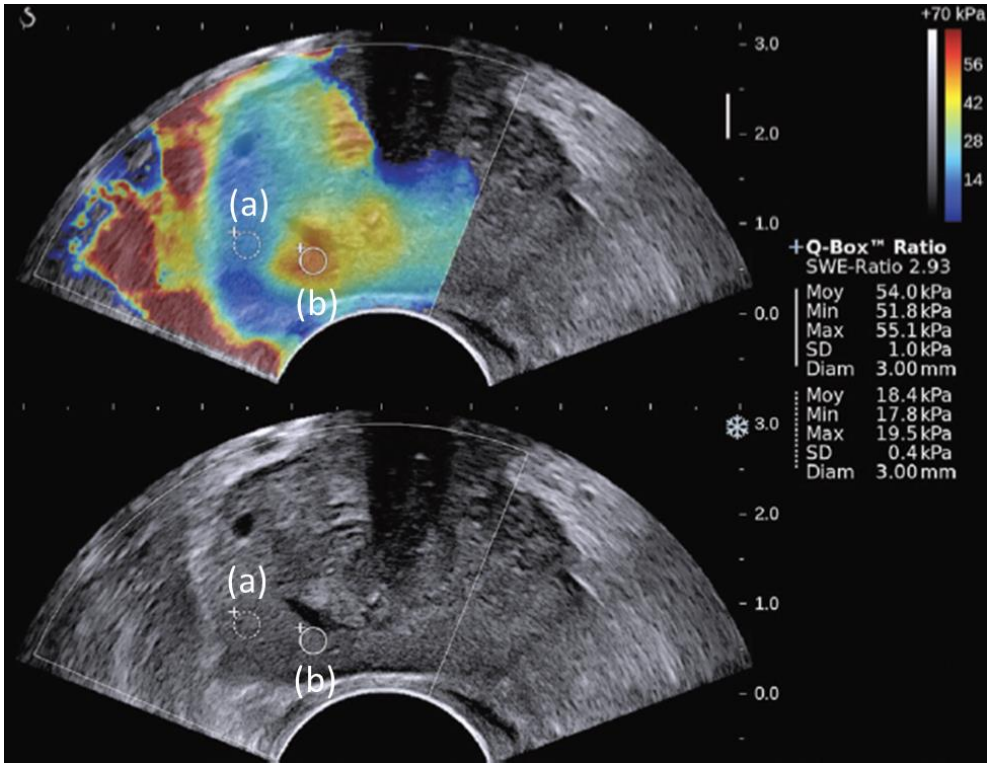

Figure 2.9 Shear wave elastography (SWE) (top) and B-mode ultrasound (bottom) images of (a) benign area outlined with dashed line, and (b) malignant area outlined with solid line. Adapted from Correas et al. 2015 [70].

Recent studies [70-74] are listed in Table 2.3 using SW to reveal PCa lesion. Due to the quantitative nature of this modality, elasticity value can be generated for the prostatic tissues. In 2012, Barr et al. [71] showed initial results of using a threshold elasticity value of 37 kPa to differentiate between benign and malignant prostate lesions. This produced a higher sensitivity (96 %) and specificity (96 %) than any of the SE imaging in Table 2.2. They also reported the Young's modulus of benign vs. cancer lesions were 21.5 ± 11.5 kPa vs. 58.0 ± 20.7 kPa respectively. Despite of the encouraging results of using elasticity as a diagnostic biomarker, it was a single small study with limited number of patients. In another research, Ahmad et al. [72] did not use a threshold value of elasticity, but applied a cut-off value of PSA level. Although they reported a high sensitivity and specificity, the Young's modulus value for both the benign vs. the cancer areas was more than two-fold of that from Barr et al. [71]. Woo et al. [74] assumed that the variance may be caused by the size of the prostate and technique of the operator.

As summarised in Table 2.3, a large overlap of the elasticity range is noticed between of benign and cancer lesion which suggests that not all cancers are stiff, and vice versa not all stiff lesions are cancerous. They could be calcifications or fibrosis. Different cut-off value was applied to these five major SWE researches. This resulted in a disparity of the assessment of the elasticity of prostate lesion. The inconsistent cut-off value also led to a variance of the accuracy of the SWE method. The worst performance for SWE in terms of sensitivity was 43% [74], and the best was 96% [71]. Few publications included the specific resolution of the system they used, but many cancers detected were larger than 2 mm. According to the latest report from Correas et al. [70], he performed well-designed analysis of the relationship between SWE accuracy and size of PCa lesion size. It was reported that SWE can efficiently identify cancers of 3 mm or larger with a high accuracy of 95%. However, the accuracy was 55% for a minimal foci size of 2 mm.

Although adequate experience and knowledge of both techniques are necessary for operating either elastography method, SWE does appear much easier to carry out than SE and requires less learning curve as no manual compression is needed. There is, however, minimal pressure applied to the end-fire transducer which requires bending to image the prostate. During SWE imaging, the whole prostate cannot be imaged at once due to the limited size of ROI, and the anterior transitional zone is rarely assessed because of the signal attenuation in large prostates. Other limitations of SWE also include the slow frame rate of one image per second and the delay to obtain image stabilization for each plane acquisition.

Table 2.3 Summary of shear wave elastography studies assessing malignancy of masses in the prostate.

Year	Reference	Patients	Gold standard	Cutoff parameter	Benign (kPa) [min – max]	Cancer (kPa) [min – max]	Sensitivity (%)	Specificity (%)	PPV (%)	NPV (%)
2012	Barr et al. [71]	53	Biopsy	YM 37 kPa	**21.5 ± 11.5 [30 – 110]**	**58.0 ± 20.7 [9 – 107]**	**96.2**	**96.2**	69.4	99.6
2013	Ahmad et al. [72]	50	Biopsy	PSA<20 µg/L PSA>20 µg/L	**74.9 ± 47.3**	**133.7 ± 57.6**	**90** **93**	**88** **93**	93 98	83 81
2014	Boehm et al. [73]	60	RP specimen	50 kPa	**42 [29 - 71.3]**	**88 [54 – 132]**	**80.9**	**69.1**	67.1	82.2
2014	Woo et al. [74]	87	Biopsy	YM 43.9 kPa	**33.2 ± 16.7 [2.3 - 150.1]**	**54.6 ± 46.0 [13.5 - 191.2]**	**43.0**	**80.3**	15.3	94.6
2015	Correas et al. [70]	184	Biopsy	YM 35 kPa	**21 (12) [8 – 218]**	**53 (43) [10 – 267]**	**96**	**85**	48	99

The Young's Modulus (YM) value of benign and cancer tissues are presented with mean standard deviation except for Correas et al. [70] with median (interquartile). Boehm et al. [73] reported the elasticity value in shear modulus.

2.2.4 Magnetic resonance elastography

The technique of elastography for use in conjunction with magnetic resonance imaging (MRI) is named magnetic resonance elastography (MRE). It measures the stiffness of the soft tissue by assessing the propagation of shear waves using magnetic resonance methods. Although elastography was introduced to the field of MRI shortly after its use in ultrasound, there have been far fewer publications on prostate imaging. Moreover, they are mostly limited to feasibility studies using prostate phantom [75, 76] or canine models [77, 78]. Thought potential has been shown in human *in vivo* studies, only a few clinical studies [79-81] have been conducted yet, and these were performed in a limited number of patients. It is difficult to decide the trade-off between the spatial resolution and penetration depth of the excitation of the shear waves. Also, MRE was too sensitive to the patient movement. These could limit number of human studies *in vivo*.

Kemper et al. [79] applied vibration to the pelvic bone of 7 healthy volunteers using an external oscillator. They reported the shear modulus of the central portion (2.2 ± 0.3 kPa) was lower than peripheral portion (3.3 ± 0.5 kPa) of the prostate gland. Li et al. [80] used transpelvic excitation with a study of 18 patients. It was reported that the elasticity of the lesions of PCa vs. healthy peripheral zone of the prostate was 6.55 ± 0.47 kPa vs. 2.26 ± 0.45 kPa. These MRE techniques were not capable of acquiring high signal-to-noise ratio (SNR) motion encoded MR signals at 1.5 T, and transmitting shear waves of sufficient amplitude into the prostate in a patient friendly manner.

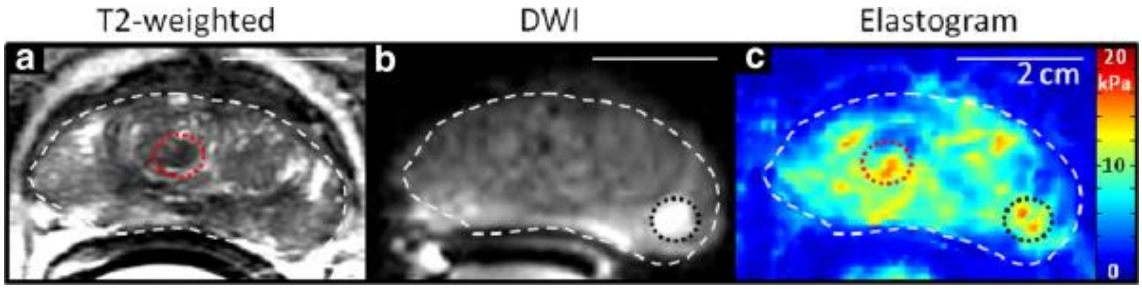

Figure 2.10 A patient was diagnosed with PCa before imaging. (a) T2-weighted image, (b) diffusion-weighted image, (c) MR elastogram. Two ROIs with abnormal signals were selected in a prostate outlined with a white dashed line. Adapted from Arani et al. 2013 [81].

Recently, Arvin et al. [81] conducted endorectal MRE and found that shear waves with frequencies up to 300 Hz could propagate across the entire prostate. The stiffness of central gland and peripheral zone of 8 volunteers was reported to be 19 ± 5 kPa and 17 ± 3 kPa respectively. As illustrated in Figure 2.10, a low signal in the T2-weighted image

(outlined with red circle), was correlated to a region of increased stiffness in the MRE image (outlined with red circle). Also, a region of restricted diffusion in the diffusion-weighted image (DWE) (outlined with dark circle), corresponded to a region of elevated stiffness in the MRE image (outlined with dark circle). However, histology was not performed as part of this study.

Alternatively, transurethral [77] and transperineal [82-84] approaches have yielded success in inducing shear waves. However, the anatomy of human is very different from canine and further study is required for the feasibility of transurethral method in human. In terms of the transperineal approach, Sahebjavaher et al. [84] recently presented an initial patient study originally with 18 patients by comparing the MRE results with whole-mount pathology, but the reconstruction maps were sensitive to small changes in the wave patterns in repeat cases. Moreover, long mechanical wavelength (between 15 and 35mm) limits the smallest detectable tumour with the excitation frequency of 70 Hz and trans-perineal excitation beyond 100 Hz were difficult or impossible because of the high attenuation of the waves near the perineum.

2.2.5 Summary of mechanical properties of prostate

In conclusion, these elastography studies have shown promise to use elasticity as a diagnostic biomarker for PCa, especially the quantitative elasticity assessment. However, currently in clinical care, elastography technique is not recommended to be used alone for routine care of PCa, and prostate biopsy [85] must always be combined with the results of the transrectal ultrasound B-mode and with other imaging techniques. Table 2.4 summarized the pros and cons of the current elastography modalities in the detection of PCa. Many cancer foci in the prostate gland has very small size less than 1 mm [10]. However, the spatial scales of current elastography techniques limit their applications to identify such small lesions. With improved diagnostic accuracy and advanced technology, quantitative elastography *in vivo* will hopefully reduce the number of painful TRUS biopsies. Further evaluation is required for whether elastography can predict grade of cancer, especially differentiate indolent from significant diseased lesion.

Table 2.4 Comparison of different elastography techniques employed in PCa detection.

Technique	Advantages	Disadvantages
US SE	• additional contrast to US • economic • most mature • portable	• observer disparity • learning curve required • qualitative
US SWE	• quantitative • easier to perform than SE • less learning curve • portable	• limited size of ROI • signal attenuation • slow frame rate
MRE	• quantitative • whole-prostate imaging	• sensitive to patient movement • limited study • signal attenuation • expensive • non-movable

US (ultrasound), SE (strain elastography), SWE (shear wave elastography), MRE (magnetic resonance elastography).

2.3 Elastography with Optical Coherence Tomography

Optical imaging techniques have also been proposed for elastography. In the landmark paper published in 1998, Schmitt et al. [86] first employed optical coherence tomography (OCT) [87] to measure local displacement induced by quasi-static compression. OCT is a 2D/3D imaging technique with micro-scale spatial resolution and millimetre-scale imaging depth [11]. Elastography with OCT is termed as optical coherence elastography (OCE). The spatial resolution of OCE ranges from several to hundreds of microns and the depth of view is the same or even larger (up to 10 mm) than OCT depending on the different methods used. Current clinical imaging such as ultrasound elastography and MRE delineates the imaging scale at whole-organ level, whilst laboratory imaging such as atomic force microscopy (AFM) [88, 89] and optical tweezer [90] targets at cellular level. OCE is potential to bridge the gap between organ-level and cellular-level imaging of the biomechanical properties.

This thesis intends to introduce this kind of OCE technique for the characterization of PCa. Although this technique is a comprehensive system and has advanced a lot in the recent years with many different variations, this section aims at providing a general background of this technique. Similar to ultrasound elastography, OCE is also consisted of two parts, namely excitation and detection. It generally has an external or internal excitation approach to deform the tissue and an OCT-based detection method to measure the corresponding tissue response. Since the detection methods are based on OCT (the main part of OCE), this section starts with an introduction to OCT explaining the working process and imaging resolution. In the second part of this section, the displacement detection methods and prominent loading methods will be discussed.

2.3.1 Optical coherence tomography

The working principle of optical coherence tomography (OCT) is analogous to ultrasound imaging except that OCT uses near-infrared light rather than acoustical waves. The speed of sound is ~1500 m/s, whilst that of light is ~$3x10^8$ m/s. In order to achieve a 10-µm resolution, a time resolution of ~30 femtosecond ($30x10^{-15}$ s) is required [91]. It is not possible to use direct electronic detection as ultrasound does, instead high-speed optical gating, optical correlation, or interferometry must be used for the measurement of signal in OCT setup. Owing to the use of light, there is no need for direct contact with tissue or transducing medium (ultrasound gel), which makes OCT to be a non-invasive and noncontact method especially suitable for clinical application. The evolution of OCT technology originated from time-domain systems to spectral-domain systems.

Time-domain OCT

OCT is essentially based on low-coherence interferometry (typically a Michelson interferometer) by measuring the magnitude and echo time delay of backscattered light from internal microstructures in tissues [92]. Time-domain OCT (TD-OCT) is defined if the interferometer output is detected as the reference arm is scanned. As shown in Figure 2.11, the incident light from a low coherence light source is split into two beams, namely a reference beam and a sample beam. The light reflected by the scanning reference combines with the backscattered light from the sample travelled with different distances. An interference pattern only occurs when the two path lengths are matched to within the coherence length.

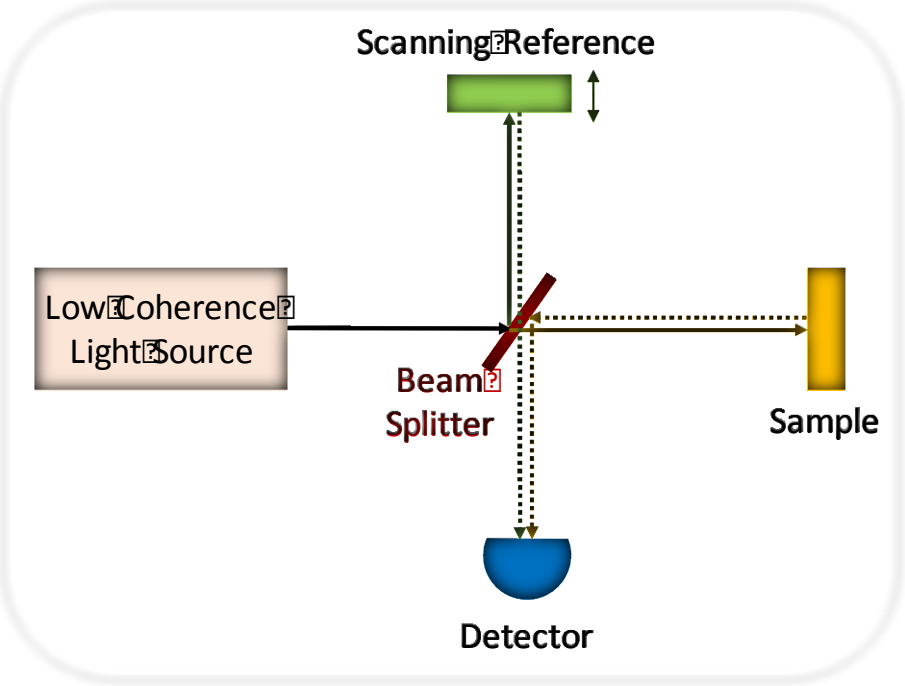

Figure 2.11 A schematic diagram of a typical time-domain OCT with a classic Michelson interferometer.

In TD-OCT, the reference mirror is mechanically stepped to change the optical path length and produce A-scans (axial scans) which are the measurement of backscattered intensity versus depth (axial position). Early OCT instruments relied on TD-OCT using a low coherence light source and interferometer with a scanning reference arm. However, such designs are not suitable for 3D *in vivo* imaging with low sensitivity and long acquisition time.

Fourier-domain OCT

Detection of interference signal is also possible in the Fourier domain using a low coherence interferometer (implemented using fibre optics) with a broadband light source. The measurement of the interference spectrum is performed with a spectrometer and a high-speed line scan camera. This method was first proposed by Fercher et al. [93] in 1995 and defined as spectral-domain OCT (SD-OCT). In Figure 2.12 with a schematic of a typical SD-OCT, a broadband light source is divided into two beams. The time offset between the fixed reference beam and the sample beam is determined by the path length difference, which is the depth-related information of the structure in the tissue. The interference spectrum of the two beams is measured by the spectrometer as a function of wavelength. It is then read by a computer and numerically resampled from wavelength to frequency or wavenumber. Therefore, the interference spectrum is a spectral modulation

rescaled as a function of frequency. Lastly, the depth-resolved information is reconstructed by performing a fast Fourier transform (FFT) on the interference signal.

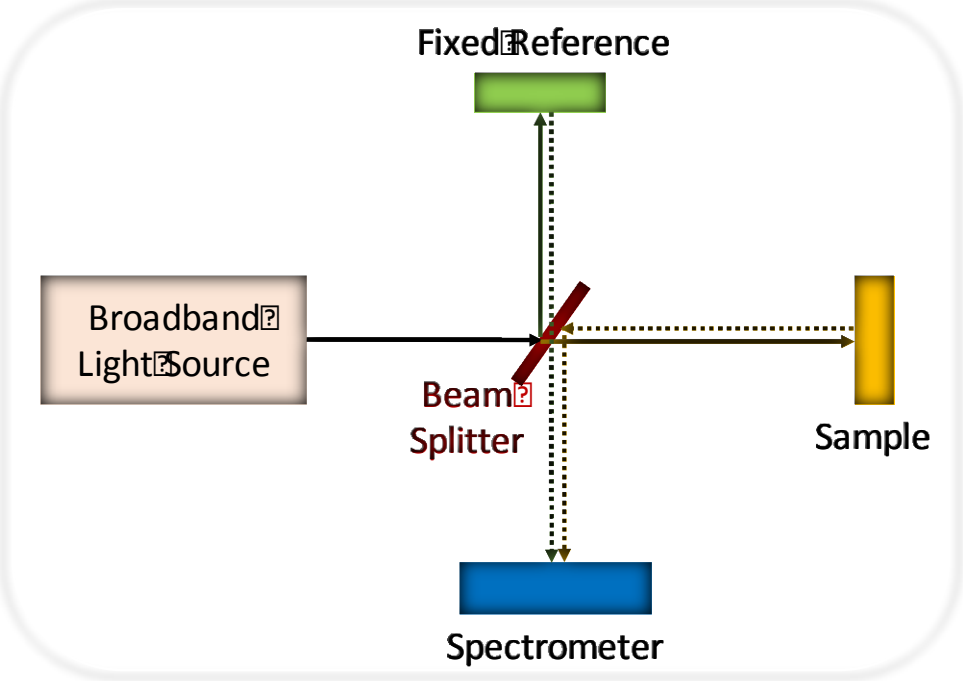

Figure 2.12 A schematic diagram of a typical spectral-domain OCT set up.

In SD-OCT, A-scans (axial scans) are generated by the measurement of the echo magnitude and echo delay of the backscattered light from the tissue, where the scan rate is determined by the line scan rate of the high-speed camera. A series of A-scans are termed B-scan (cross-sectional image) which is acquired by transversely scanning the OCT beam across the sample. A phase-sensitive image can be generated by calculating the phase difference between points at the same depth in adjacent A-lines. SD-OCT can also realize a volumetric imaging, and 3D images can be generated by raster scanning with a serious of B-scans. SD-OCT has been proved to have a much higher sensitivity and speed over TD-OCT [94] owing to the simultaneous measurement of all the echoes of light and without the need for mechanically stepping the reference arm. The other form of Fourier-domain OCT is known as swept-source OCT (SS-OCT) which uses photodetectors and an interferometer with a frequency swept, narrow-bandwidth light source.

Image Resolution

Image resolution is essential for the performance of an imaging system. In OCT imaging, the axial and transverse resolution are determined independently, which makes OCT superior to conventional and confocal microscopy. In microscopy, the axial resolution is determined by the depth of field, while in low-coherence interferometry the axial resolution [91] is mainly governed by the coherence length of the light source. The coherence length is given by the full-width at half-maximum (FWHM) of the autocorrelation function. Assuming a light source with a Gaussian-shaped spectrum, the axial resolution, Δz, is

$$\Delta z = \frac{2\ln 2}{\pi} \cdot \frac{\lambda^2}{\Delta\lambda} \approx 0.44 \cdot \frac{\lambda^2}{\Delta\lambda}$$

where $\Delta\lambda$ is the FWHM bandwidth of the Gaussian spectrum and λ is the centre wavelength of the light source. It is noted that the axial resolution is inversely proportional to the bandwidth of the light source, hereby the light sources with broad bandwidth are preferred for microscale axial resolution. It is important to know that the actual resolution within the imaged tissue sample varies by different degree of dispersion, absorption and scattering of the sample.

For the transverse or lateral resolution of OCT imaging, as in conventional microscopy, it is governed by the focal spot size, which is defined as the diffraction limited minimum spot size of the focused Gaussian beam in the sample arm. The transverse or lateral resolution, Δx, is the diameter of the beam at its waist, which is given by $2\omega_0$ (two times the beam waist)

$$\Delta x = 2\omega_0 = \frac{4\lambda}{\pi} \cdot \frac{f}{d} = \frac{4\lambda}{\pi} \cdot \frac{1}{2NA} \approx 0.63 \cdot \frac{\lambda}{NA}$$

where ω_0 is the beam waist of the Gaussian beam, λ is the center wavelength of the light source, f is the focal length of the objective lens, d is the spot size of the incident beam on the objective lens, and NA is the numerical aperture of the objective lens. The transverse resolution is inversely proportional to the numerical aperture. Therefore, high transverse resolution requires focusing objective lens with a large numerical aperture.

At the same time, the transverse resolution, Δx, also governs the depth of focus, or the confocal parameter, b, which is expressed as (two times the Rayleigh range, z_R)

$$b = 2z_R = 2 \cdot \frac{\pi {\omega_0}^2}{\lambda} = 2 \cdot \frac{\pi\left(\frac{\Delta x}{2}\right)^2}{\lambda} = \frac{\pi\Delta x^2}{2\lambda} \approx 1.57 \cdot \frac{\Delta x^2}{\lambda}$$

where $\omega_0$is the the beam waist of the Gaussian beam, Δx is the transverse resolution, and λ is the center wavelength of the light source. Since the depth of focus is proportional to the transverse resolution, the finer the transverse resolution, the smaller the depth of focus will be. There is a trade-off between the two.

For the OCT penetration depth, it is predominant limited by light scattering within sample. The scattering can be defined as $1/\lambda_c^k$, where the coefficient k is dependent on tissue morphology [95]. In ophthalmology, light source with wavelength of ~800 nm is mostly used. The eye is transparent with minimal attenuation and scattering, which makes easy optical access to the anterior segment and the retina. While for other biological tissue imaging, the optimum wavelengths are between ~1300 and ~1500 nm applied for a deeper penetration depth of 1 to 2 mm.

2.3.2 Optical coherence elastography

2.3.2.1 Displacement detection

Speckle-tracking method

The early OCE studies relied on the pioneer work of Schmitt et al. using the speckle-tracking method with cross correlation technique to detect the tissue response after loading. Speckle is the fine-scale, random, mottled intensity pattern generated by the sub-resolution sample scatters present in all coherent imaging systems. The use of speckle for displacement detection is because each speckle realization is subjected to the precise location of scatters within the tissue. In this case, the tissue displacement is assessed by the shift of speckle pattern between sequential B-scans with the cross-correlation.

However, the minimum displacement between measurements is about half of the speckle size [96]. Such process decreases the spatial resolution of displacement measurement, which is much lower than the OCT imaging. One benefit of speckle tracking is that both the axial and shear motion can be tracked simultaneously. Nevertheless, three-dimensional tracking is not demonstrated using speckle tracking. Although it has been realized in ultrasound elastography and MRE, the long acquisition time has limited the application. OCE has higher acquisition speed than ultrasound, and 3D tracking using OCE may provide additional information for shear strain in anisotropic tissues.

Phase-sensitive OCT

Instead of using changes in the intensity information, the other main method for displacement detection, phase-sensitive OCT, obtains the phase information from complex OCT signal. Phase-sensitive technique was first proposed for the measurement of flow velocity based on the Doppler shift [97]. After the advent of Fourier-domain OCT, it has been a predominant method used for displacement detection in OCE. After mechanical loading, the axial displacement produces a phase shift between two A-scans obtained from the same lateral positions. The change in axial displacement, Δu_z, is given by

$$\Delta u_z = \frac{\Delta \emptyset \lambda}{4\pi n}$$

where $\Delta \emptyset$ is the phase shift, λ is the wavelength of the light source, and n is the refractive index of about 1.4. As noted in the equation above, only the axial displacement can be detected. The minimum phase difference that can be measured is determined by the phase sensitivity of the OCT system, which is related to the signal to noise ratio (SNR). In practice, the typical displacement sensitivity is between 0.1-1 nm [91].

A major limitation of phase-sensitive detection is the ambiguity caused by phase wrapping. It is possible to unwrap the phase, but is sensitive to noise. This can be improved by intensity threshold and weighting the phase difference to give preference to the ones evaluated from pixels with high SNR. On the other hand, faster acquisition can be applied in dynamic loading to mitigate phase wrapping. Additionally, robust algorithms are desirable for unwrap phase correctly.

Table 2.5 Comparison of different displacement detection techniques employed in OCE.

Technique	Axial resolution	Lateral resolution	Minimum displacement	Maximum displacement
Speckle tracking	5-10 times OCT	5-10 times OCT	~half pixel size	~half OCT resolution
Phase sensitive	Same as OCT	Same as OCT	~20 pm	~half source wavelength

Phase-sensitive is superior to speckle-tracking method since the former one has larger displacement dynamic range, about 20-fold greater than for the latter one [98]. Also, the spatial resolution of phase-sensitive OCE is comparable to the underlying OCT system.

The emerging of phase-sensitive OCT detection enabled OCE techniques to reconstruct the biomechanical properties of tissues with high accuracy and high sensitivity to tissue displacement. Hereby, phase-sensitive OCE will be applied to this research thesis, and details of the instrument configuration will be provided in Chapter 3.

2.3.2.2 Loading methods

There are a wide group of methods employed in OCE techniques. These methods can be broadly classified based on how the excitation induced, whether it is static or dynamic load, localized or global applied, external or internal loaded, elastic travelling or standing waves generated, and contact or noncontact method. A discussion will be included in each method to stress the advantage and disadvantage. The choice of a loading method is largely depended on the requirements of the application.

Surface acoustic wave method

Surface acoustic wave (SAW) method is an emerging OCE technique based on the propagation of mechanical wave along the tissue surface. In order to induce SAW, various loading methods can be used, including contact methods [99, 100] such as a metal rod as illustrated in Figure 2.13 (a) or a piezoelectric transducer, and noncontact methods [101-103] such as pulsed laser as illustrated in Figure 2.13 (b) and a focused air puff. Such non-destructive loading has remarkable potential in delicate tissues such as cornea.

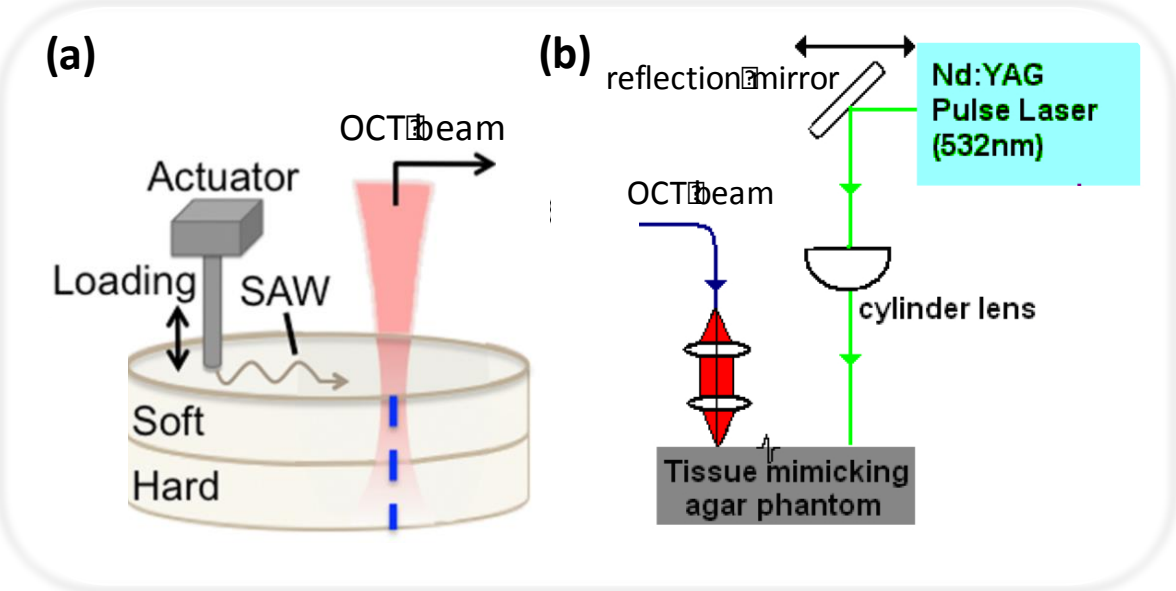

Figure 2.13 A schematic of surface acoustic wave (SAW) generated using (a) contact loading and (b) noncontact loading. Adapted from Kennedy et al. 2014 [11] and Li et al. 2011 [102].

When such dynamic load is applied on the surface of the sample such as phantom or tissue, a SAW is generated. If the load is perpendicular to the surface, isotropic elastic material behaves as Rayleigh waves [104] which contains both longitudinal and transverse motion. For a homogeneous sample, the relationship between the Young's modulus, E, and the phase velocity, c_p, of SAW can be expressed as [100]

$$E = \rho {c_p}^2 \, (2.618 + 1.332v)$$

where v is the Poisson's ratio about 0.5, and ρ is mass density of the sample.

For layered sample with different stiffness of each layer, the possible effect of wave dispersion needs to be considered, which is related to the depthwise distribution of the sample elasticity. In this case, the effective penetration depth, z, can be approximated to the corresponding wavelength, λ_s, using the equation below

$$z \approx \lambda_s = \frac{c_p}{f_s}$$

where c_p is the phase velocity of SAW, and f_s is the SAW frequency. Due to the variation of elasticity with depth, SAW with lower frequency penetrates to deeper layers, whilst that with higher frequency is limited in the superficial layers. Using the abovementioned two equations, the SAW velocity at different depth can be used to achieve depth-resolved quantitative measurement with the mapping of Young's modulus. Using a homemade metal-rod shaker, Figure 2.14 illustrated that a hard nodule deep (1.5 mm) below the human forearm skin surface was identified with a good contrast with the surrounding normal tissue.

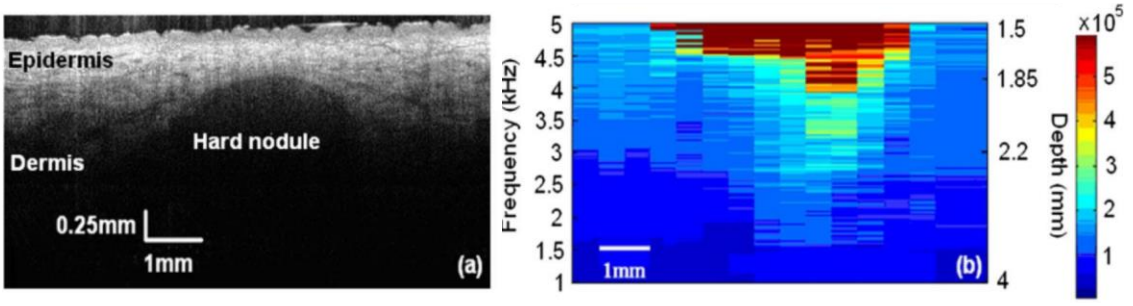

Figure 2.14 (a) OCE structure image and (b) the resulting elastogram with SAW OCE of *in vivo* human forearm skin with a hard nodule in the middle. Adapted from Li et al. 2012 [99].

The main advantage of employing SAW method is capable to measure the elasticity beyond the standard OCT imaging limit, which suggests the possibility of OCE to

implement in dermatology. However, the location of the elasticity might have errors due to the approximation between the depth and the wavelength. Also, the long wavelength of SAW leads to a lower lateral resolution (~500 μm). Another drawback of this method is that the elasticity measurement of superficial layer of the tissue may not be possible since that the minimum depth can be probed is limited by the maximum frequency of SAW can be detected.

Shear wave method

Shear wave (SW) is mainly generated using dynamic loading with a fixed frequency [105, 106] or focused impulse excitation with a short pulse duration [107-109], as well as mechanical loading with a broad frequency range [110]. Analogous to ultrasound shear wave elastography, the relationship between the tissue Young's modulus, E, the shear modulus, G, and SW velocity, c_s, can be written as

$$E = 2(1 + v)G = 3G = 3\rho {c_s}^2$$

where v is the Poisson's ratio around 0.5, and ρ is mass density of the sample. Since both the SAW and bulk SW can may present at depths, differentiating SW from SAW remains a problem. Song et al. [106] employed point loading at the side of the sample by a slender stainless-steel rod tip fixed on a stacked piezoelectric actuator (5 cycle bursts of 5 kHz sine waves) as presented in Figure 2.15 (a).

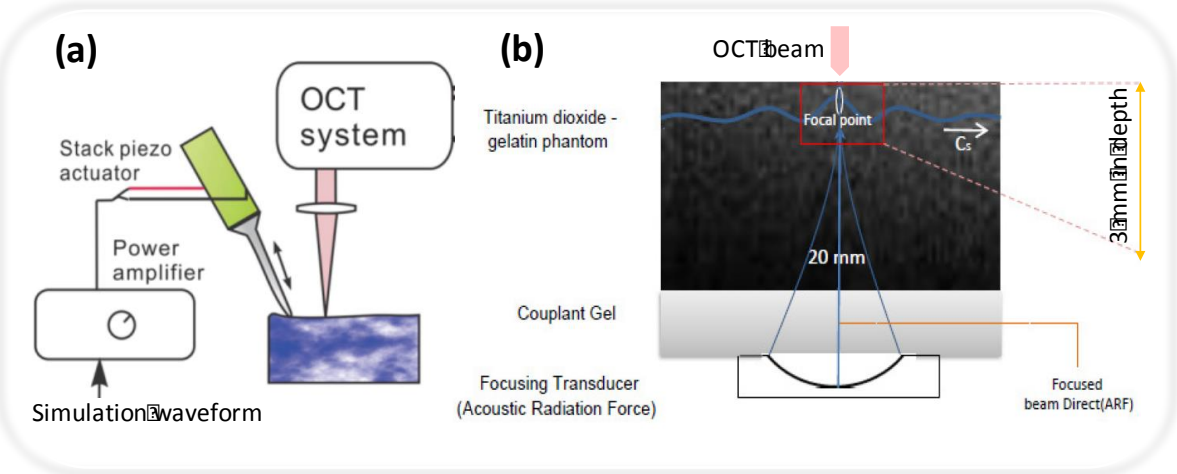

Figure 2.15 A schematic of the shear wave (SW) generated by (a) a piezoelectric actuator at 5 kHz, and (b) a focused ultrasound beam using a 20 MHz piezoelectric transducer. Adapted from Song et al. 2013 [106] and Razani et al. 2012 [109].

SAW was expected to attenuate rapidly with depth by operating the transducer in the kilohertz range. Thus, the detected sub-surface lateral motion was considered to directly relate to bulk SW behaviour. As shown in Figure 2.15 (b), a 20 MHz piezoelectric transducer produced a focused ultrasound beam in burst mode [109] within the titanium dioxide-gelatine phantom. The SW travelled in the direction indicated by the white arrow. The propagation was radially outwards from the focal point and normal to the direction of the focused beams.

For a homogenous sample where the spatial variation of elasticity is larger than the SW length, the SW with a specific frequency will propagate at a constant velocity. Here, the linear relationship between the phase delay, $\Delta\emptyset$, and the distance along a wave path, Δr, can be expressed as

$$c_s = \frac{\omega \Delta r}{\Delta \emptyset}$$

where c_s is the SW speed, and ω is the angular frequency. By applying the two equations above and similar setup in Figure 2.15 (a), the elasticity map can be reconstructed as shown in Figure 2.16 (b) [105]. The stiff inclusion was identified within the agar phantom with clear boundary as expected. However, the linear fitting of the phase delay curve performed over ~500 μm, which limited the lateral resolution of SW OCE. A drawback of such SW setup is that it requires direct contact with tissue, while SW generated by non-destructive radiation source as Figure 2.12 (b) might be an option for future biomedical applications. Since SW methods in OCE are still in early stage of development, many of the papers published limit in the feasibility study in phantom [105] and *ex vivo* studies such as cardiac muscle [107] and carotid artery [108].

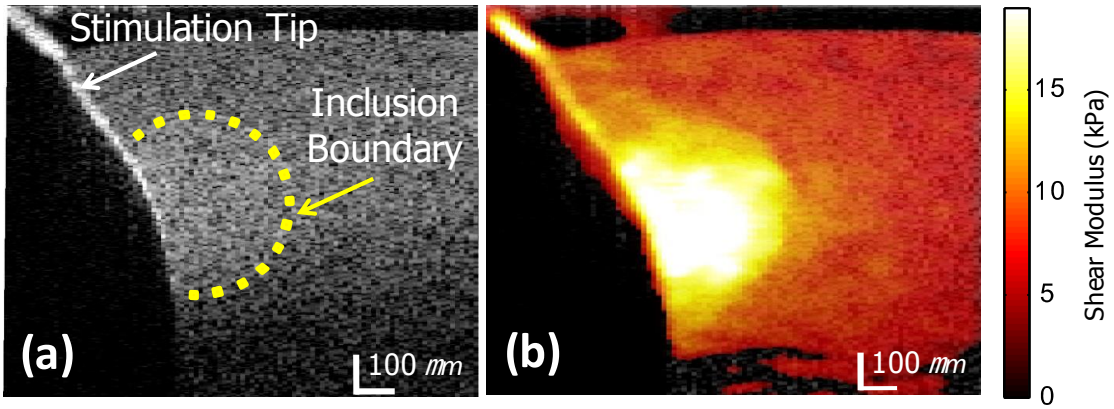

Figure 2.16 (a) B-mode structural image, and (b) shear modulus mapping of agar phantom with inclusion. Adapted from Song et al. 2013 [105].

Compression method

Compression elastography is the most straightforward method to implement in OCE and also the most mature one in probing prostate mechanical properties with ultrasound elastography as reviewed above. Schmitt et al. [86] first explored elastography on a scale substantially smaller than previous studies utilizing a piezoelectric actuator and a circular glass cover slip glued on top of its ring-shaped head. The actuator ensured to provide displacements up to 100 μm in the linear range, and the glass attempt to serve as an optical window and a compression plate. In this case, the mechanical excitation is a static, uniform, and whole-range compression, which had been the only method utilized until 2008. However, it requires direct contact with tissue by loading the compression via the surface of the glass.

Analogous to ultrasound elastography, the local strain is estimated by measuring the change in displacement over an axial depth range. The elastogram reconstructed is a map of this local strain. Since the direct measurement of the local stress within the sample is not possible, the elastic modulus cannot be generated from the local strain. Nevertheless, this pioneer study with the strain results from gelatine scattering models, pork meat, and intact skin opened the world of developments of OCE technique and possible applications of this technique in both research and medical areas.

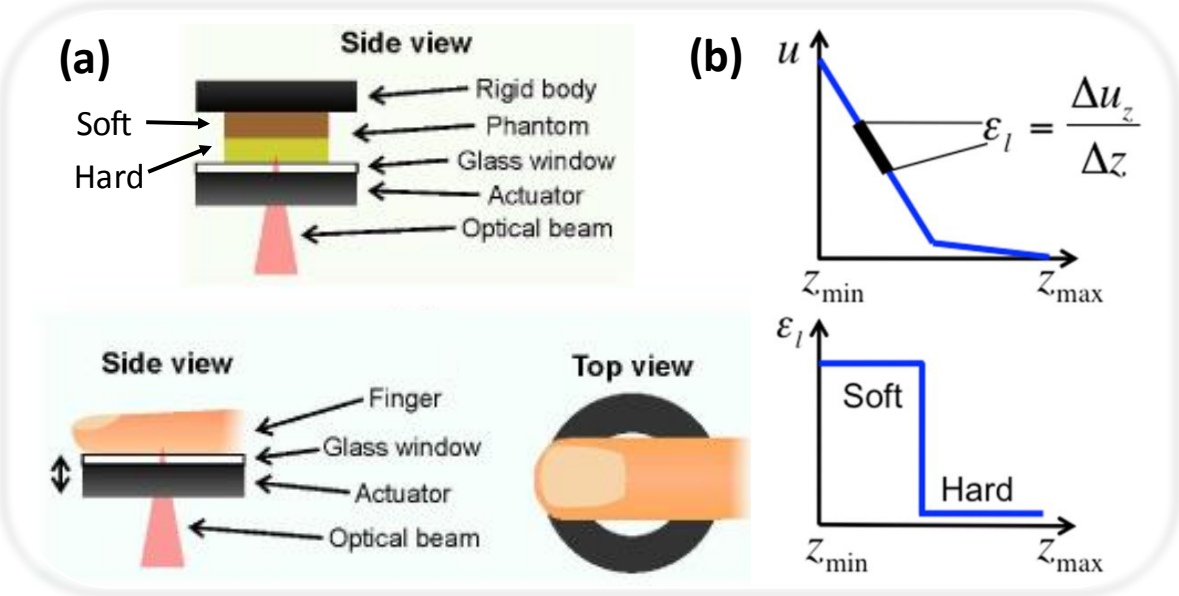

Figure 2.17 A schematic of compression loading method using (a) a ring actuator and (b) resulting displacement (u) vs. depth (z) and corresponding strain (ε_l). Adapted from Kennedy et al. 2014 [11] and 2009 [111].

Innovated by Schmitt's work, dynamic loading has also been used in compression OCE. Kennedy et al. [111] applied dynamic loading by a ring actuator to demonstrate a feasibility study in bilayer silicone phantoms and *in vivo* human skin. A schematic of the sample arm setup is shown in Figure 2.17 (a). The ring actuator in contact with the sample surface had an aperture of 15 mm and a resonance frequency of 45 kHz. In Figure 2.17 (b), the vibration amplitude was measured as resulting displacement and the dynamic strain was calculated according to the change in vibration amplitude versus axial depth, similar to static elastography loading. Thus the soft phantom had larger strain than the hard phantom.

With faster acquisition speed [112], a significant improvement of OCE resolution was observed in Figure 2.18 compared to the previous result [111]. In Figure 2.18 (a), strong contrast was visible between different layers of skin, where the stratum corneum has a thickness of ~300 µm. It was noted that the living epidermis had a higher strain the strain rate than the stratum corneum as shown in Figure 2.18 (b). The OCE signal with colour map was superimposed on the OCT signal as illustrated in Figure 2.18 (c). Compression OCE was also capable of a 3D OCE imaging of human skin *in vivo* [112]. However, the lack of direct measurement of absolute elasticity may limit its potential applications.

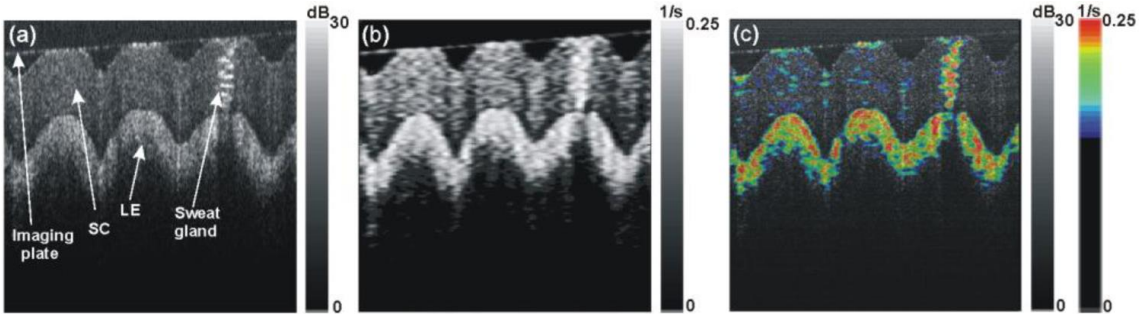

Figure 2.18 (a) OCT, (b) OCE, and (c) overlaid images of skin from the tip of the middle finger. SC (stratum corneum), LE (living epidermis). Image size is 1.4 x 1.4 mm. Adapted from Kennedy et al. 2013 [112].

Summary of loading methods

The difference of the abovementioned loading methods is compared in Table 2.6, wherein the dynamic range was calculated by dividing the maximum to minimum measured parameter. Among them, compression method stands out with high resolution and larger dynamic range. SAW and SW can only measure bulk elasticity and the lateral resolution is lower due to the long wavelength of the mechanical wave. For the prostate elastography imaging, the aim is to obtain subtle changes in stiffness of biopsy tissue, which is usually

1-2 mm in diameter. However, the current compression method is not quantitative. Hereby in this research thesis, compression method will be employed with modification added to the traditional instrument to achieve quantitative measurement of prostate tissue with high resolution. Details will be provided in Chapter 3.

Table 2.6 Comparison of different loading techniques employed in OCE.

Technique	Axial resolution	Lateral resolution	Measured parameter	Dynamic range	Quanti-tative
SAW	N/A	500-1000 µm	Phase velocity, c_p	~450 [99]	Yes
SW	N/A	500 µm	Phase velocity, ${c_s}^2$	~14 [106]	Yes
Compression	40-120 µm [98]	Same as OCT	Local strain, ε_l	~660 [113]	No

2.4 Concluding Remarks

To conclude this chapter, it lays a foundation for the whole research work by providing three major bricks. The first brick is the background of PCa disease and current clinical diagnostic methods, which serves as the motivation for this thesis. After finishing the disadvantage of DRE, it begins the second brick with current researches of prostate elastography techniques. Promises is presented with elastography but resolution remains a challenge. Finally, the last brick is an introduction of high-resolution OCT elastography. Comparison was provided of the different OCE techniques, and phase-sensitive compression OCE is proposed to be employed for this thesis. Further modification of the instrument follows in the next chapter.

Chapter 3. Evaluation of Fixative Effects on Tissue Stiffness with Vibration Optical Coherence Elastography

This research thesis aims at quantitative evaluation of degree of malignancy of human prostate cancer using vibration optical coherence elastography. It is based on the assumption that all the prostate biopsies are fixed to the same level before the vibration optical coherence elastography scanning. Accordingly it will firstly evaluate the fixative impact on the biological tissues using the vibration optical coherence elastography. The details of this fixative study will be provided in this chapter.

This chapter is also going to introduce the optical coherence elastography with vibration method, where the system configuration and parameters will be detailed, as well as a brief explanation of the working principle.

3.1 Introduction

Fixation of biological tissues is a crucial step for preparing specimens for the histopathological examination under a microscope. Besides of prohibiting tissue from degrading, fixation enables easier handling, prolonged storage and precise sectioning of tissues to uniform morphology. By far the most commonly used fixative is formaldehyde (CH_2O). Aldehyde can form an increased number of inter- and intra-fibrillar cross-links of primary amine groups of polypeptide chains [114-116]. Consequently, covalent chemical bonds stabilize soluble proteins to insoluble structural proteins and the whole structure is given mechanical strength. A saturated 37% – 40% (w/v) formaldehyde water solution is formed by dissolving the gaseous formaldehyde in water, i.e. 100% formalin. On top of that, a small amount of methanol is usually added as a stabilizer to prevent oxidation and polymerization.

In practise, ten-percent (v/v) formalin solution containing 4% (v/v) formaldehyde widely used universal fixative for routine histologic use in many laboratories and in a diagnostic setting for pathologic purpose. Ten-percent formalin solution is produced by diluting one part of stock 37%-40% (w/v) formaldehyde solution with nine parts of water. Alternatively, phosphate buffer at neutral pH is usually used for diluting called 10% neutral buffered formalin (NBF). Routinely tissues are required for a period of 24 to 48 hours [117] embedded in the formalin for a proper fixation. It is assumed that this period

is enough for the fixatives to diffuse into the tissue and the chemical reactions of formaldehyde with various components to finish. The volume of the formalin solution is depended on the size and thickness of tissues [118], which is usually in excess of 20 times the volume of the tissue.

Formaldehyde is considered dangerous and toxic and as a result concerns have been raised about the potential health risks of traditional formalin embalming techniques [119]. The Thiel method is a new soft-fix embalming technique. The main components of Thiel solution are water, glycol, salts, and very low concentrations of harmful components: formaldehyde, chlorocresol and morpholine. Due to the high concentration of salt components, proteins in the tissues are denatured, leading to a homogenization of the tissues [120]. The embalming procedure consists of intravascular injection and followed by immersion in Thiel fluid for at least 2 months. The Thiel embalming method was first developed by anatomist Walter Thiel in 1992 [121]. It has been modified since then and is currently utilised by the Centre for Anatomy and Human Identification (CAHiD) at the University of Dundee [119]. According to recent reports [118, 119], Thiel embalming can provide long-lasting preservation with impressive flexibility and tissue quality, especially for the application in microvascular exercise.

In addition to the successful application on histopathology, fixed and preserved tissue is also served as a useful tool for clinical training and biomedical instrumentation design [122, 123]. In this case it is not only the tissue morphology that need to be considered but also its mechanical properties since they have significant influence on the design and performance of such instruments. Fixation induced mechanical property changes have attracted attention and studies have been carried out to investigate the effects of tissue preservation methods on the mechanical properties of different kinds of tissues using traditional mechanical loading methods [122-128]. However, to the best of our knowledge there are some limitations regarding to the current studies of the fixation effects to mechanical properties of tissue: 1) the traditional loading method cannot provide real time elasticity change since it is a relatively time consuming technique, thus the detailed elasticity change with precise time line during the fixation procedure cannot be determined; 2) the degree of influence of different fixation methods to mechanical properties in relation to different kinds of tissues remains unknown.

Optical Coherence Tomography (OCT) is an optical imaging technique that enables high-resolution, cross-sectional imaging of tissue microstructures, *in vivo*, non-invasive and in real time [86, 111, 112, 129-141]. Optical Coherence Elastography (OCE) has become

increasingly utilised as it carries the potential to provide ultra-high resolution imaging which not only has the ability to detect subtle changes in material structure but also can characterise materials based on their mechanical properties (stiffness). The basic concept of OCE is to stimulate vibration in the target tissue and measure the vibration amplitude corresponding to strain. Areas with higher vibrating amplitude indicate a softer material while areas with lower vibrating amplitude indicate a stiffer material [12, 111, 112]. Compared with other elastography methods, i.e. ultrasound and magnetic resonance elastography, OCE is capable of providing ultra-high microstructural and mechanical characterization, and therefore has the potential to resolve the microscopic heterogeneity in the assessment of mechanical properties of tissues. OCE also has high acquisition speed with 2D image acquisition rates in the range of 10s to 100s of kHz, and potentially even higher, which has great potential to fulfil real-time 2D elastography. OCE has high mechanical sensitivity which enables displacement detection up to picometers [142]. It has the potential to detect differentiations between small alterations in mechanical properties. The mechanical properties of tissue can be estimated using OCE while providing the ultra-high resolution with elastography of OCT images.

This chapter explores the use of quantitative OCE to provide quantitative mechanical property changes induced by fixation procedure. To achieve this goal, the elasticity changes of five different kinds of tissue were compared under the fixation of 10% diluted formalin and Thiel fluids. A vibrating shaker was used to generate phase change in the sample. Phase sensitive optical coherence tomography (PhS-OCT) was utilized to record the phase change of samples in a precise controlled time line, from which the time impact of quantitative Young's modulus was deduced. The technique has great potential application in the further development of fixatives for better maintenance of tissue properties. The results also have significance on influencing fixative choice in biomedical instrument design.

3.2 Materials and Methods

3.2.1 Sample preparation

To investigate the time impact of elasticity by formalin and Thiel fluids, five different tissue types were submerged into each fixative from fresh. The tissue types were porcine fat, porcine liver, chicken breast, chicken tendon and chicken cartilage. For each tissue type, 5 samples were prepared for the experiment. Random samples of chicken breast and porcine fat were taken with a 16-gauge biopsy needle. The chicken tendon samples were

selected by directly dissecting a chicken drumstick. For the porcine liver and the chicken cartilage, the random samples were cut and trimmed with a scalpel. The sample size was approximately 2 mm in diameter and 1cm in length.

The two fixative solutions chosen were 10% formalin dilution and Thiel embalming fluids. Thiel embalming fluids are primarily salt based with boric acid and contain a very low concentration of formalin. The solution volume applied to each sample is ~30 ml. For the formalin treatment, the samples were immersed in 10% formalin dilution for 6 months. Thiel fluids utilised in this study are arterial infusion fluid, venous infusion fluid and tank fluid [119] formulated in the Centre for Anatomy and Human Identification (CAHiD) at the University of Dundee. The composition of each fluid is demonstrated in Table 4.1. For the Thiel treatment, the samples were submerged in a mixture of 50/50 arterial and venous infusion fluids for 24 hours then transferred to tank fluid for the following 6 months. All fixation and experiments were conducted at room temperature.

Table 3.1 Composition of Thiel Embalming Fluids as Used in this study

	Arterial and Venous infusion (50/50) mixture	Tank fluid
Hot tap water [mL]	535.5	850
Boric acid [g]	16.35	24
Ammonium nitrate [g]	107.1	80
Potassium nitrate [g]	26.75	40
Sodium sulphite [g]	42.35	54
Glycol [mL]	159.55	80
Glycol/Chlorocresol mix [mL]	34.95	15
Formalin 37% [mL]	52.35	16
Morpholine [mL]	15.45	-
Alcohol [mL]	136.6	-
Total volume [mL] ca.	1000	1000

Imaging experiments were performed after 0, 10 minutes, 20 minutes, 30 minutes, 40 minutes, 50 minutes, and 1 hour, 70minues, 80 minutes, 90 minutes, 100minutes, 110 minutes, 2 hours, 3 hours, 4 hours, 5 hours, 6 hours, 7 hours, 8 hours, 9 hours, and 1 day, 2 days, 3 days, 4 days, 3 months, 6 months after immersing the tissues in the fixatives.

During the OCE scanning, the tissue sample was taken out of the fixative and placed on 2% agar (mixed with 5% whole milk to produce a scattering background) phantom with a thickness of ~8 mm which acted as an elasticity reference [12, 143]. Each sample was scanned at the three clearly marked positions at each time interval. The scanning process took approximately 2 minutes per sample. The sample was kept moisture during the scan and returned to the fixative immediately after the procedure.

3.2.2 System configuration

The OCE system consists of two main parts: signal detection and vibration stimulation. For signal detection, a phase-sensitive optical coherence tomography (PhS-OCT) with spectral-domain configuration is adapted to measure the displacement of tissues. For vibration stimulation, a magnet shaker is used to produce vibration within the sample. The configuration of the main components in the vibration OCE system is illustrated in Figure 3.1.

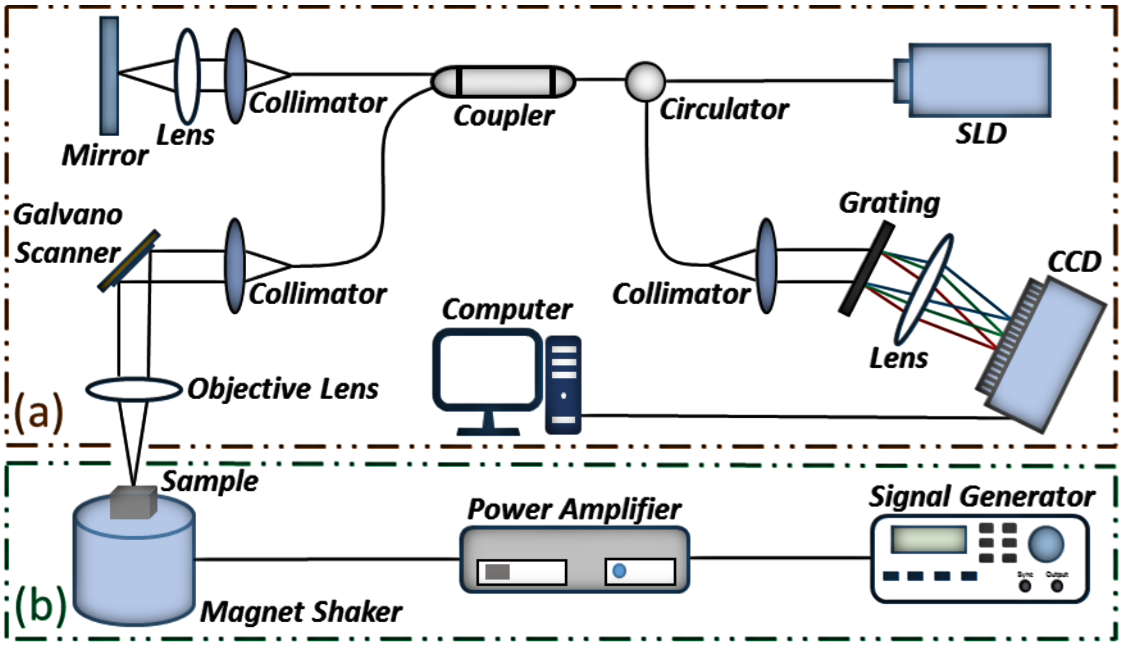

Figure 3.1 A schematic of system setup of the vibration OCE system consisting of (a) signal detection using PhS-OCT and (b) vibration stimulation using a shaker. SLD (superluminescent diode), CCD (charged coupled device) line-scan camera.

Phase-sensitive optical coherence tomography

As shown in Figure 3.1 (a), the PhS-OCT system employs a superluminescent diode (SLD, S5FC1021S, Thorlabs) as a broadband light source, with a centre wavelength of ~1302 nm and bandwidth of ~85 nm. A three-port circulator is used to separate optical signals that travel in opposite directions in an optical fibre. After passing the optical circulator, the light from the SLD is split into two beams using a 10/90 fibre coupler (FC1310-70-10-APC, Thorlabs) that is based on Michelson interferometry. One beam of ten percent light is delivered to a stationary mirror that refers to the reference arm, while the other beam of ninety percent light is focused on the sample via an objective lens (LSM02, Thorlabs) of 18 mm focal length. For the realization of 2D and 3D scanning, a Galvano mirror (2-axis Galvanometer, GVS002, Thorlabs) is also utilized in the sample arm with precise motor control, where one mirror scans rapidly to form a B-scan (2D), and the other one is responsible for a C-scan (3D).

Then the backscattered beam from the sample arm and the reflected beam from the reference arm recombine in the fibre coupler to form the interference light that is further delivered through the optical circulator into a spectrometer. The spectrometer equips with a collimating lens (F280APC-C, Thorlabs), a diffractive grating (1200 lines/mm), a camera lens (AC-508-100-C, Thorlabs) with a focal length of 100 mm, and a high-speed InGaAs line-scan camera (GL2048L, UTC Aerospace Systems, NJ, USA). A computer with NI (National Instruments Corp., TX, USA) platform works for synchronizing Galvano scanner driving signal and camera trigger signal, as well as real-time imaging processing and data acquisition of the line-scan camera. The program of the data acquisition was implemented in LabVIEW (National Instruments Corp., TX, USA).

Vibration generation

To generate vibration, a sine-wave signal modulated at ~8 kHz is generated by a function waveform generator (33220A, Agilent Technologies, USA) and an amplifier (7724 DC enabled AC power amplifier, AE Techron). The signal is then sent to drive a magnet shaker (LDS V201, Brüel & Kjær Sound & Vibration Measurement A/S, Denmark) as illustrated in Figure 3.1 (b). The vibration is transmitted from the shaker to compress the sample and trigger vibration within the sample in the axial direction. The amplitude of the vibration to the sample is controlled by the voltage output from the amplifier. Table 3.2 shows the gain of the amplifier and the resulting voltage output to the magnet shaker.

Table 3.2 Voltage (V) output to the shaker by adjusting the AF amplifier Gain (%). AF (audio frequency), SD (standard deviation).

Gain%	Test1 (V)	Test2 (V)	Test3 (V)	Mean (V)	SD (V)
10	0.20	0.30	0.30	0.27	0.06
15	0.80	0.80	0.80	0.80	0.00
20	1.30	1.30	1.30	1.30	0.00
25	1.70	1.80	1.80	1.77	0.06
30	2.20	2.30	2.30	2.27	0.06
35	2.80	2.80	2.90	2.83	0.06
40	3.30	3.30	3.40	3.33	0.06
45	3.80	3.90	3.90	3.87	0.06
50	4.40	4.50	4.50	4.47	0.06
55	4.90	5.10	5.10	5.03	0.12
60	5.50	5.70	5.70	5.63	0.12
65	6.20	6.40	6.50	6.37	0.15
70	7.00	7.30	7.30	7.20	0.17
75	8.00	8.20	8.30	8.17	0.15
80	9.00	9.00	9.10	9.03	0.06
85	10.00	10.00	10.10	10.03	0.06
90	11.40	11.20	11.30	11.30	0.10
95	12.30	12.30	12.30	12.30	0.00
100	12.30	12.30	12.30	12.30	0.00

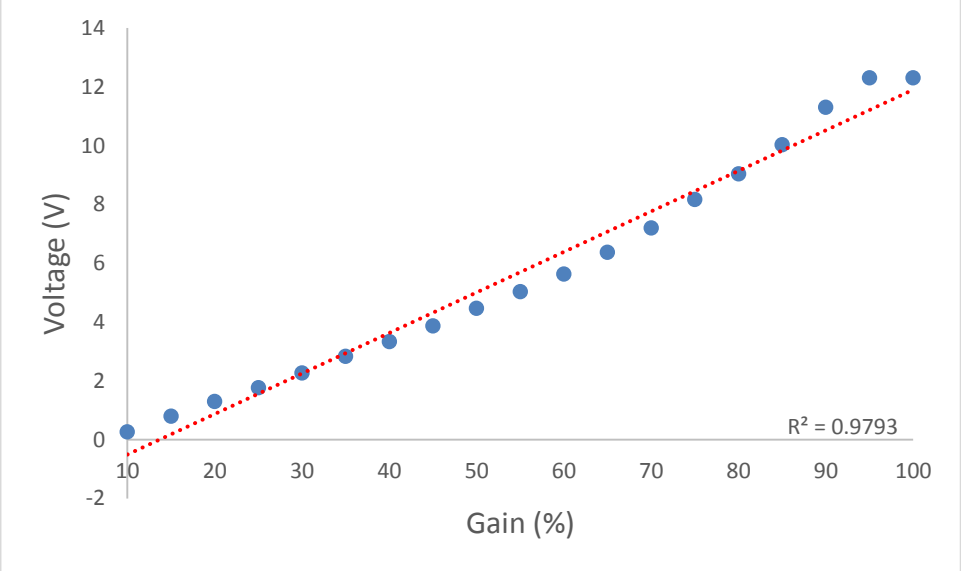

Figure 3.2 A polynomial fitting of the mean value of the voltage output to the shaker and the different Gain (%) of the AF amplifier.

Additionally, the voltage on the shaker is plotted at different gains of the amplifier in Figure 3.2. A linear fitting demonstrated a high R-squared value of 97.93%. The optimum

gain is between 50% and 80% for the biological tissues of biopsy shape. Hence, the maximum displacement applied to the samples is ~1 µm to ensure the generated strain was in pure linear-elastic regime.

Specifications

The parameters of the main components are listed in Table 3.3 For this system performance, it provides an axial resolution of 8.8 µm and a transverse resolution of 7.9 µm in air. The total depth range is measured to be ~2.8 mm in air, while ~2.1 mm in biological tissue by assuming that the refractive index of the sample is ~1.35. Additionally, the dynamic range of the PhS-OCT system is ~100 dB at 0.5 mm axial depth with a phase noise of 3 mrad. However, the signal to noise ratio (SNR) in the region of interest (ROI) of the tissue sample is ~50 dB. The acquisition rate is determined by the spectrometer of a maximum rate of ~76335 A-scans/s.

Table 3.3 Specifications of phase-sensitive OCE system.

Specifications	values
Superluminescent diode (SLD, S5FC1021S, Thorlabs)	
Central wavelength	1302 nm
Bandwidth	85 nm
Axial resolution	8.8 µm
Objective lens (LSM02, Thorlabs)	
Effective focal length	18 mm
Lens working distance	7.5 mm
Lateral resolution	7.9 µm
InGaAs Linescan Camera (GL2048L, UTC Aerospace Systems, NJ, USA)	
Resolution	2048 x 1
Pixel pitch	10 µm
Maximum Line rate	76335 lps (lines per second)
Practical sampling frequency	47 kHz
2-axis Galvanometer (GVS002, Thorlabs)	
Maximum mechanical scan angle	±12.5 ˚
Practical x-axis travel length	3 mm
Practical y-axis travel length	3 mm
A-scans per M-scan	512
Magnet shaker (LDS V201, Brüel & Kjær, Denmark)	
Maximum frequency range	13 kHz

Scanning protocol

The structural images of the samples generated by the PhS-OCT system were shown as a function of depth. While the shaker continued to fire the stimulus to the sample, the vibration signal was acquired using M-B mode as illustrated in Figure 3.3. For the

acquisition of a cross-sectional 2D structural and elastography image, the OCT probe beam stayed for 512 repeats during A-line scan at every spatial location (total 512 locations) sequentially within the B-scan mode. A complete B–scan consists of 512 × 512 A-scans. Accordingly, a cross-section view of the structure was revealed, and further imaging processing in MATLAB R2015b (The MathWorks, Natick, MA, USA) generated an elastogram of the sample.

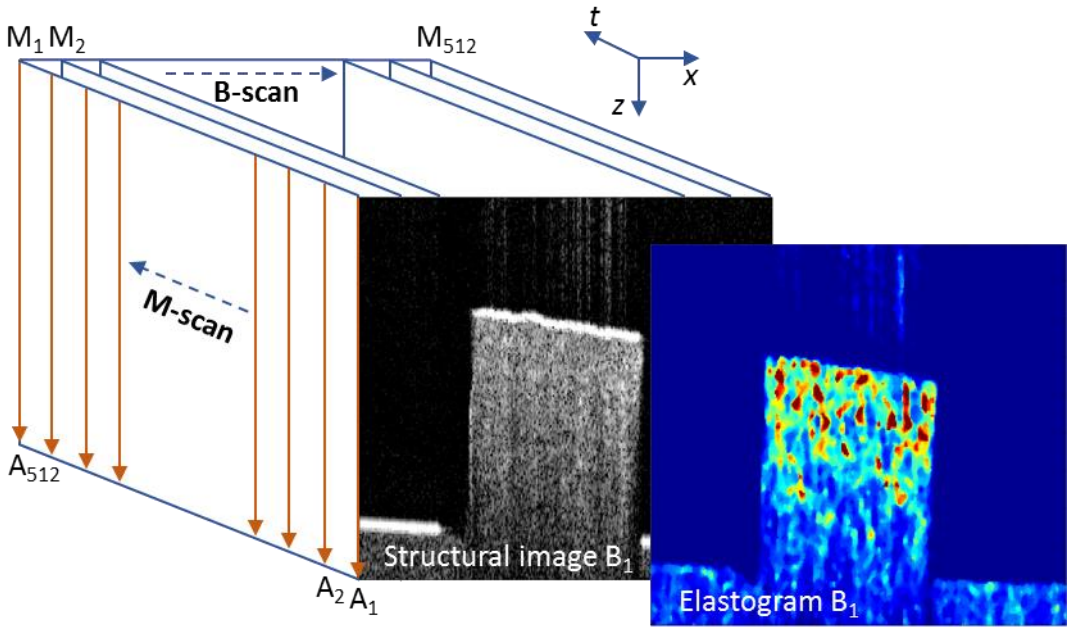

Figure 3.3 A schematic of the scanning protocol using M-B mode for the fixative tissue, wherein the agar phantom as a reference, x-axis is the lateral position of the sample, z-axis is the direction of laser beam, and t-axis represents the time location during M-scan.

3.2.3 Stiffness quantification

Agar phantom

In the vibration OCE, the 2D stiffness of biological tissues was quantified using the agar phantom as a reference. Tissue-mimicking phantoms play an important role in all kind of medical imaging modalities. The physical gels using agar are obtained through physical procedures such as heating and cooling. Agar-based tissue phantoms, while being more cost-efficient, is simple and safe to prepare, and biologically compatible. C. Li et al. [99, 144] studied the elasticity of single-layer phantoms by calculating the phase velocities of surface wave. It was reported that the Young's modulus of 1%, 2% and 3% agar phantoms was approximately 80 ± 2.99 kPa, 193 ± 4.01 kPa, 515 ± 3.59 kPa with a phase velocity of 4.87 ± 0.94 m/s, 7.55 ± 1.09 m/s, 12.33 ± 1.03 m/s respectively. In this thesis, two-percent agar phantom will be used as a quantitative reference.

Fourier transform amplitude

The vibration amplitude within the sample can be measured as phase shift using PhS-OCT. Figure 3.4 (a) illustrates a structural image of the cross-section view of a 2% agar phantom. As shown in Figure 3.4 (b), the phase difference of a lateral position chosen with a red arrow in the structural image is represented as the grey and white strips. Then the vibration signal of a point, chosen with a blue arrow, is denoted as the sinusoid signal in Figure 3.4 (c). After the fast Fourier transform (FFT) of the vibration signal, a peak at ~8 kHz is revealed in Figure 3.4 (d), which is the modulated frequency of the shaker. The FFT amplitude at ~8 kHz is related to the displacement of the point at the lateral position of the red arrow and axial position of the blue arrow.

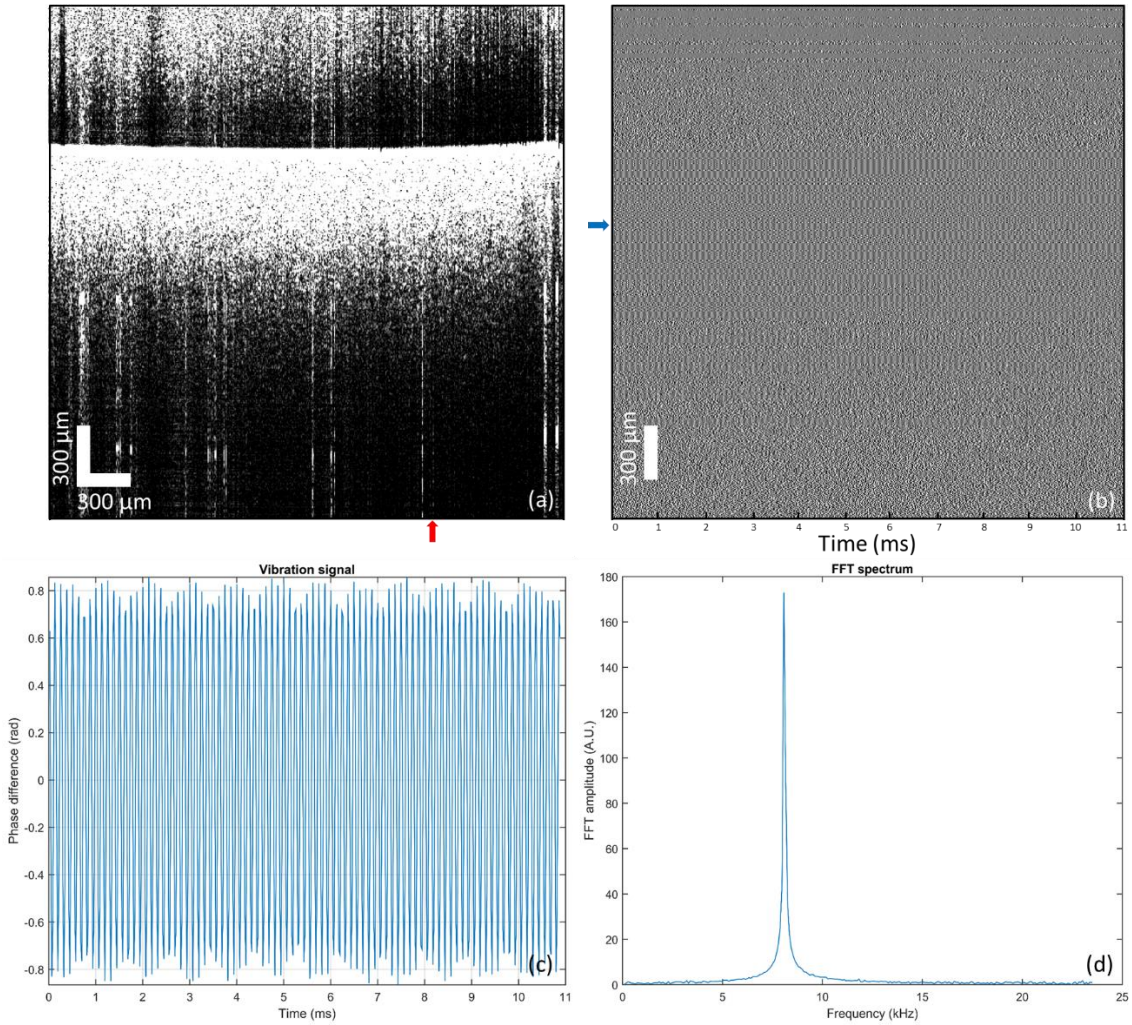

Figure 3.4 Data processing of 2% agar phantom with (a) structural image, (b) phase shifts along time of the lateral position of the structure image labelled with red arrow, (c) the vibration signal along time of a point in the lateral position labelled with blue arrow, and (d) FFT amplitude of the phase difference as a function of frequency.

Theory

The quantitative 2D stiffness of the sample was estimated from the data processing procedure previously described [12, 143]. The vibration amplitude, related to the strain, is highly sensitive to the change of material elasticity. In vibrational OCE, the mechanical field is usually considered as a constant stress field, which means it is assumed that the same force is applied onto an area [113]. By applying stress, σ, on the sample, the relationship between Young's modulus, E, and strain, ε, is expressed as

$$E = \sigma/\varepsilon \tag{5}$$

Under the condition of same mechanical field, the softer material has a larger deformation (strain), whilst the stiffer material has smaller deformation (strain). Hereby, under the same stress ($\sigma_1 \approx \sigma_2$) for a heterogeneous material, the ratio of Young's modulus is written as Eq. (6).

$$\frac{E_1}{E_2} = \frac{\sigma_1/\varepsilon_1}{\sigma_2/\varepsilon_2} = \frac{\sigma_1\varepsilon_2}{\sigma_2\varepsilon_1} \approx \frac{\varepsilon_2}{\varepsilon_1} \tag{6}$$

The strain, ε, is expressed as the displacement, ΔL, over the total length, L, of the sample. In vibration OCE, the strain is calculated using Eq. (7), where, d_1 is the displacement amplitude estimated at a depth of z from the top of the sample and d_2 is the estimation at a depth of $z + \Delta z$.

$$\varepsilon = \frac{\Delta L}{L} = \frac{d_2 - d_1}{\Delta z} \tag{7}$$

Herein, the magnitude of d_1 and d_2 is measured from the FFT spectrum as the absolute value of the FFT amplitude. Using the agar phantom as a reference, different vibration amplitude is generated from the biological tissue and the agar phantom. After subtracting the background noise and averaging all the A-lines, the FFT amplitude is plotted at each points along the depth of a chosen lateral position [12]. Accordingly, the ratio of the strain between the two layers is approximately as the ratio of the slopes between the linear fits of the points in the tissue area and the phantom area.

A heterogeneous material, hereby under the same stress, the ratio of Young's modulus in different regions is equivalent to the inverse ratio of the strain. Thus, the quantitative Young's modulus of the biological tissues, which was placed on the agar phantom, can be estimated. By applying Eq. (7), the ratio of strain is the inverse ratio of the Young's modulus. Previous publications [99, 144] proved that the Young's modulus of 2% agar

phantom is known as ~193 kPa. Given the Young's modulus of the agar phantom, the Young's modulus of the biological tissue can be calculated.

3.3 Results

3.3.1 The effect of formalin fixation to tissue elasticity

It was found that the Young's modulus of all tissue types increased due to the formalin fixation. However, each tissue type varied in time, speed and degree of fixation. Although the elasticity properties of soft tissues (chicken breast, porcine liver and fat) were similar before fixation, the porcine liver had the lowest Young's modulus among them. After embedding them in the formalin for 6 months, the elasticity of the porcine fat was even softer than the porcine liver. The elasticity change of formalin embedded porcine fat, liver, chicken breast, cartilage is presented in Figure 3.5, while the chicken tendon has a much large scale of Young's modulus that is shown in Figure 3.6. Each error bar represents the standard deviation of the three scans of each sample at each time point.

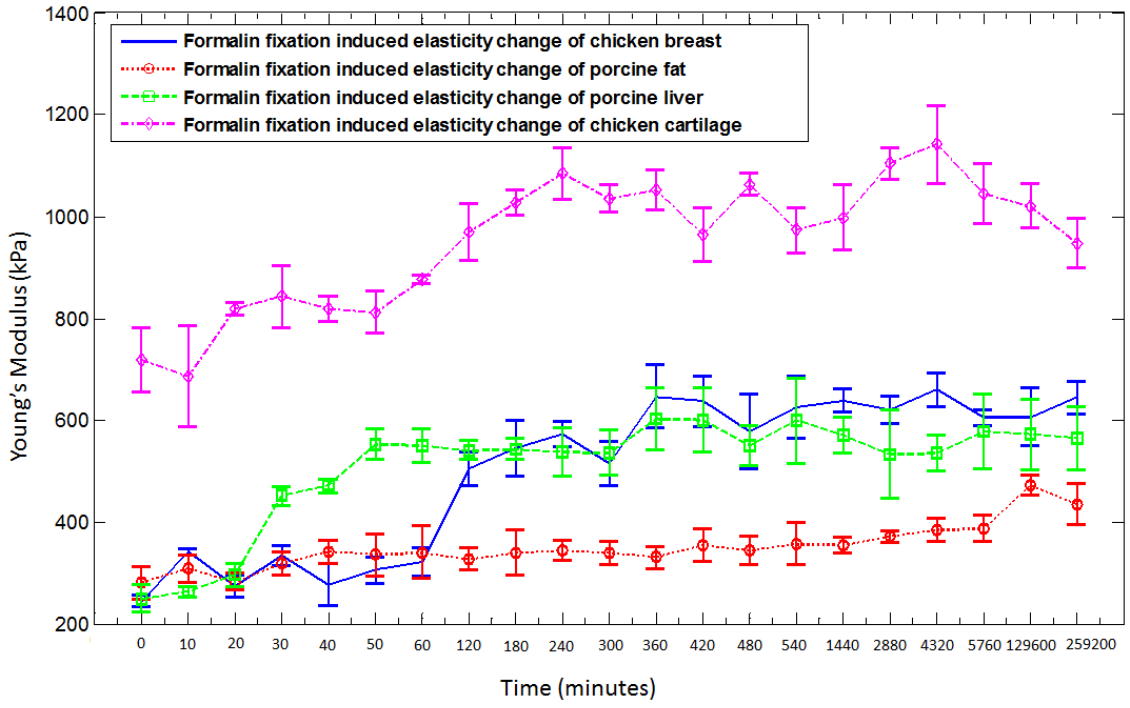

Figure 3.5 Elasticity change of fat, liver, muscle, and cartilage embedded in formalin for 6 months with a precisely controlled time line. Each error bar represents the standard deviation of the three scans of each sample at each time point.

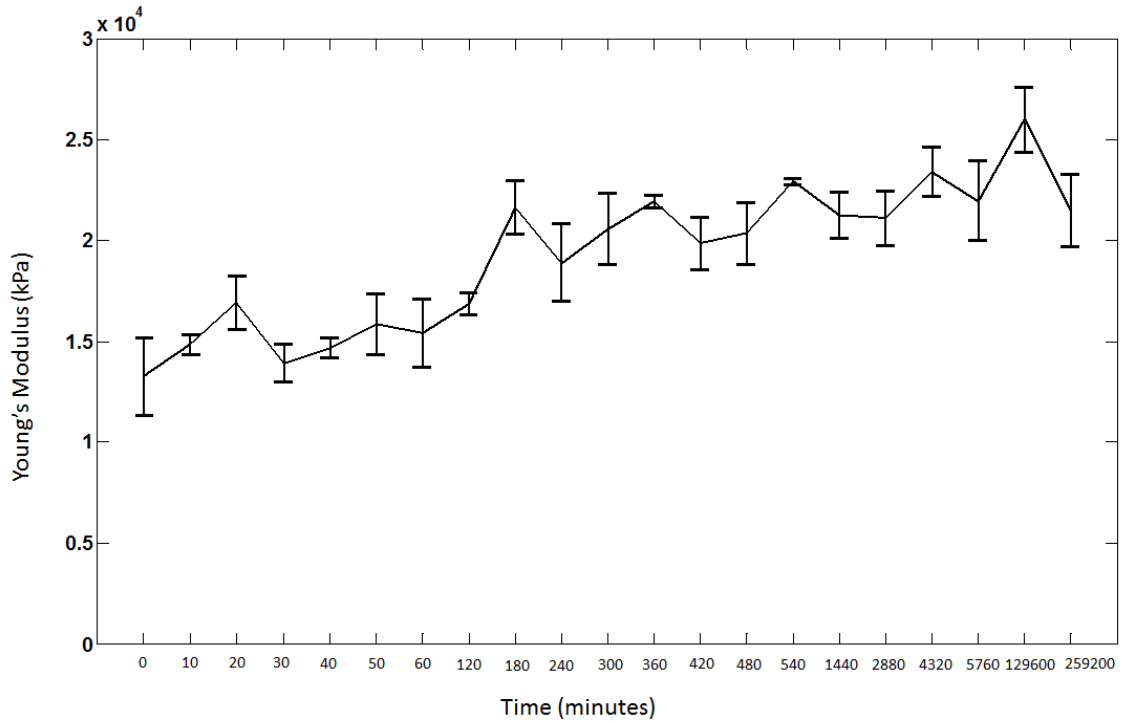

Figure 3.6 Elasticity change of tendon embedded in formalin for 6 months with a precisely controlled time line. Each error bar represents the standard deviation of the three scans at each time point.

Chicken breast

The 2D elastography image with absolute Young's modulus values (Figure 3.7) demonstrates the typical elasticity change of chicken breast which was fixed in 10% formalin dilution. The elasticity data was measured intensively at first 2 hours with a 10-minutes interval, for the following hours, and then 3 days. The overall Young's modulus of specimen can be calculated from the elastograms. The Young's modulus was calculated by averaging Young's modulus value over the whole area associated. In addition, a clear tissue-air-agar boundary can be seen on the elasticity images, although the signal decreases at deeper locations. This is expected because the accuracy of the phase measurement relies on the intensity level from structure image [12].

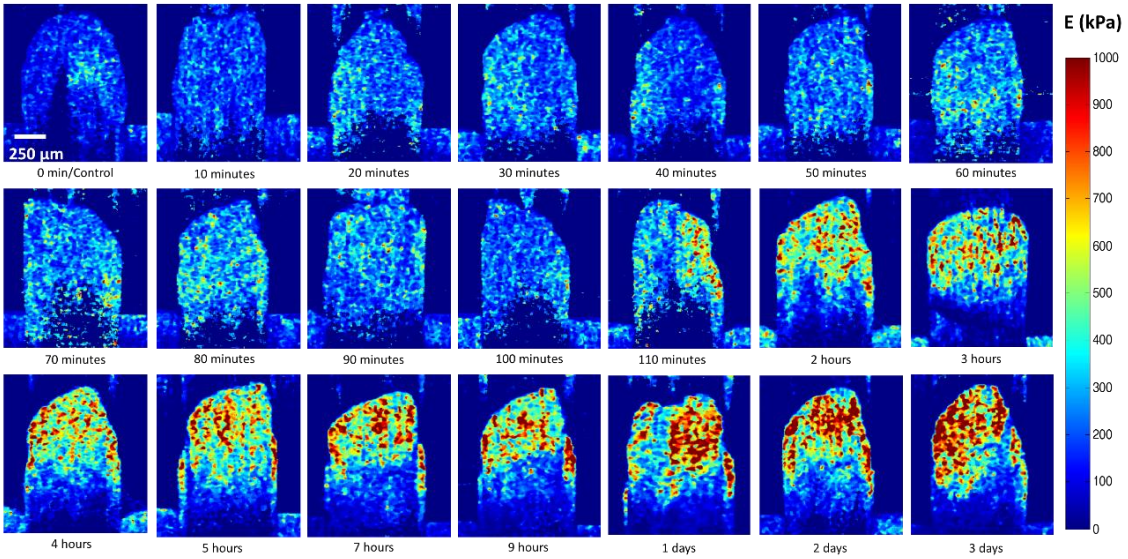

Figure 3.7 Typical elastograms of formalin fixed chicken breast with a precisely controlled time line.

As displayed Figure 3.7, the elastograms were not taken from the identical detecting point on the chicken breast. However, the detection points were close to each other and no larger deviation needed to be considered. It can be clearly observed that the elasticity of formalin fixed chicken breast remained almost constant from the beginning of fixation to 100 minutes. A clear increase of tissue stiffness could be observed from 110 minutes of fixation. The stiffness increases slowly and tends to stabilise after approximately 1 day and remained constant afterwards.

Details of the change of formalin fixed chicken breast can be found in Figure 3.7. The Young's modulus of the chicken breast increases significantly by 106.3% from 110 minutes' fixation (244.7 ± 12.0 kPa) to120 minutes' fixation (504.9 ± 43.4 kPa). The majority increase occurs with the first 120 minutes. After 120 minutes, the Young's modulus of the chicken breast raised slowly with fluctuations and reached approximately 645 kPa at 6 months of fixation. The overall rise of the Young's modulus of the chicken breast induced by formalin was ~164%.

Chicken cartilage

The Young's modulus of the chicken cartilage increased at a slower rate between 60-120 minutes' fixation (from 718.4 ± 63.2 kPa). The cartilage stiffness increased gradually until 4 hours where it reached its stability at ~1100 kPa, with 53.1% overall increase. The elasticity change of formalin fixed chicken cartilage is demonstrated in Figure 3.8 with typical elastograms at 0, 30 minutes, 90 minutes, 3 hours, 9 hours, 1 day, and 3 days.

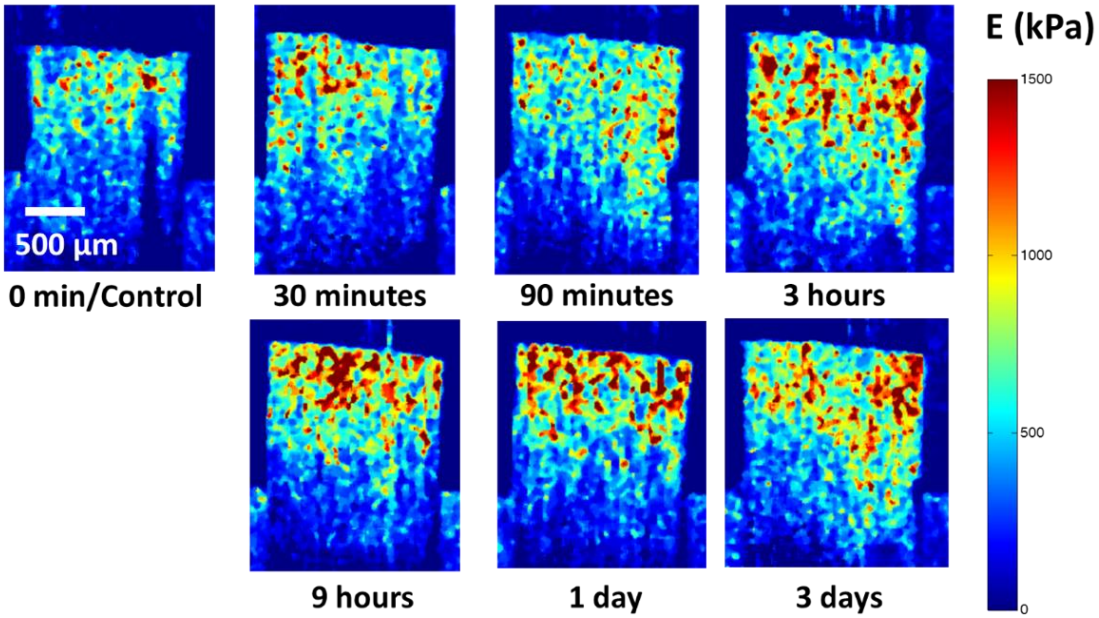

Figure 3.8 Typical elastograms of formalin fixed cartilage with a precisely controlled time line.

Chicken tendon

The Young's modulus of the chicken tendon is much higher compared to other tissue types. The initial value is 13249.4 ± 1908.1 kPa. The increase in elasticity occurred between 120 minutes and 180 minutes and became stable at ~20556.9 ± 1779.3 kPa. The overall increase is 55.2%. The elasticity change of formalin fixed chicken tendon is demonstrated in Figure 3.9 with typical elastograms at 0, 30 minutes, 90 minutes, 3 hours, 9 hours, 1 day, and 3 days.

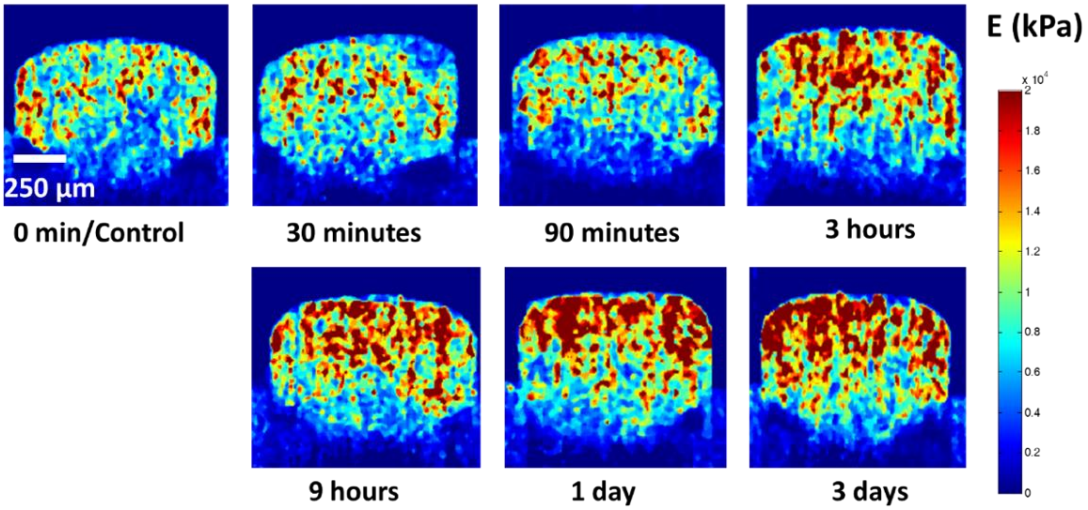

Figure 3.9 Typical elastograms of formalin fixed tendon with a precisely controlled time line.

Porcine liver

The elasticity changes in the porcine liver were observed much earlier and occurred faster compared to all other tissue types. Changes in elasticity occurred within 20-30 minutes (from 249.7 ± 26.3 kPa) of formalin fixation and stabilised in approximately 50 minutes (to ~550 kPa) with overall increase of 120.2%. The elasticity change of formalin fixed porcine liver is demonstrated in Figure 3.10 with typical elastograms at 0, 30 minutes, 90 minutes, 3 hours, 9 hours, 1 day, and 3 days.

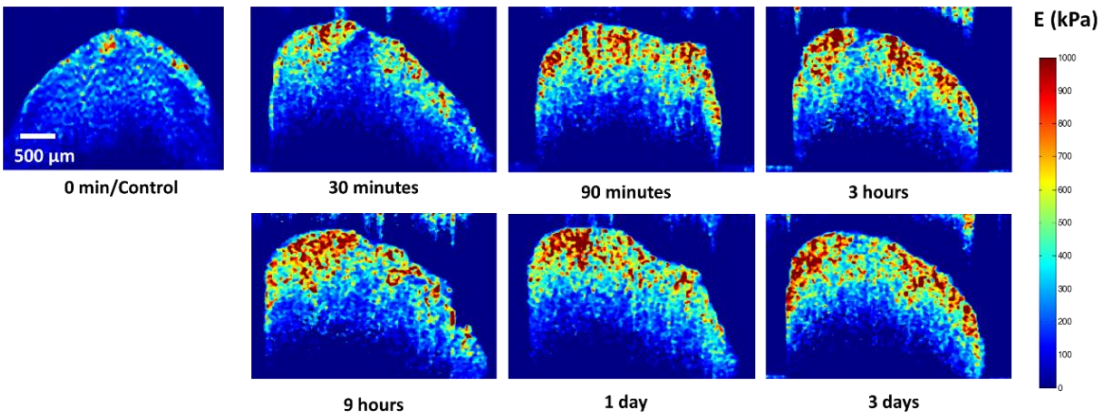

Figure 3.10 Typical elastograms of formalin fixed porcine liver with a precisely controlled time line.

Porcine fat

Formalin had the least effect on the porcine fat, with overall increase by 54.7% from 280.7± 30.8 kPa to 434.2 ± 39.5 kPa. All other tissue types displayed a greater response to formalin fixation. The elasticity change of formalin fixed porcine fat is demonstrated in Figure 3.11 with typical elastograms at 0, 30 minutes, 90 minutes, 3 hours, 9 hours, 1 day, and 3 days. Note that different from other kinds of tissues which were relatively homogeneous in elastograms, the fat tissue is heterogeneous in nature with hollows in the images. It is because that the adipocytes in the porcine fat specimen appear transparent under OCT and only the other cells such as stroma cells can be revealed.

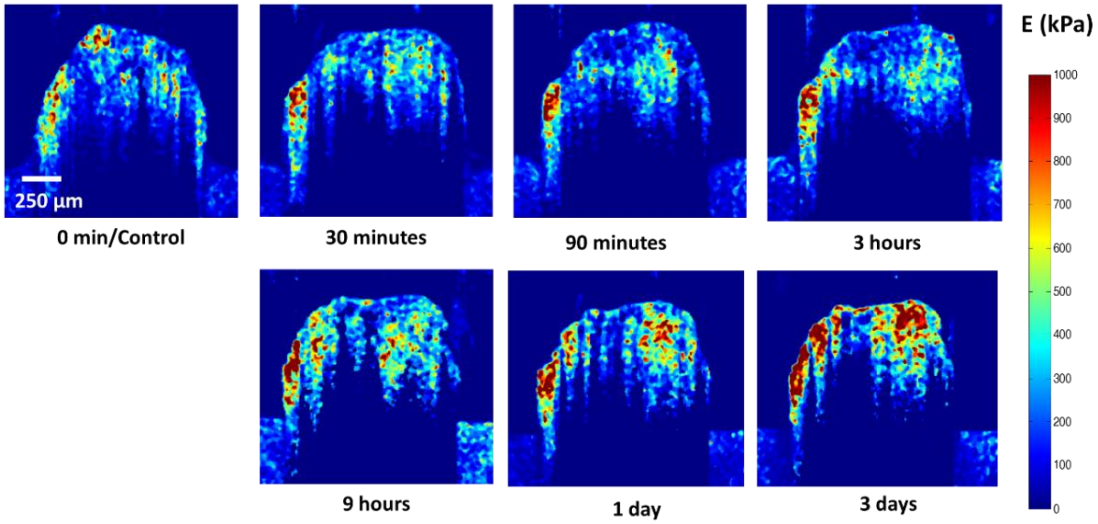

Figure 3.11 Typical elastograms of formalin fixed porcine fat with a precisely controlled time line.

3.3.2 The effect of Thiel fixation to tissue elasticity

Figure 3.12 and Figure 3.13 displays the time impact on the elasticity changes of porcine fat, liver, chicken muscle, cartilage and tendon by Thiel fluid fixation. Each error bar represents the standard deviation of the three scans of each sample at each time point. In the first four days, the Young's modulus of all tissue types embedded in Thiel fluid fixation tend to remain stable with only small fluctuations compared to the formalin fixation. However, the increment of stiffness was observed from 4 days to 6 months in all the tissues. Among them, the porcine fat underwent a large increase of 72.5% from 211.9 ± 43.5 kPa to 365.5 ± 19.4 kPa.

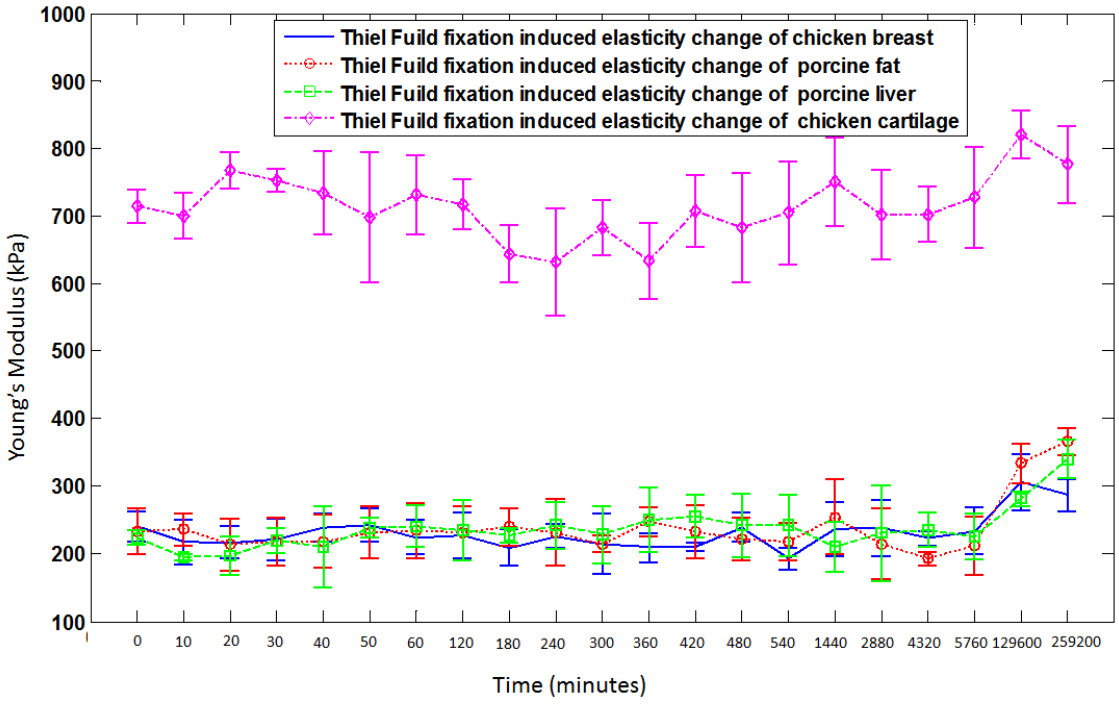

Figure 3.12 Elasticity change of fat, liver, muscle and cartilage embedded in Thiel fluid for 6 months with a precisely controlled time line. Each error bar represents the standard deviation of the three scans of each sample at each time point.

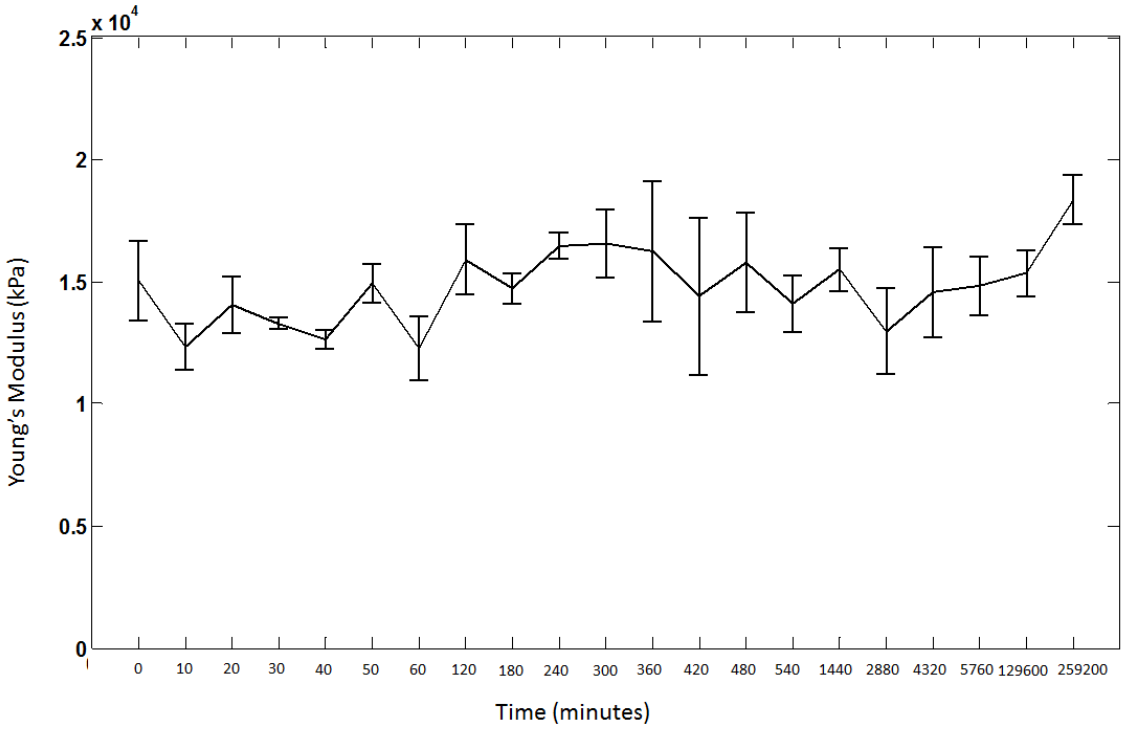

Figure 3.13 Elasticity change of tendon embedded in Thiel fluid for 6 months with a precisely controlled time line. Each error bar represents the standard deviation of the three scans at each time point.

Figure 3.14 shows the elastograms taken from the chicken breast specimens fixed with the Thiel fluid. The chicken breast elasticity does not show any significant increase and remains almost constant from the beginning to the end of 3 days.

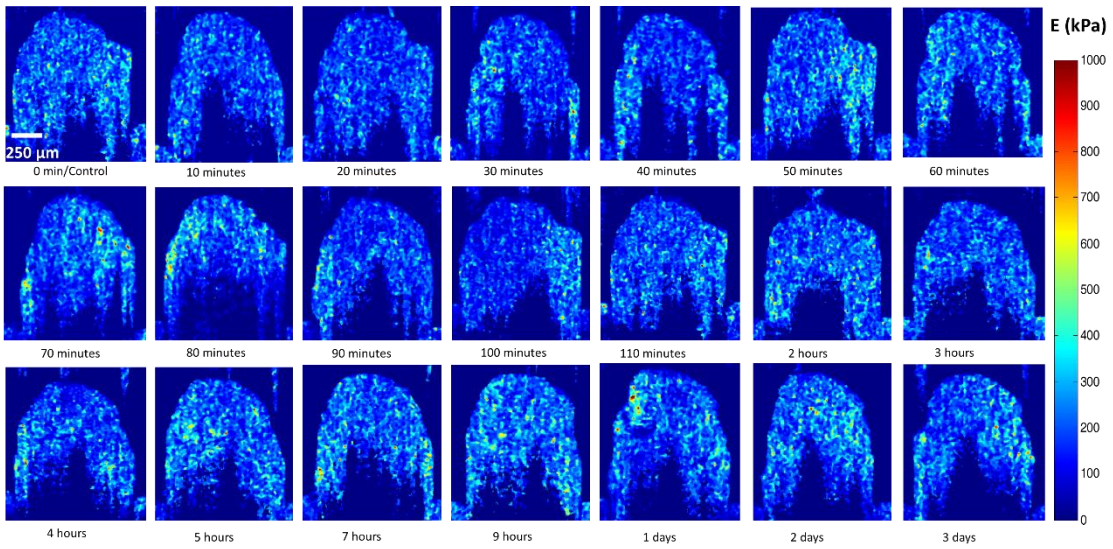

Figure 3.14 Typical elastograms of Thiel fluid fixed chicken breast with a precisely controlled time line.

3.4 Discussion and Conclusion

Normally, the Thiel cadavers are submersed in a tank for at least 3-6 months before use, whilst the Thiel preserving time for smaller organs or tissue samples can be weeks. To replicate the real fixation process, we investigated the elasticity change of the tissues embedded in formalin and Thiel solution for 6 months. As time elapses, the formaldehyde penetrates into the tissue gradually and terminates any ongoing biochemical reactions inside the tissue. The produced cross-links of the proteins result in the augment of the tissue elasticity.

The data gathered displays an ascending trend in the elasticity changes for the samples immersed in 10% formalin dilution, but constant values of Young's modulus with only slight fluctuation for all tissue types immersed in Thiel solutions. This is because that formalin solution has a much higher concentration of formaldehyde than Thiel solutions. After four days, however, the tissues in the Thiel solution tended to become stiffer slightly, whilst no significant increase was observed in formalin samples. Though the measured elasticity of the tissues is an approximate value acquired by comparing with the Young's modulus of the agar phantom, this method is still capable to monitor the change of tissue mechanical properties over time.

Due to the variety of the size and density of different tissue types, the distribution of Young's modulus is not uniform in some of the elasticity images illustrated by the uneven colour. For example, adipose tissue has a heterogeneous structure, where the adipocyte looks transparent in the OCE images. It is also noted that there was little alteration observed in the elasticity of the porcine fat samples fixed with formalin. The primary component of fat tissue is adipocyte, but formaldehyde can change the tissue mechanical properties owing to the cross links of the protein structure. Therefore, less significant tissue stiffness change is produced in fat tissue as compared to other tissues.

Beside of adipocytes, fat tissue also contains stromal vascular fraction of cells such as preadipocytes, fibroblasts and vascular endothelia cells. The elasticity increment mainly comes from the surrounding stroma part, but not the adipocytes. Traditional loading method and sonoelastography can only measure the bulk elasticity of the tissues, and they are limited in the resolution. Although the Young's modulus of fat tissue acquired in this study is the average value of the whole area, more details of the surrounding stroma components can be revealed with OCT structure imaging and elastograms.

Although the tissue was vacuum-packed before transferring to the OCE lab, there had been autolysis and decomposition to a certain extent. In addition, there was evaporation, especially on the surface of the tissue while preparing and scanning the sample. Attributed to the biochemical reactions and manual operation, a slight increase of tissue stiffness at the origin could be possible. When preparing the porcine liver sample, the process of cutting and trimming the sample took considerably longer (5 minutes) as the liver sample was too soft to handle. In comparison, the preparation time for the chicken breast and porcine fat using a biopsy needle took less than one minute. Thought the loss of moisture was minimised and well controlled in the other tissues, the situation could be worse in the liver due to the nature of the tissue compared to other tissue types. Thus, the original value of elasticity of the liver was further increased and higher than literature reports [145, 146].

Theoretically, the tissue samples were ceased from further degradation by utilizing 10% formalin thus it can preserve functional cell and tissue structure, and is beneficial to immunohistochemistry techniques. For the formation of Thiel Fluid, the combination of salts and glycol and reduced formalin can cease any further degradation of samples and provide a softer and flexible fixation than those fixed with formalin solution. However, it is difficult to stain Thiel nerves by standard H&E (Haematoxylin and Eosin stain) histological examination procedure due to the high concentration of salts in the Thiel fluids [147].

In conclusion, this chapter demonstrates that quantitative OCE method is suitable for monitoring elasticity changes during the fixation procedure of 10% formalin and Thiel fluids. It is found that the elasticity changes of tissues in formalin solution display a rising trend, but changes in elasticity of Thiel fixed tissues are not obvious. This is likely as a result of the significantly reduced formalin concentrations in Thiel solutions. Nevertheless, the reduced changes of elasticity in Thiel fixed specimens help to retain lifelike textures and properties of tissues, enabling surgical and clinical training more approaching to the reality compared to traditional rigid formalin fixed specimens. It is proved that a novel technique, vibration OCE, is capable to characterise and assess new fixation methods. Though there is no one fixative suitable for all the situations, it is of great potential using our structural images and elastograms to evaluate the time and concentration of the fixative required to produce specific tissue characteristics in the histopathology.

Chapter 4. Elastic Quantification of Biopsies from Men Suspected with Prostate Cancer Using Vibration Optical Coherence Elastography

The previous chapter has proved the feasibility of using vibration optical coherence elastography in monitoring the elasticity change of tissue with a small scale like biopsy size. Based on the findings from last chapter, this chapter involves a large clinical study, for the first time, to investigate the prostate tissue stiffness using vibration OCE and reveal the relationship between tissue stiffness and the degree of malignancy, as well as the prediction of the final Gleason grade of radical prostatectomy.

4.1 Introduction

Prostate cancer (PCa) is a heterogeneous disease with a multifocal origin [148]. The disease is usually suspected using serum prostate-specific antigen (PSA) test and/or digital rectal examination (DRE). In the routine clinical care, the trans-rectal ultrasound (TRUS) guided biopsies has become the worldwide accepted standard in PCa diagnosis. The degree of malignancy is characterised following histopathologic verification under a microscope using the Gleason scoring system [5] by a pathologist. A healthcare challenge is to improve accuracy of detecting and the Gleason grade characterisation of initial prostate biopsy as this would make more appropriate therapy choices. Radical prostatectomy (RP) is a surgical option for localised disease aiming at cure. However, the data obtained from the histopathological examination of RP specimen indicate that a large disparity exists between the Gleason score of biopsy samples and the RP specimen [3, 4].

RP is primarily meant to remove all malignant tissues while preserving neurovascular bundles and continence mechanism for good quality outcomes [149]. Intraoperatively, the decision for RP is based on a combination of preoperative imaging, biopsy histology and macroscopic assessment. The final decision on margin status, however, is confirmed after many days of surgery which is the least helpful as corrective surgery is impossible in contrast to other organs such as breast cancer [150]. Patients with positive surgical margins have a higher risk of cancer recurrence and need further treatment. An intraoperative diagnostic technique which can reliably assess the margin status of tissues with regard to presence or absence of cancer cells would have a huge potential implication

of surgical techniques and prostate cancer (PCa) patient outcomes. Frozen section and imprint cytology are currently used but are often not reliable [151, 152].

Optical imaging techniques have been explored to address this issue in a number of previous publications. A number of optical imaging techniques have been proposed, including optical coherence tomography (OCT) [153] and Raman spectroscopy [154], however the use of tissue stiffness measurements has not been reported. Tissue from PCa has a higher elasticity modulus than the normal prostate glandular tissue [6]. Changes in the elasticity may indicate an abnormal pathologic process as the elasticity of tissue is a result of increased cell density and collagen deposition [155, 156]. Probing the elastic properties of prostate tissue has become a popular research topic these days [48, 72, 74]. This can also be obtained using optical imaging such as OCT which has a much higher microscale resolution. It has the potential to improve the limit of conventional medical imaging [11]. Furthermore, this technology is promising to uncover the microscopic heterogeneity of prostate tissue and even early tumour.

The use of OCT to perform elastography is a technique known as optical coherence elastography (OCE) with sub-nanometre displacement sensitivity [113]. Although the penetration depth of OCT (1-2 mm) is much less than that of ultrasound and MRI, this limit is overcome by developing fibre optics like needle probes for elastography measurements [157, 158]. Guan *et al*.[12] combined phase sensitive OCE (PhS OCE) with an ultrasound transducer to provide quantitative Young's modulus of a degenerated tendon model with a high spatial resolution. A high signal to noise ratio was reported while monitoring the elasticity alteration of the tendon treated with collagenase of different concentration and time. In the previous chapter, a vibration OCE method incorporating a combination of a spectral-domain OCT (SD-OCT) system and an electromagnetic shaker has been proved to be capable to monitor the fixative effects on the biopsy-size tissue samples. Such results presented the clinical potential of using vibration OCE for the elastic evaluation of prostate tissue.

Building on the technological advance and experience, it is hypothesized that OCE can reliably differentiate benign and malignant prostate tissues with high diagnostic accuracy. Moreover, the technology could have potential in charactering different grades of prostate cancer based on the change of tissue morphology as well as mechanical properties. The vibration OCE will be applied for both 2D and 3D quantitative imaging of *ex vivo* human prostate tissue. Quantitative 3D elastography images of biopsy cores will then correlate with histopathological reports for cross-validation. This technique has the potential to

greatly increase the utility and impact of OCE in a clinical setting, for real-time detection and characterisation of cancers. If combined with OCT needle probe this technique is promising to be used to reduce the number of biopsy required. It is also hypothesis that *ex vivo* measurements of tissue stiffness on biopsy material may have an improved prediction of the final Gleason grade of radical prostatectomy with the patients undergoing laparoscopic RP.

4.2 Patients and Methods

4.2.1 Patients recruitment

Ethical approval was granted by Tayside ethical committee (14/ES/0049). Informed consent was obtained from all the patients before their biopsy procedures for the reported study. We recruited 70 patients (age range 56-85) underwent TRUS guided 12-core biopsy between April 2014 and December 2015, 10 of whom participated in our feasibility study with slight different design of protocol. Afterwards, a small group of 11 patients underwent laparoscopic RP using a rapid prototyping mould based approach published previously [159].

In this chapter, the statistical analysis will only include 60 patients with a well-designed protocol as shown in Figure 4.1. If the participants were suspected with PCa based on elevated PSA and abnormal DRE examination results, 12 biopsies were taken from each participant. Afterwards, OCE scanning was performed on the *ex vivo* biopsy tissues that were submerged in the formalin solution for 24 hours before OCE. Then the specimens were sent for histopathological examination. The final step of this study is to correlate the OCE findings with the histopathological reports as a golden standard.

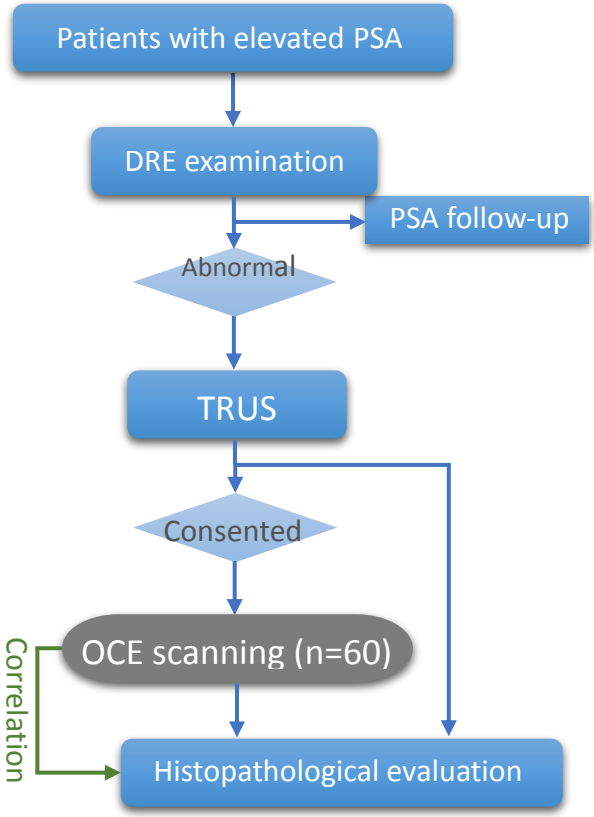

Figure 4.1 Flowchart of patient recruitment.

According to the histopathologic report after the vibration OCE, there are 37 PCa patients, 1 patient with carcinosarcoma, and 22 patients not suspicious of malignancy whose biopsies were classified into the region of benign/normal biopsy tissues. Two combined Gleason scores are usually assigned to the PCa patients to evaluate the aggressiveness and prognosis of the cancer with a higher number to be more malignant. Wherein the lowest score given is Gleason 3+3=6 [20] in the current clinical care. At least one non-cancerous prostate diseases were reported in 17 patients among the 22 cancer-free patients, for instance, benign prostatic hyperplasia (BPH), atypical small acinar proliferation (ASAP), prostatitis and/or prostatic intraepithelial neoplasia (PIN). Table 4.1 displays the details of patient number and percentage for each classification.

Table 4.1 Histopathologic classification of patients suspected with prostate cancer.

Category	Number of patients	Percentage
Prostate adenocarcinoma	37	61.7 %
Carcinosarcoma	1	1.7 %
Non-cancerous disease	17	28.3 %
Disease-free	5	8.3 %
Total	60	100%

4.2.2 Histopathology of biopsies

All participants underwent standard 12-core TRUS guided biopsies of prostate gland. The biopsy size was mainly determined by the geometry of the 18-gauge biopsy needle and the force applied during the operation procedure. Each biopsy was a circular core approximately 0.8-1.2 mm in diameter and 5-20 mm in length. For each participant, the 12 specimens were put into 10% neutral buffered formalin (50 mL) immediately after TRUS procedure and stored in the independent containers. According to the previous study [160] of the effect of fixative on tissue stiffness, the samples were embedded in the formalin for 24 hours before the elasticity test (OCE) was performed on each biopsy.

After the OCE imaging, biopsies were then sent to the pathology department at Ninewells Hospital preparing for the pathological analysis using a routine histological protocol. The haematoxylin and eosin (H&E) staining was applied to exam the cellular structure and report the degree of malignancy. After processing the tissue, the ~5 μm section was mounted between a glass slide and coverslip. At least three histological slices were obtained from each biopsy. Lastly, the staging and percentage of cancer involvement were reported by an experienced pathologist blinded to the OCE data. The detailed histopathology report included the presence/absence of malignancy, grade of cancer, percentage core involvement, and perineural infiltration.

The histopathological data of a total of 720 cores were categorised into non-cancerous prostate tissue (448 core biopsies) and cancerous prostate tissue (272 core biopsies). Among them, there were 260 PCa samples which were further divided into 7 sub-groups as shown in Table 4.2. This sampling size with a varied spectrum should be sufficient for evaluating OCE imaging in the diagnosis of PCa with different aggressiveness.

Table 4.2 Histopathologic classification of biopsies from patients diagnosed with prostate cancer.

Gleason score	3+3	3+4	3+5	4+3	4+4	4+5	5+4	Total
Number of biopsies	58	54	4	46	48	39	11	260
Percentage	22.3%	20.8%	1.5%	17.7%	18.5%	15.0%	4.2%	100%

4.2.3 Imaging system

Details of system setup has been described in the previous chapter. Briefly, the OCE system consists of two main parts: signal detection and vibration stimulation. For signal detection, a phase-sensitive optical coherence tomography (PhS-OCT) with spectral-domain configuration is adapted to measure the displacement of tissues. The PhS-OCT

system employs a superluminescent diode (SLD, Thorlabs) as a broadband light source, with a centre wavelength of ~1302 nm and bandwidth of ~85 nm. For the system performance, it provides an axial resolution of 8.8 µm and a transverse resolution of 7.9 µm in air. Additionally, the dynamic range of the PhS-OCT system is ~100 dB at 0.5-mm axial depth with a phase noise of 3 mrad. However, the signal to noise ratio (SNR) in the region of interest (ROI) of the tissue sample is ~50 dB. The acquisition rate is determined by the spectrometer of a maximum rate of ~76335 A-scans/s. To generate vibration, a sine-wave signal modulated at ~8 kHz is generated by a function waveform generator (Agilent Technologies, USA) and an amplifier (AE Techron). The signal is then sent to drive a magnet shaker (Brüel & Kjær Sound & Vibration Measurement A/S, Denmark). The vibration is transmitted from the shaker to compress the sample and trigger vibration within the sample in the axial direction.

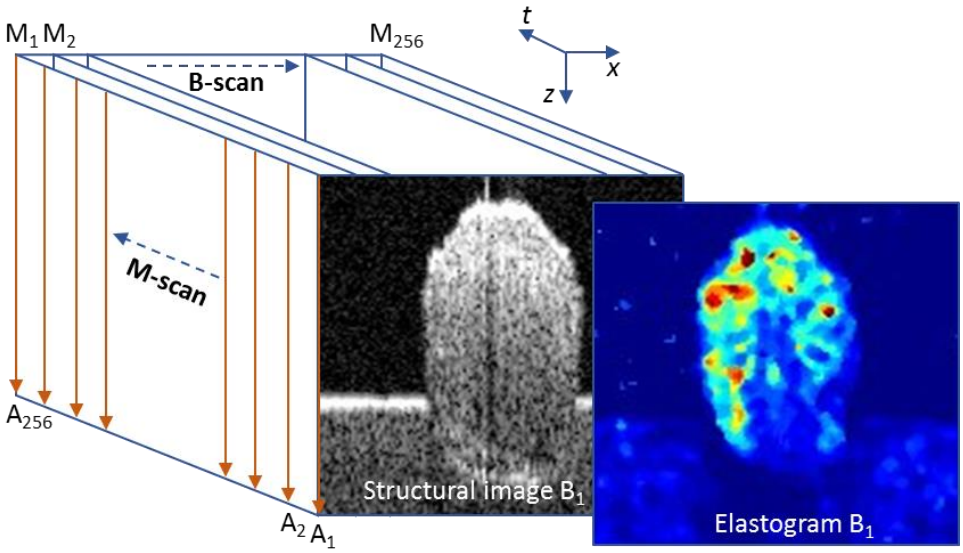

Figure 4.2 A schematic of the scanning protocol using M-B mode for the prostate biopsy tissue, wherein the agar phantom as a reference, x-axis is the lateral position of the sample, z-axis is the direction of laser beam, and t-axis represents the time location during M-scan.

For the scanning protocol of the prostate biopsy tissue, it is slightly different from that of the fixative tissues. As illustrated in Figure 4.2, a complete B-scan (a cross-section view) consists of 256 × 256 A-scans. Three-dimensional (3D) elastogram was then realized with consecutive B scans along the length of the prostate biopsy at an interval of 50 µm. Herein the acquisition time for a set of OCE data was 3 minutes for a size of 2 mm × 2 mm × 3 mm. After the acquisition of one data set, the transitional stage was moved 2.5 mm in y direction for next acquisition, and repeated until the whole biopsy core was scanned. During the OCE scanning, the biopsy core was placed on 2% agar phantom with a

thickness of ~8 mm as an elasticity reference [144]. The total scanning time for each biopsy was dependent on the biopsy length, approximately 20 minutes on average. Finally, the raw structure and elastogram data sets were processed by MATLAB R2015b (The MathWorks, Natick, MA, USA) [12] to generate structural and elastogram frames for each B-scan. The frames were then imported into Amira (Mercury Computer Systems, Berlin, Germany) and reconstructed into 3D data sets at full resolution.

4.2.4 Statistical methods

This research thesis is based on a clinical study that aims at verifying the feasibility of the test imaging method and improving the diagnostic accuracy of PCa. To evaluate the diagnostic test study, the outcome of the test imaging method was compared against the gold standard, i.e. histopathology of TRUS guided biopsy, which is the best single test considered the current preferred method of diagnosing PCa. This is a blind study valid for assessing the diagnostic accuracy of the new imaging method.

It is noted here that the scanning procedure and the subsequent imaging analysis of test imaging was performed on the biopsies from people suspected with PCa before the histopathological assessment without knowing whether or not they have cancer or degree of malignancy. For the histopathological process, the pathologists who interpret the histological slides of the prostate biopsies were blinded to the results of the test imaging method. Since the reference diagnosis (histopathological verification) is open to subjective interpretation, it is crucial to ensure interpreting the results of the reference diagnosis without knowing the results of the test imaging method.

A systematic statistical analysis was conducted after obtaining both OCE and histological results. The Young's modulus (kPa) estimated from 720 biopsy cores by the OCE system was compared amongst malignant and benign tissues, as well as different Gleason scores. All the statistical analysis was conducted in the platform of SPSS 22 (SPSS, Chicago, IL, USA) software. The p value of 0.05 was considered to be statistically significant using analysis of variance (ANOVA) test. Receiver operating characteristic (ROC) curve was utilized to reveal the diagnostic accuracy of OCE technique in differentiating benign and malignant prostate tissues. Differences among different pathological groups were assessed using the Games-Howell test.

The accuracy of the optical imaging method was evaluated by sensitivity and specificity that are independent of the population of interest recruited in the test, while positive

predictive value (PPV) and negative predictive value (NPV) rely on the prevalence of PCa in the population of interest. Herein, the population of interest refers to the sum of true positive (TP), false positive (FP), true negative (TN) and false negative (FN). A table is presented in Table 5.3 to demonstrate the relationship among the abovementioned jargon.

Table 4.3 The relationship among the fundamental terms for a clinical test.

		Gold Standard# Result		
		Positive	Negative	
Test* outcome	Positive	True Positive (TP)	False Positive (FP)	Positive Predictive Value = TP/(TP+FP)
	Negative	False Negative (FN)	True Negative (TN)	Negative Predictive Value = TN/(FN+TN)
		Sensitivity = TP/(TP+FN)	Specificity = TN/(FP+TN)	

Test*: the new diagnostic method, i.e. vibration optical coherence elastography was used to evaluate the malignancy of the prostate biopsies. Gold Standard#: the histopathological result of the TRUS biopsy was applied as the gold standard to confirm PCa.

True positive

True positive (TP) is the case when the test shows positive, as does the gold standard. In other words, the test correctly identifies the patients with PCa.

False positive

False positive (FP) identifies the patients who have PCa but the test outcome is positive. In other words, the test incorrectly detects the patient with PCa.

True negative

True negative (TN) is defined test gives negative, as does the gold standard. In other words, the test correctly classifies the patients as PCa-free.

False negative

False negative (FN) counts the patients who have PCa but the test outcome is negative. In other words, the test incorrectly reports the patient as PCa-free.

Sensitivity

Sensitivity of the test imaging method refers to the ability of the test to correctly identify those patients with PCa, which is the probability of being test positive when PCa present. For example, a test imaging method with 90% sensitivity correctly detects 90% patients with PCa (TP) but 10% patients with PCa are undetected (FN).

$$\text{Sensitivity} = \frac{True\ Positives\ (TP)}{True\ Positives\ (TP) + False\ Negatives (FN)}$$

Specificity

Specificity is the ability of the test imaging method to correctly detect those patients without PCa, which is the probability of being test negative when disease absent. For instance, a test imaging method with 90% specificity correctly detects 90% patients without PCa (TN) but 10% patients without PCa are incorrected identified with PCa (FP).

$$Specificity = \frac{True\ Negatives\ (TN)}{False\ Positives\ (FP) + True\ Neageives\ (TN)}$$

Cut-off value

The cut-off value is set as a threshold above or below which the test imaging method is positive. The sensitivity and specificity of the test are inversely proportional, and dependent on the cut-off value.

Positive predictive value

Positive predictive value (PPV) gives the proportion of patients with a positive test result who truly have PCa. A high PPV suggests that the test imaging method is compatible to the gold standard diagnosis.

$$Positive\ Predictive\ Value\ (PPV) = \frac{True\ Positives\ (TP)}{True\ Positives\ (TP) + False\ Positives\ (FP)}$$

Negative predictive value

Negative predictive value gives the proportion of patients with a negative test result who do not have PCa. Likewise, a high NPV also suggests that the test imaging method is compatible to the gold standard diagnosis.

$$Negative\ Predictive\ Value\ (NPV) = \frac{True\ Negatives\ (TN)}{True\ Negatives\ (TN) + False\ Negatives\ (FN)}$$

4.3 Results

4.3.1 Two-dimensional visualization of prostate biopsies

Cross-section structural, elastogram and overlaid images of biopsies from different pathological categories are demonstrated in Figure 4.3. A benign prostate biopsy was presented in Figure 4.3 (1a, 1b and 1c). A clear biopsy-agar-air boundary is seen in the elasticity images although intensity of the signals decreases at deeper locations. This is expected because the accuracy of the phase measurement relies on the intensity level of structure image.

Figure 4.3 (2a, 2b and 2c) is from a biopsy diagnosed of ASAP. There are subtle differences of structural images between benign and ASAP tissue, which was confirmed by the histologic phenotype. The difference between the two is more obvious in the elastograms, where the ASAP biopsy has lower stiffness than normal prostate biopsy. Prostatic intraepithelial neoplasia (PIN) as illustrated in Figure 4.3 (3) has higher stiffness than benign prostate biopsies, whereas BPH and ASAP have lower stiffness than benign prostate tissue. Notwithstanding, significant overlaps still exists amongst the elasticity range of the abovementioned kinds of prostate tissues.

Figure 4.3 (4-6) compares the structural images and elastograms of malignant PCa with Gleason score of 4+3, 4+4 and 4+5. There are significant differences of elastograms as seen in Figure 4.3 (3b-6b). An increasing trend of Young's modulus of biopsies is observed with the increasing Gleason sum.

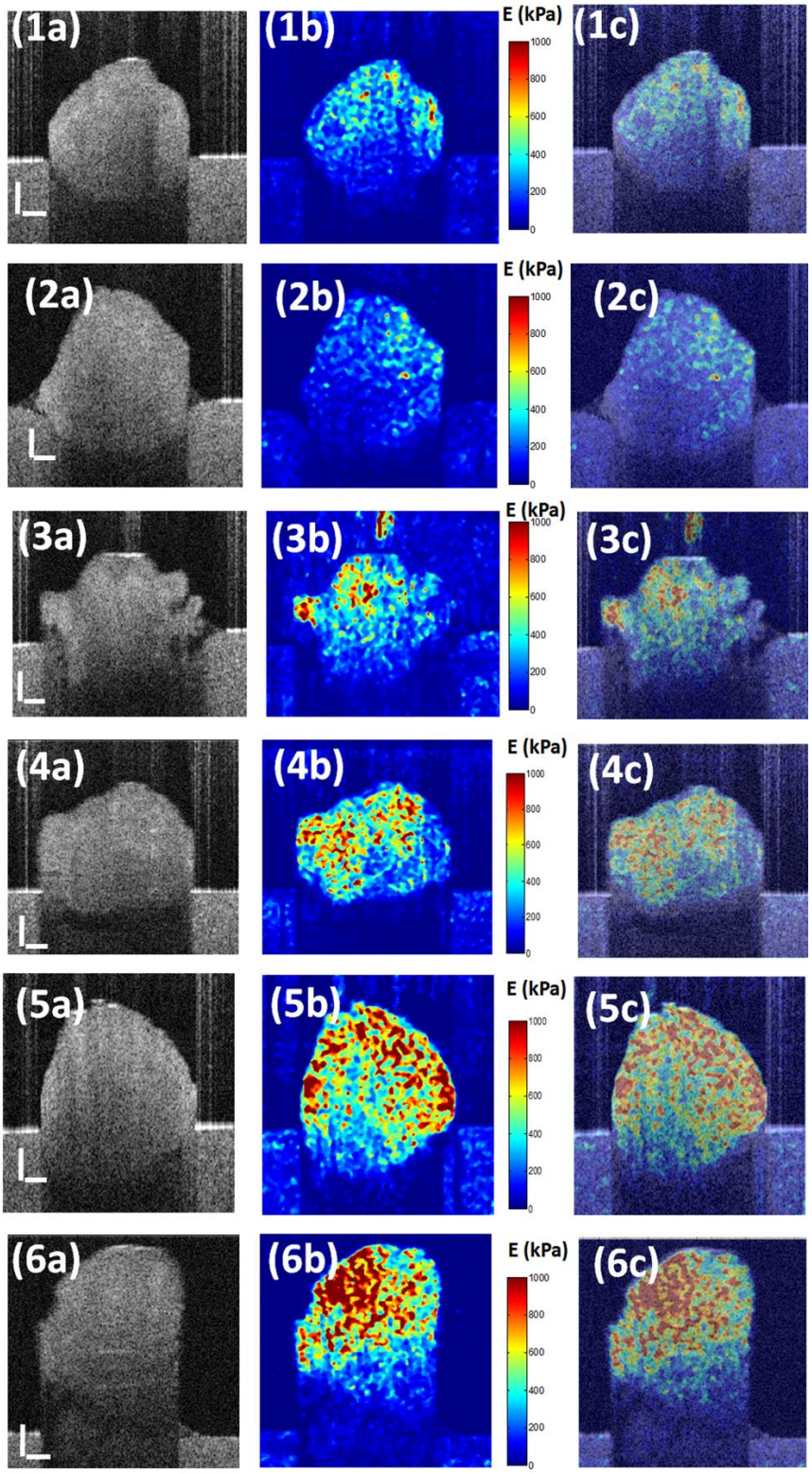

Figure 4.3 (a) Cross sectional structural image (b) the corresponding calculated Young's modulus elastography and (c) overlaid images of structural and elastograms of (1) benign prostate tissue, (2) atypical small acinar proliferation (ASAP), (3) prostatic intraepithelial neoplasia (PIN), (4) malignant prostate cancer with Gleason score of 4+3, (5) prostate cancer with Gleason score of 4+4 and (6) prostate cancer with Gleason score of 4+5. The colour bars show the Young's modulus value in the unit of kPa. The scale is 250μm.

Additionally, the images obtained using OCT and OCE were cross correlated with the images acquired after standard histopathologic processing. The results suggest that micro-architecture in the order of 10 µm can be distinguished in prostatic tissue. Figure 4.4 illustrates cross-sectional OCT structural images and OCE elastograms, as well as and the *en face* histological photos of prostate tissue with different pathological phenotypes. The green arrows pointed the area where the OCT and OCE obtained the 2D images from.

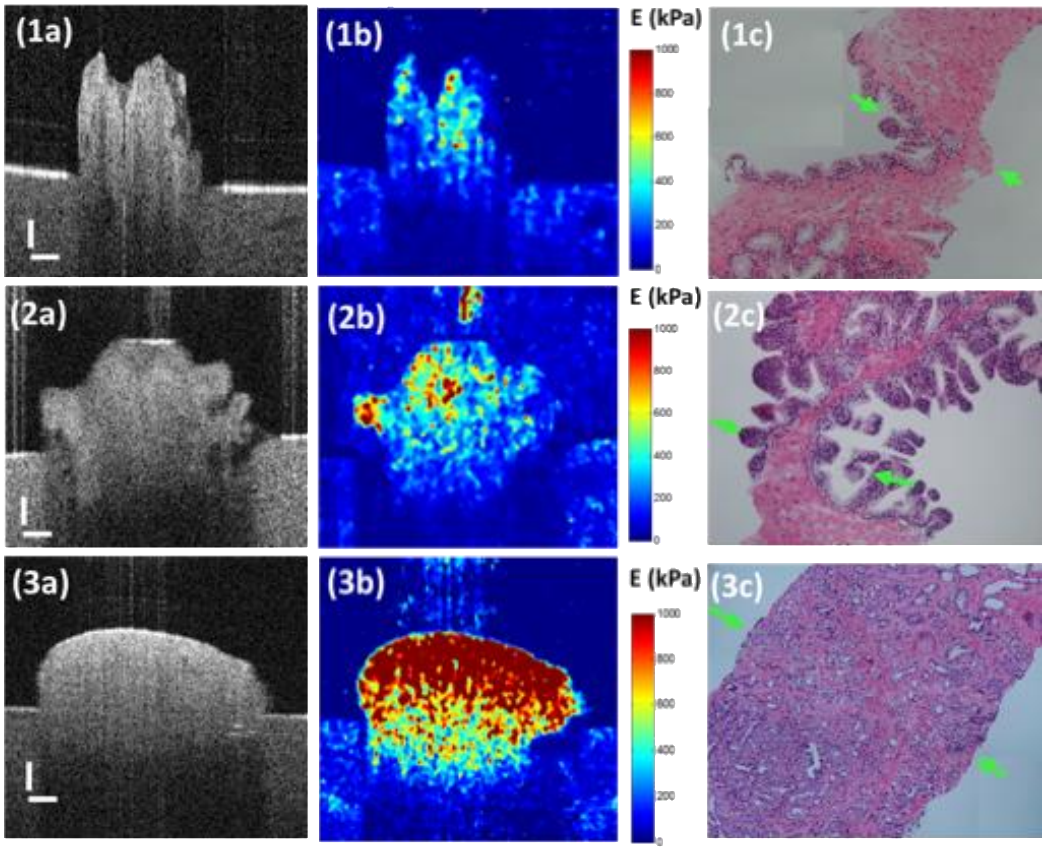

Figure 4.4 Images of (a) cross sectional OCT structure, (b) the corresponding OCE elastograms and (c) *en face* histological images of (1) benign prostate tissue, (2) prostatic intraepithelial neoplasia (PIN) and (3) malignant PCa with Gleason score 4+4. Young's modulus is in the unit of kPa. The scale is 200 µm.

The top of Figure 4.4 presents the images from a benign prostatic biopsy. Figure 4.4 (1a) of OCT structure shows an irregular boundary indicating the benign glandular lumens in the histological image Figure 4.4 (1c). However, difference is not seen between glandular lumens and the surrounding stromal tissue. For example, smooth muscle and fibroblastic stroma cannot be distinguished. Figure 4.4 (1b) demonstrates in detail the elastic variance in single elastogram. The elasticity of glandular lumens is higher than that of the surrounding tissue. By comparing all elastograms and histological photos of benign prostate tissue, it is found that smooth muscle has the lowest stiffness at 378.4 kPa (SD =

48.9 kPa). The glandular lumens have higher stiffness at 530.6 kPa (SD = 30.9 kPa), whereas the stiffness of fibroblastic stroma varies at 518.4 kPa (SD = 82.5 kPa).

Images of the histology, structure and elastogram of PIN are illustrated in the middle of Figure 4.4. The glandular lumen in Figure 4.4 (2a) has a more irregular surface, which is confirmed by the histological phenotype in Figure 4.4 (2c). The difference between PIN and benign prostate tissue is more evident in the elastogram Figure 4.4 (2b).

A typical malignant glandular tissue with a Gleason score of 4+4 is demonstrated in the bottom of Figure 4.4. The lumens here serve as the main characteristics to determine PCa aggressiveness. In Figure 4.4 (3a), the malignant lumen structure is significantly smaller than those in the benign glandular tissue and range in size from 10 to 50 μm, which matches with the histological findings. Therefore, OCT can identify microarchitecture of 10 μm or greater. Cancerous prostate tissue is observed to have a well-rounded shape without irregular gland lumens with higher light reflectivity. A significant increase of tissue stiffness is observed in Figures 4.4 (3b).

4.3.2 Three-dimensional visualization of prostate biopsies

Figure 4.5 delineates 3D images of structure and elastogram from benign and different grade of malignant PCa prostate biopsies. The *en face* views of four different data (structure, elastogram, overlay and histology) are obtained from five prostate cores of benign and different grades of malignant PCa from Gleason sum 6 to 9. Comparing structural images Figure 4.5 (1a-5a) with histological photos Figure 4.5 (1b-5b), a good registration of biopsy structure is observed. In Figure 4.5 (2b-5b), an ascending trend of elasticity is observed in the region of malignant PCa with the increase of Gleason sum. Additionally, the area of malignancy can be better depicted by elastogram obtained from OCE than by histological photo. The bright areas in Figure 4.5 (2b-5b) match with the area labelled by the red arrows in Figure 4.5 (2d-5d), where the red arrows indicate the origin and end of the malignant area in the prostate biopsies. Although the details of biopsy structure is missed in the elastograms, this drawback can be compensated by the overlaid image of both structural and elastogram information as shown in Figure 4.5 (1c-5c).

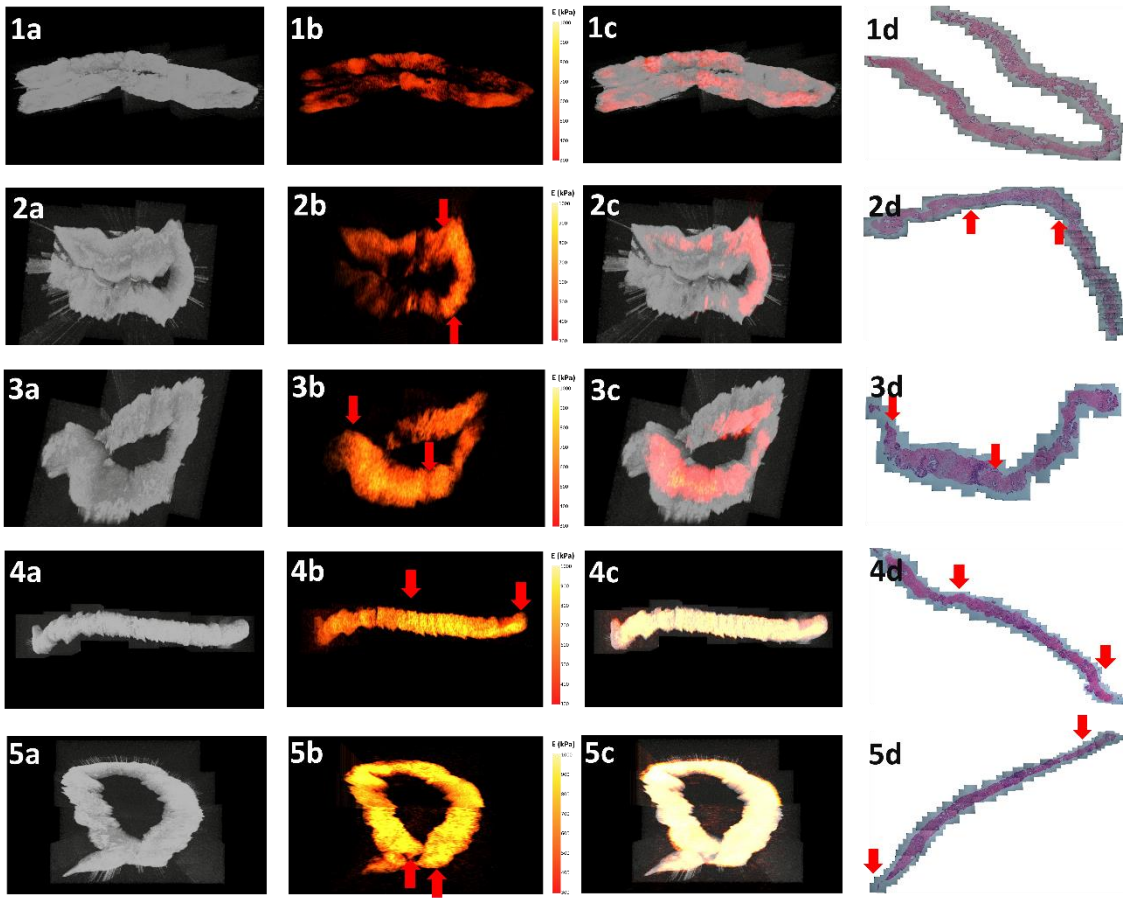

Figure 4.5 3D visualization of (1) benign and PCa biopsies with Gleason score (2) 3+3 with cancer involvement 30%, (3) 3+4 with cancer involvement 40%, (4) 4+4 with cancer involvement 60% and (5) 4+5 with cancer involvement 80%. (a) OCT structural image, (b) OCE elastograms, (c) overlaid images from en-face views and corresponding (d) histological photos. The red arrows in b and d indicate the origin and end of malignancy. Young's modulus is in the unit of kPa. The scale is 200 µm.

4.3.3 Diagnostic accuracy of vibration OCE

In this study, three methods were utilized for the statistical analysis by comparing different biopsy cores: 1) the average Young's modulus method which is the weighted average Young's modulus value over the whole area associated within each biopsy, 2) the maximum Young's modulus which is the maximum Young's modulus value of all the B-scan elastograms across each biopsy, and 3) the threshold method which is percentage of the data points of Young's modulus higher than 600 kPa amongst the whole data set of each biopsy.

Diagnosis of cancer from benign biopsy

The results from the statistical analysis of PCa and benign prostate tissue are illustrated and compared using the whisker plots in Figure 4.6. From these plots, a significant increase of stiffness can be observed ($p < 0.001$) between benign prostate tissue and PCa using any of the abovementioned three methods. With the average method as shown in Figure 4.6 (a), the stiffness of cancer biopsies was approximately 57.63% higher than that of benign ones with corresponding stiffness values of 698.43 ± 125.29 kPa versus 443.07 ± 88.95 kPa. Using Young's modulus of 600 kPa as a cut-off value to suspect PCa, it is noted in Figures 4.6 (c) that some stiff areas exist in the non-PCa biopsies but most of them are below 30%. It could be that the biopsy has very low cancer involvement but not recognized as cancer.

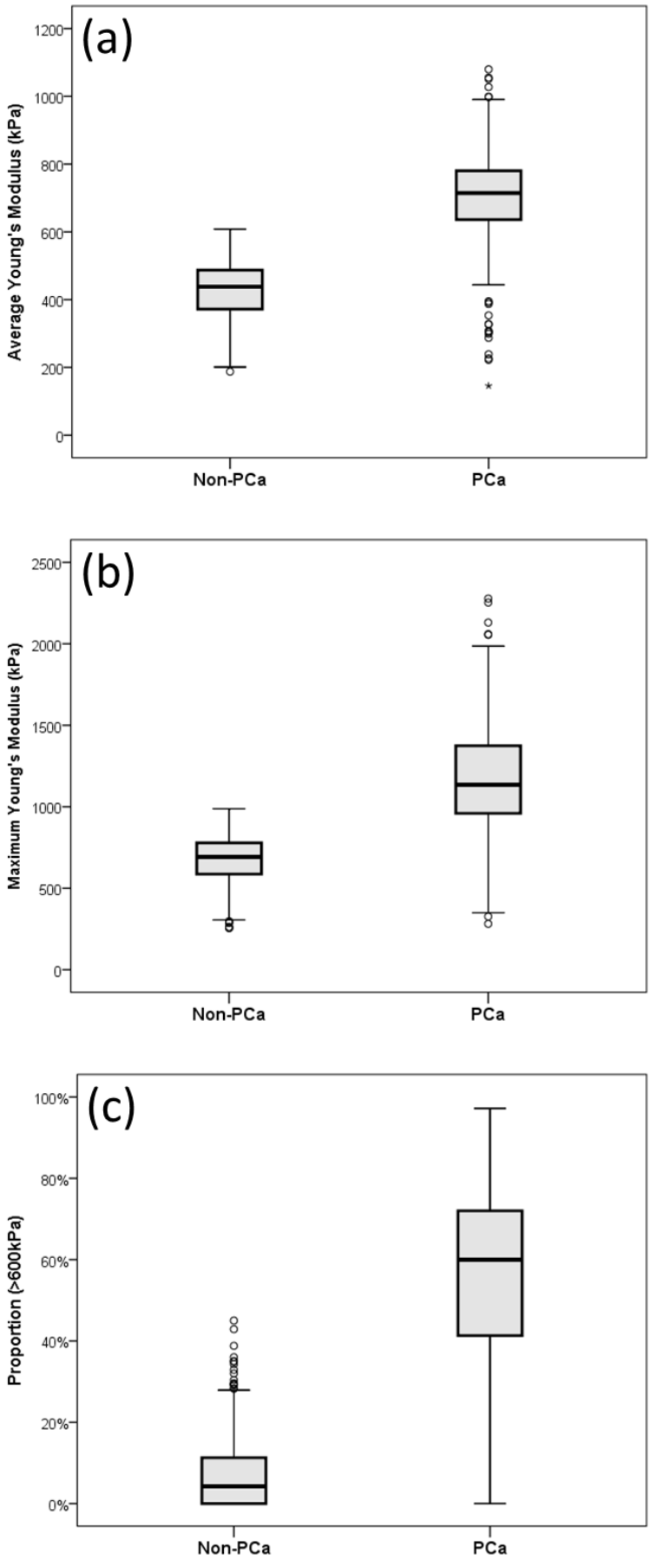

Figure 4.6 Whisker plots of correlation between Young's modulus (kPa) and pathological outcomes using (a) average method, (b) maximum method and (c) threshold method.

Receiver operating characteristic curve

The plot of ROC analysis in Figure 4.7 is intended to evaluate the ability of quantitative OCE to diagnose PCa using the abovementioned three statistical analysis methods. The analysis demonstrates that over 90% area is under the ROC curve. Amongst the three curves, the analysis method using average Young's modulus has the highest area under the curve (AUC) (93.9%) which manifests that OCE is promising with high capability for the diagnosis of PCa. The threshold method has the AUC of 93.6%, and the maximum method has the lowest AUC but still a high accuracy (91.6%). Using the threshold method for the diagnostic accuracy, the biopsies of Young's modulus value higher than 600 kPa are treated as positive results with PCa, and the others are negative and can be considered as cancer-free (benign) biopsies. Compared with the histological results, the data analysis shows that the sensitivity and specificity were 89.6% and 99.8% respectively. Moreover, the positive and negative predictive values calculated for this technique were 99.5% and 94.6% respectively.

Area Under the Curve

Test Result Variable(s)	Area	Std. Error[a]	Asymptotic Sig.[b]	Asymptotic 95% Confidence Interval	
				Lower Bound	Upper Bound
Average	.939	.014	.000	.911	.966
Max	.916	.015	.000	.887	.944
Threshold	.936	.014	.000	.909	.963

The test result variable(s): Threshold has at least one tie between the positive actual state group and the negative actual state group. Statistics may be biased.

a. Under the nonparametric assumption

b. Null hypothesis: true area = 0.5

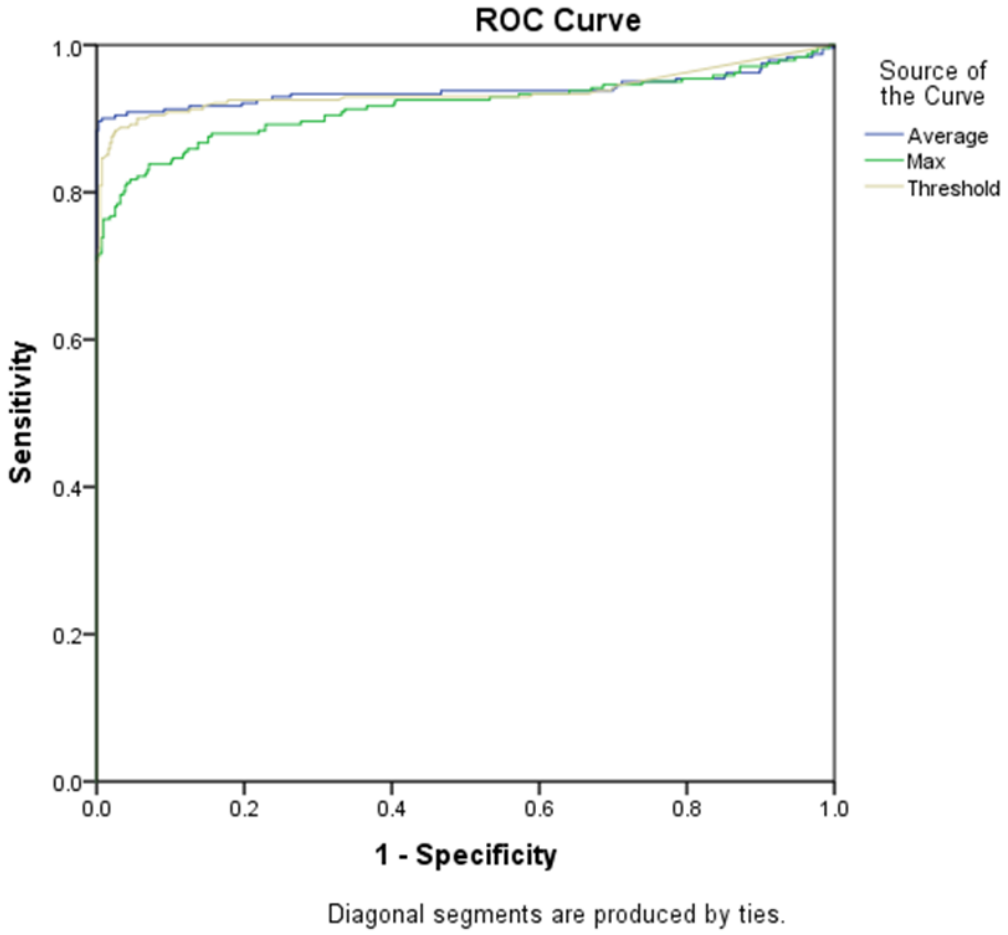

Figure 4.7 ROC curves showing the diagnostic accuracy of vibration OCE in detecting PCa with three statistical analysis methods.

Quantitative evaluation of malignancy

The relationship between the Gleason score and the estimated Young's modulus is compared in Figure 4.8. The presence of Gleason score in the histopathological result is a clinical significance to make the optimal decision for the individual patient. The average method stands out from the abovementioned three methods. A significant difference is

noticed amongst Young's modulus of different Gleason scores estimated by OCE (p value < 0.05) except for Gleason score 7 and 8 (p value = 0.765). The details of the multiple comparison results are listed in Table 4.4 of the biopsy Young's modulus among different pathological categories using three different statistic values.

Table 4.4 Multiple comparison of the biopsy Young's modulus among different pathological categories using three different statistic values.

Multiple Comparisons

Games-Howell

Dependent Variable	(I) sum	(J) sum	Mean Difference (I-J)	Std. Error	Sig.	95% Confidence Interval	
						Lower Bound	Upper Bound
E_average	6	7	-117.69997*	16.00413	.000	-159.6735	-75.7264
		8	-90.41680*	30.48902	.021	-170.5830	-10.2506
		9	-218.89872*	27.32026	.000	-290.6487	-147.1487
	7	6	117.69997*	16.00413	.000	75.7264	159.6735
		8	27.28317	28.03842	.765	-46.9788	101.5451
		9	-101.19875*	24.55544	.001	-166.2304	-36.1671
	8	6	90.41680*	30.48902	.021	10.2506	170.5830
		7	-27.28317	28.03842	.765	-101.5451	46.9788
		9	-128.48192*	35.72699	.003	-221.9542	-35.0096
	9	6	218.89872*	27.32026	.000	147.1487	290.6487
		7	101.19875*	24.55544	.001	36.1671	166.2304
		8	128.48192*	35.72699	.003	35.0096	221.9542
E_max	6	7	-210.94477*	43.87529	.000	-325.5849	-96.3047
		8	-202.87174*	71.68868	.030	-391.0745	-14.6690
		9	-409.32746*	65.71860	.000	-581.7122	-236.9427
	7	6	210.94477*	43.87529	.000	96.3047	325.5849
		8	8.07303	66.67224	.999	-167.8123	183.9584
		9	-198.38269*	60.20677	.008	-357.1107	-39.6547
	8	6	202.87174*	71.68868	.030	14.6690	391.0745
		7	-8.07303	66.67224	.999	-183.9584	167.8123
		9	-206.45572	82.69874	.067	-422.7997	9.8882
	9	6	409.32746*	65.71860	.000	236.9427	581.7122
		7	198.38269*	60.20677	.008	39.6547	357.1107
		8	206.45572	82.69874	.067	-9.8882	422.7997
Thres	6	7	-.21693*	.03266	.000	-.3023	-.1316
		8	-.12838*	.04651	.035	-.2502	-.0066
		9	-.26976*	.04182	.000	-.3792	-.1604
	7	6	.21693*	.03266	.000	.1316	.3023
		8	.08855	.04211	.162	-.0222	.1993
		9	-.05283	.03687	.483	-.1496	.0440
	8	6	.12838*	.04651	.035	.0066	.2502
		7	-.08855	.04211	.162	-.1993	.0222
		9	-.14138*	.04956	.027	-.2711	-.0117
	9	6	.26976*	.04182	.000	.1604	.3792
		7	.05283	.03687	.483	-.0440	.1496
		8	.14138*	.04956	.027	.0117	.2711

*. The mean difference is significant at the 0.05 level.

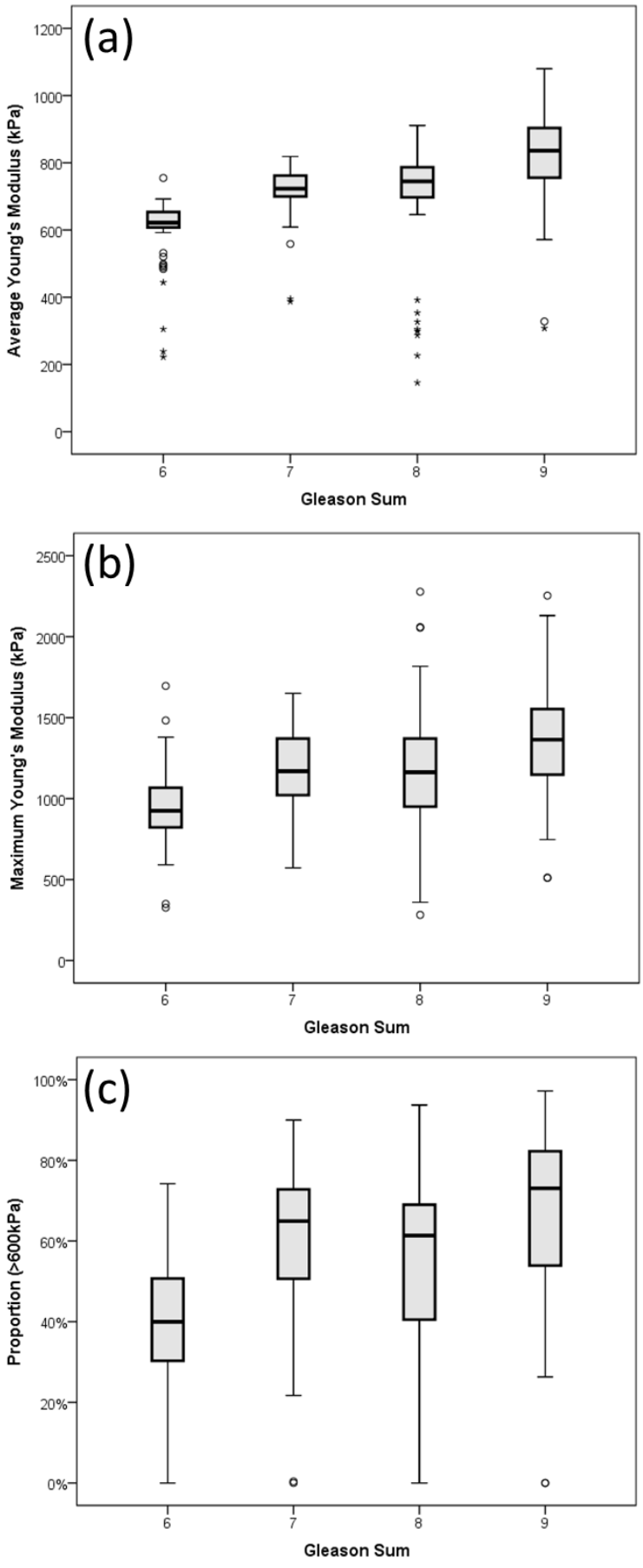

Figure 4.8 Whisker plots of correlation between Gleason scores and Young's modulus (kPa) using (a) average method, (b) maximum method and (c) threshold method.

4.3.4 Prediction of histological grade of radical prostatectomy

Eleven participants underwent laparoscopic RP surgery. Two of them received second biopsy before prostatectomy who are excluded from our study. Three patients (patient no.1, 3 and 7) had upgrading of disease from a low to high Gleason score following RP as listed in Table 4.5. The table summarised the biopsy stiffness, initial Gleason grade, and final Gleason grade of RP. It is noted that biopsy stiffness (kPa) is the weighted mean of the stiffest biopsy amongst 12 biopsies. The ROC curve of the analysis method using average Young's modulus has the highest AUC (93.9%). According to the ANOVA analysis of the average method, the upper bound for Gleason 6 is 626.41 kPa at 95% confidence interval for mean value. Hereby, these three patients should be stratified to a higher Gleason score.

Table 4.5 Disparity between Gleason score of initial and final biopsy.

Patient number	Stiffness (kPa)*	Gleason grade of biopsies	Gleason grade of radical prostatectomy	
1	**631.07**	**3+3**	**3+4**	**7**
2	795.16	3+3 3+4	3+4	7
3	**649.02**	**3+3**	**3+4**	**7**
4	809.61	4+3 4+4 4+5 5+4	4+5	9
5	707.69	3+3 3+4 4+3	3+4	7
6	900.99	3+5 4+4 4+5	4+5	9
7	**658.93**	**3+3**	**3+4**	**7**
8	728.25	3+3 3+4	3+4	7
9	739.24	3+3 4+3	4+3	7

* Stiffness (kPa) is the weighted mean of the stiffest biopsy amongst 12 biopsies.

4.4 Discussion and Conclusion

In this study, we demonstrated an optical characterization of the microstructural details of prostate tissue obtained from a large number of transrectal ultrasound (TRUS) guided biopsies using high-resolution optical coherence elastography (OCE). The method appeared to be highly accurate in differentiating cancer from normal benign prostatic tissue. It also provided accurate characterisation of Gleason grade based on the measurement of Young's modulus (tissue stiffness). Optical coherence tomography (OCT) provides ultrastructural details of the tissues, and elastograms provide additional details and clarity. Additionally, the technique could predict a higher Gleason grade disease on the final histopathology of a radical prostatectomy (RP) specimen. It may help in bridging the disparity between histopathological Gleason grades of TRUS biopsy and RP samples. However, this certainly needs further work due to a small sampling size of only 11 participants. Furthermore, the technique has a real potential of being used during surgery of prostate to guide dissection between peripherally located cancer tissue and neurovascular bundles.

With future engineering and research aimed at *in vivo* stiffness measurement, the instrument can be integrated with optical fibre probes in catheters, endoscopes, laparoscopes, and needles to access tissues deep within the body. The ultimate goals, to be achieved through future research of this work are *in situ* detection and characterisation of PCa to allow a more precise focal treatment, and scan the surface of the excised prostate gland intraoperatively to provide the surgeon with an assessment of tumour margins within minutes of prostate removal. Several challenges must be addressed before a complete translational landscape is possible. Heterogeneity of tissues, including diathermied tissue on the surface of prostate, presence of blood could have an impact on the penetration of light. However, an excised piece of tissue followed by washing using normal saline could be used within surgical theatres for margin status assessment.

As demonstrated in the structural images of prostate biopsies, clear differences were noticed between benign and malignant groups. Benign prostate biopsy tissues were observed to have irregular and hollow glandular lumens in 2D/3D images, whereas malignant ones were lacking a lumenal structure with an increment of light reflectivity. With further use of a different objective lens, the imaging resolution of OCT could be increased to 1-2 µm, which will discover more structural details of prostate biopsy, and enhance the ability of optical biopsy. The functional OCE, used in this study measured vibrational amplitude (surrogate markers of mechanical properties) of the freshly

obtained prostate specimens following mechanical loading of tissues. The tissue stiffness estimated from this parameter was then used to categorise specimens into different histological classifications. Further quantitative 3D elastogram of a prostate biopsy was reconstructed in high resolution from consecutive 2D elastograms. Both structural image and elastogram obtained using the OCE system were compared with histopathology as a reference standard to evaluate the diagnostic accuracy of the technique. A high diagnostic accuracy (with AUC > 90%) of classification of normal and cancerous tissues was presented in an *ex vivo* setting using quantitative OCE. Additionally, point to point comparison between histological image and elastogram illustrated a high accuracy in studying the underlying micro-scale elastic properties. It indicates that OCE can be a promising imaging tool for PCa detection with a high sensitivity and specificity in malignant prostate diseases.

The gold standard histopathological analyse requires the expertise of a trained histopathologist. An inter-observer variation exists between two histopathologists besides difficulties in characterising smaller than 3 mm lesions. Microstructure which may be missed by unaided eyes could explain the cases in this study where few areas of benign tissue has a higher stiffness than most. It was noted that the Young's modulus obtained from this study was higher than literature [71, 72]. The prostate biopsy samples in this study were fixed in formalin before the OCE experiment, which ensures the following histopathological analysis of the cellular structure of the fixed biopsy. Formalin is prevalently used to fix the tissue by cross-linking the proteins and hindering the biological degradation process. It increases the tissue stiffness which, to some extent, can bring bias to the final elasticity of prostate biopsies. In our experiment, timeline was precisely controlled to finish every experiment. Since all the samples were fully fixed in the formalin for 24 hours according to the findings in Chapter 4, the extent of stiffness increase should be the same for all the benign and malignant prostate tissues.

In conclusion, the imaging of the mechanical properties of prostate tissue obtained using OCE presented the potential of optical modality for the identification and characterisation of PCa. The results form a basis for future research using the technique in *in vivo* assessment of PCa and intraoperative assessment of tumour margins. The biopsy stiffness evaluated with high-resolution OCE maybe a new biomechanical marker of PCa with a high diagnostic accuracy of detecting cancer and stratify the Gleason grade of the cancerous tissues.

Chapter 5. Second Harmonic Generation Imaging of Collagen Orientation in Prostate Biopsies from Men Suspected with Prostate Cancer

The quantitative stiffness of prostate biopsy tissue has shown correlation with the cancer aggressiveness in the previous chapter using optical coherence elastography. Nevertheless, the stiffness alteration observed in the prostate biopsy was still in the tissue level. The elasticity of soft tissue is known to depend on the microscopic and macroscopic structural organization of their molecules. Another imaging modality second harmonic generation microscopy is introduced in this chapter to investigate the interaction between prostate cancer cells and the surrounding matrix. This will probably provide a cue for the tissue stiffness increase of cancerous tissue. A brief background about second harmonic generation microscopy will be provided before the adapted methodology, and followed by a cohort of patient study. The results of this study will be correlated with the pathology as a gold standard, including a discussion between stiffness and collagen alignment.

5.1 Introduction

In the microenvironment of prostate gland, there are two main cell types: epithelia and stromal cells [13, 16]. The secretory epithelia in the normal human prostate gland are confined by the basement membrane and the surrounding stroma consists of fibroblasts, smooth muscle cells (SMC), immune cells, nerves, blood vessels and the extracellular matrix (ECM) forming the cytoskeleton. The components in the ECM contribute to the biophysical properties of tissues by providing structural and functional support to the epithelia. Hereby, the prostate ECM is of significance to understand the biomechanics of prostate. The tissue stiffness is a result of increased cellularity and elevated collagen contents in the ECM [155, 156].

Collagen type I and type III are the major structural components [161, 162] in the prostate ECM. Whereas, collagen type IV exists mainly in the basement membrane. Researches have revealed the role of collagen amount in the cancer progression [46, 163]. The network of fibres varies in normal, benign prostatic hyperplasia (BPH) and PCa analysed by scanning electron microscopy (SEM) [164]. Collagen synthesis is elevated in the prostate biopsy material containing cancer by staining collagen type I [15, 163]. Collagen

is highly packed fibres with 3D structure in micrometre scale, while little is known about the correlation between tissue stiffness and fibre alignment within prostate stroma.

Several studies [14, 15, 164, 165] indicate that tumour stroma is different from the stroma in normal tissue. PCa cells proliferate and invade through the basement membrane into the host stroma followed by ECM remodelling and basement membrane degradation. The disruption creates a new stromal microenvironment termed 'reactive stroma' [14, 15, 165] to support cancer cell survival, proliferation and migration, and induce angiogenesis. In breast cancer, remodelling and reorientation of collagen with multiple collagen fibres aligned perpendicular to the tumour boundary may vary with aggressiveness of cancer foci [166, 167]. For instance, straightening of aligned collagen fibres may promote invasion of cancer cell [167]. Therefore, techniques that identify and characterize features of the epithelial-stromal microenvironment are of great diagnostic potential and interest.

Second harmonic generation (SHG) imaging is a popular imaging tool for visualisation and characterisation of non-centrosymmetric 3D structures such as collagen in medicine and biology [168-171]. It can obtain high-contrast images of collagen fibres based on the variations in the ability of the sample to generate second-harmonic light. This imaging method is based on a nonlinear light-matter interaction mechanism where the light emitted from the sample is twice the frequency (half the wavelength) of the incident light. Additionally, SHG microscopy can provide high spatial resolution images noninvasively without bio-markers or ionizing radiation for the cellular and molecular scale of collagen fibres [172, 173].

In the present study, the collagen assembly in prostate tissue was imaged with second harmonic generation (SHG) microscopy. The correlation between histology, prostate cancer (PCa) heterogeneity and SHG imaging will be discussed quantitatively using Fourier transform second harmonic generation (FT-SHG) [174-178]. FT-SHG imaging involves extracting quantitative metrics through the application of spatial Fourier analysis on the images of collagen-based prostate biopsy tissues obtained from SHG microscopy. The difference in stromal collagen fibres has been investigated in normal and malignant prostate biopsies. A parameter (A:I ratio) was applied to compute the regularity in the alignment of collagen fibres and utilized to compare across different Gleason scores. The parameter is a ratio of the anisotropic and isotropic collagen fibres. It was intended to develop a quantitative biomarker to characterize the cancer aggressiveness.

5.2 Second Harmonic Generation Microscopy

In this section, a brief background will be provided for the principle of SHG and describe the typical instrumentation setup, as well as the associated applications.

5.2.1 Theory

Second harmonic generation (SHG) is a second-order nonlinear process in which photons with the same frequency interact with a non-centrosymmetric material, and emission photons are twice the frequency (half the wavelength) of the initial photons [179]. Generally, the nonlinear polarization, P, of the material can be expressed as a power series of the electric field strength, E, of the incident light,

$$P = \chi^{(1)}E^1 + \chi^{(2)}E^2 + \chi^{(3)}E^3 + \cdots$$

where $\chi^{(n)}$ is the *n*th-order nonlinear susceptibility of the material. The first term, $\chi^{(1)}E^1$ is related to the common process such as absorption, reflection, and scattering. The second term, $\chi^{(2)}E^2$, describes second-order nonlinear processes such as SHG, sum and difference frequency generation, and hyper-Rayleigh. Finally, the third term corresponds to the third-order processes such as multiphoton absorption, third harmonic generation (THG) and coherent anti-Strokes Raman scattering.

For SHG, it is noted that the second-order nonlinear polarization depends on the field strength squared, E^2, and the second-order nonlinear susceptibility, $\chi^{(2)}$, which is measured in bulk material. This quantity will not be zero if the material is non-centrosymmetric. In the case of biological tissues, such material can be collagen, microtubules and myosin, wherein collagen gives the strongest SHG signal and thus make collagen to be the focus of most SHG studies. Collagen is the most abundant protein in vertebrates by forming the structure of extracellular matrix (ECM) and providing mechanical support for tissues. Type I collagen contributes to 90% of various types of collagen found in the human body.

Fibrillar collagen has a hierarchical organization. Firstly, the three α-chains forms molecules, tropocollagen of diameter of 1.5-300 nm, which are then self-assembled to be fibrils of diameter of ~20-250 nm, and finally to fibres of diameter of ~0.5-3 μm [168, 180]. The fibril-forming collagens are stabilized by intermolecular covalent cross-links that contribute to the overall tensile strength of most collagen based tissues. The allocation of collagen fibrils varies with the type of tissue, for instance, collagen fibrils

of tendon align parallel to each other to form banded and crimped bundled structure, while those of skin are more random with a complex interlaced network. The organization and distribution of fibrillar collagen is of significance for the tissue mechanical properties, and may play a key role in the progression of disease and cancer.

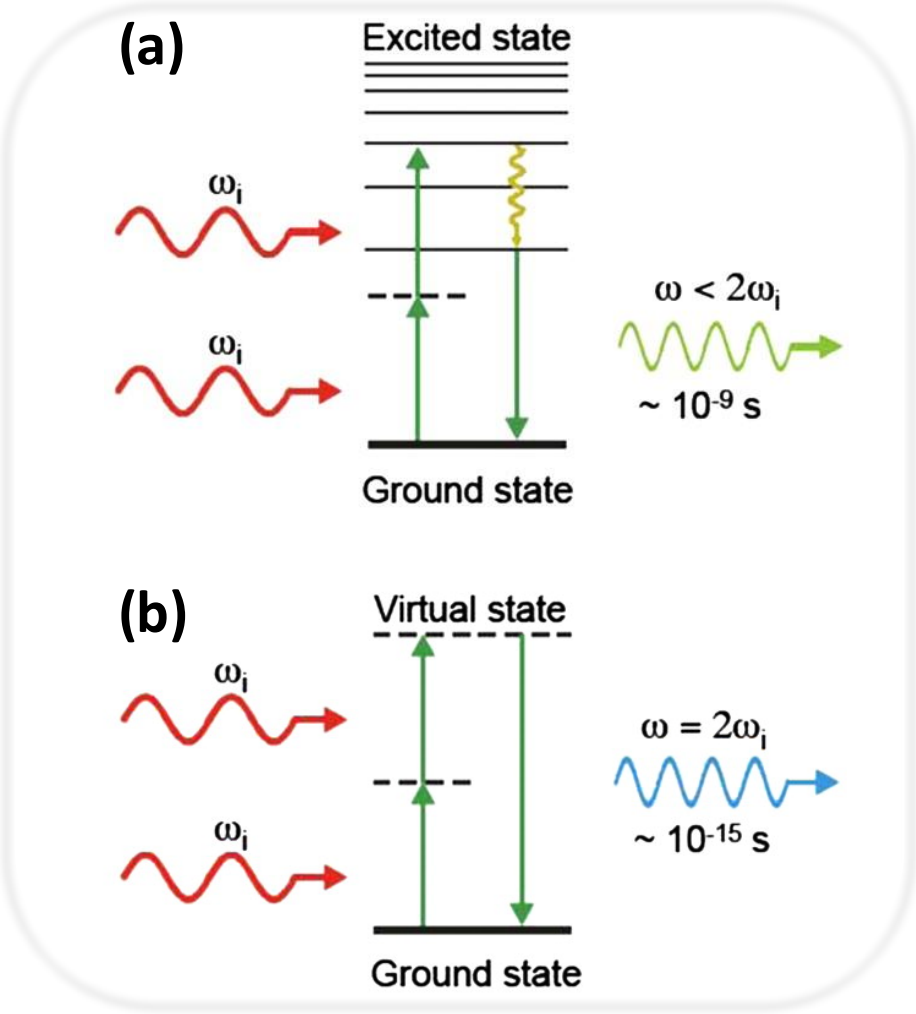

Figure 5.1 Jablonski diagram of (a) two-photon fluorescence, and (b) second harmonic generation. Adapted from Pantazis et al. 2010 [179].

Given a material without inversion symmetry and the incident beam with frequency, ω_i, as demonstrated in Figure 5.1, the vibrating electric field of the incident light causes the polarization of the medium. The emission light contains both the one with original frequency, ω_i, and the one with frequency, $2\omega_i$. As shown in Figure 5.1 (a), two-photon fluorescence involves real energy transition due to the transition from electronic ground state to excited state, resulting in the emission of a lower energy fluorescence photon and potential photodamage of the fluorophore. During the process of SHG as presented in Figure 5.1 (b), energy is conserved, i.e. all of the incident radiation energy at frequency, ω_i, is converted to emission radiation at the frequency, $2\omega_i$. Additionally, the response

time of SHG (femtosecond) is much faster than that of fluorescence (nanosecond), which allows SHG to achieve very quick and sensitive detection.

5.2.2 Instrumentation

Most SHG microscopes described in the literature are basically two-photon fluorescence microscopes, in which the optical path, detection geometry, and detection electronics are modified to include both the transmission and reflection detection geometries. In this way, both forward and backward signal collection are enabled in a complete SHG microscope. Due to the momentum conservation, the emitted SHG signal is predominantly in the forward direction. The backward SHG signal can be generated when the axial scatters are spaced by half wave, λ_{SHG}, and through multiple scattering of the forward signal as shown in Figure 5.2.

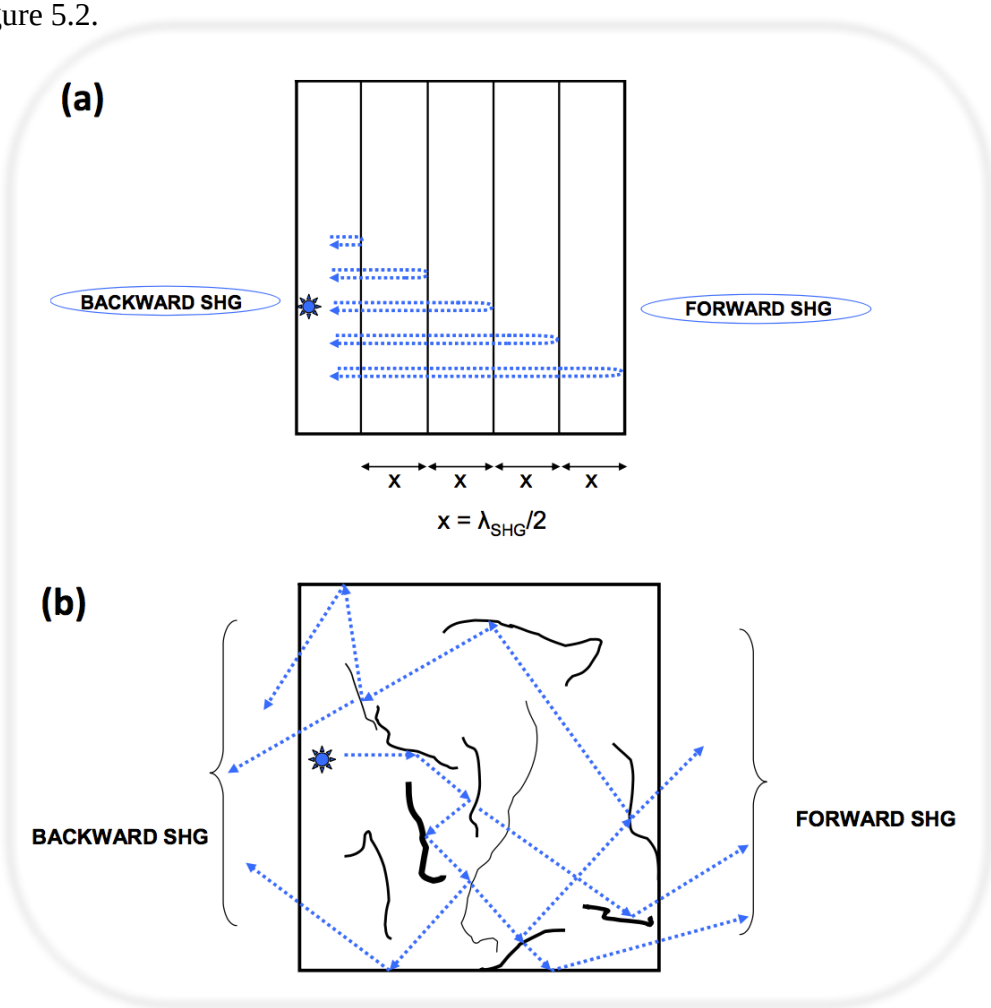

Figure 5.2 SHG signal generation of a) directional emission from constructive interference of scatters spaced $\lambda_{SHG}/2$, and non-directional emission from multiple scattering of forward signal. Adapted from Ambekar et al. 2012 [180].

The schematic of a typical SHG microscope [180] is illustrated in Figure 5.3. Modern SHG instrumentation contains two major components that are commonly a laser scanning

microscope, and a mode-locked femtosecond laser such as a wavelength tuneable titanium sapphire (Ti:Sap) laser. Herein, the selection of wavelength is determined by the type of biological tissue under investigation.

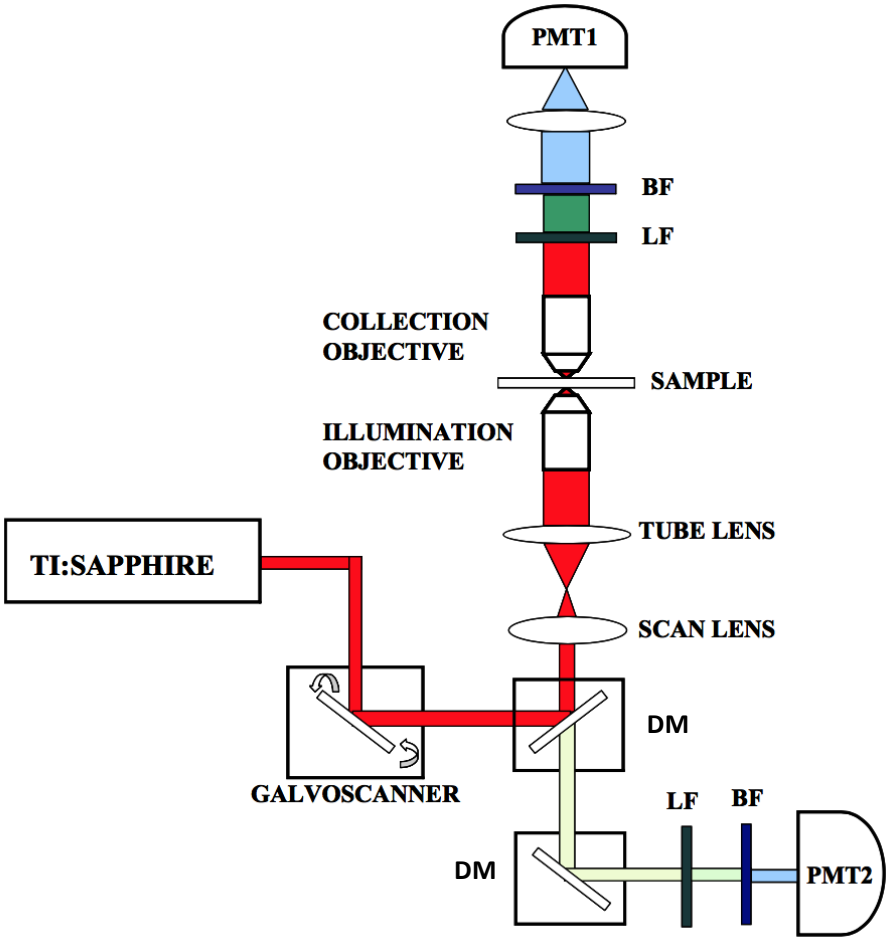

Figure 5.3 A schematic of the experimental setup of the SHG microscopy. LF is laser blocking filter, BF is SHG band pass filter, DM is the short-pass dichroic mirror, and PMT is photomultiplier to record the SHG intensity. Adapted from Campagnola et al. 2011 [168].

The beam is spatially filtered and collimated before travelling to the galvanometer that is a raster scanner. Then it is reflected by a short-pass dichroic mirror. Finally, the beam is focused onto the specimen after passing through scan and tube lens. Both a half wave and quarter wave plate are used to precisely control the polarization of the laser at the focal point of the microscope [168]. The working process of SHG signal detection is detailed below for both the forward and backward.

(1) For the detection of forward signal, the transmitted signal from the specimen is collected by a second objective. A high-NA (numerical aperture) condenser or objective is preferable for efficient SHG collection. The signal is then collected via spectral filtering

using a laser blocking filter and a band pass filter that transmits only the SHG signal. Finally, the SHG intensity is recorded with a photomultiplier (PMT1) tube.

(2) For the detection of backward signal, the epi-illumination path is required. The signal is first isolated using a dichroic beam splitter, then travels via a bandpass filter, and finally detected with a PMT2 tube.

5.2.3 Applications

SHG microscopy is well-suited for collagen imaging *in situ* owing to the intrinsic advantages over other imaging methods.

(1) The visualization of tissue structure relies on the endogenous contrast rather than using exogenous dyes or coloured proteins.

(2) SHG signals are collected based on polarization instead of absorption, unlike fluorescence imaging. Hereby, the potential photobleaching and phototoxicity, is substantially reduced.

(3) Additionally, due to the long wavelength (800-1000 nm) of the near-infrared laser utilized for light source, SHG microscopy can realize high spatial resolution (200 nm-1μm) to depths of several hundreds of microns (100-300 μm) [168, 180].

Since the last decade, SHG has emerged as a powerful nonlinear optical imaging for both biological and clinical applications. SHG imaging was utilized to study the polarity of collagen fibres in rat tail tendon in 1986 [181], which laid the foundation for the development of modern versions of SHG instruments. Increasing attention has been paid to the collagen fibres in cornea [182], skin [183], artery [184], tendon [173], lung [185], liver [186], and breast [166, 167, 176]. Among them, many studies have focused on the role of collagen in the tumorigenesis and metastasis of breast as the collagen density is found to be related to the mammographic density. Moreover, breast is the most closet tissue to prostate due to the remarkable underlying biological similarities.

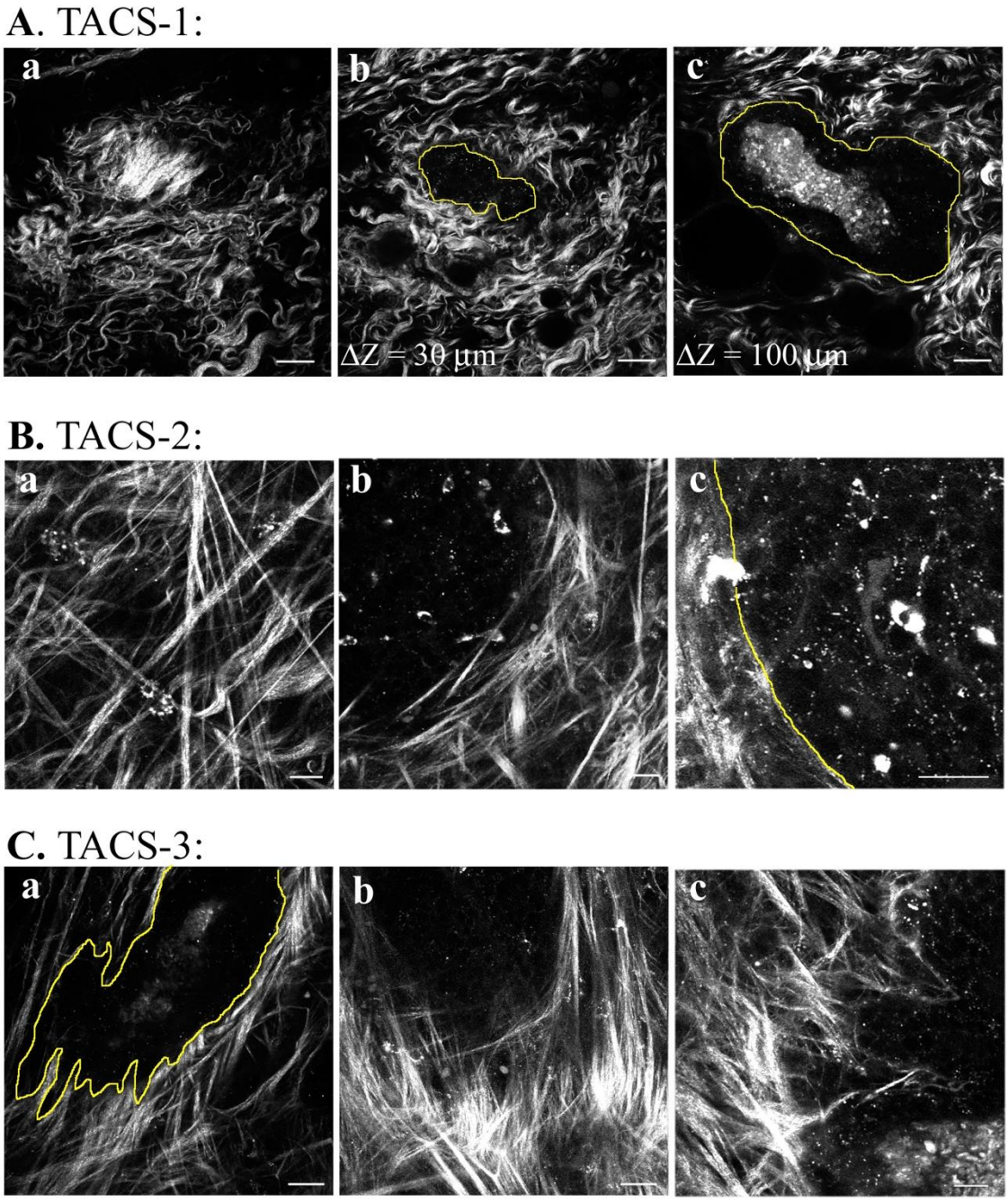

Figure 5.4 Representative SHG images of changes in collagen fibres alignment in breast cancer for three identifiable stages (TACS). Scale bar is 25 μm. Adapted from Provenzano et al. 2006 [167].

Provenzano et al. [167] measured arrangement of collagen fibres in murine tumour models using both SHG and multiphoton excitation to investigate the relationship between the collagen organization and breast cancer progression. Three tumour-associated collagen signatures (TACS) were characterized during defined levels of tumour progression as demonstrated in Figure 5.4 A, B and C.

A. TACS-1 pattern describes that the presence of increased dense collagen surrounding the tumour (marked with yellow line in b and c) was served as a reliable hallmark for locating a small tumour, but no specific alignment was present. The images a, b, and c are images from different depth.

B. TACS-2 pattern indicates that the collagen fibres stretched around a relatively smooth tumour boundary (marked with yellow line in c) when the size of the tumour increased, and were observed aligned parallel to the tumour boundary.

C. TACS-3 pattern presents that the aligned collagen fibres were normal to the irregular tumour boundary (marked with yellow line in a) associated with local invasion. It was also observed that the collagen aligned in the direction of cell invasion.

Five years after this murine model study, Conklin et al. [166] conducted a cohort of human study. It was reported that the TACS-3 pattern was highly correlated to the patient survival. Additionally, Ambekar et al. [176] employed Fourier transform SHG (FT-SHG) to quantify the fibre organisation by calculating the number of areas with aligned or randomly oriented collagen fibres, and this method was capable to identify cancer tissue from other breast benign diseases. Although the SHG microscopy has gained substantial achievement in breast cancer, it has not been performed in PCa for the quantification of the fibre alignment. The investigation of collagen alignment in prostate cancer using SHG microscopy is a potential method to better understand the mechanical behaviour of PCa tissue, and the relationship to disease progression.

5.3 Biopsies and Methods

5.3.1 Human prostate biopsy

Ethical approval was granted by Tayside ethical committee (14/ES/0049). Informed consent was obtained from all the patients before their biopsy procedures for the reported study. The prostate biopsies were obtained using trans-rectal ultrasound (TRUS) guided needle biopsy in men suspected with PCa. Each biopsy was a circular core approximately 1 mm in diameter and 1-2 cm in length. The biopsy specimens were processed using a routine pathology protocol and reported by an experienced histopathologist blinded to the SHG results. The procedure included fixing with formalin, embedding in paraffin, sectioning with a microtome and staining with haematoxylin and eosin (H&E). After processing, the stained histologic section had a thickness of ~5 µm, and was mounted

between a glass slide and coverslip. Although staining is not required for SHG imaging, it is necessary for the histopathologist to report the cancer aggressiveness and beneficial for this study to correlate SHG with the histopathological results from the same slide.

For estimation of collagen alignment around cancerous lesions, 42 biopsy samples were imaged (36 cancerous and 6 benign) using the SHG microscopy in total. The malignant PCa samples further contained 6 sub-groups according to varied Gleason score: 3+3, 3+4, 4+3, 4+4, 4+5, and 5+4 with six core biopsies in each group. The spectrum provided sufficient numbers to study cancer heterogeneity using SHG.

5.3.2 Multiphoton SHG microscopy

An upright Multiphoton microscope TCS SP8 MP (Leica) at Dundee Imaging Facility was utilized to image the histopathology slides as illustrated in Figure 6.5. The tunable near-IR laser (Spectra-Physics InSight DeepSee) produced linearly polarized pulses spectrally centred at 880 nm. After spatially filtering and collimation, the beam was sent to the galvo-scanner. Incident light at 880nm was focused onto the sample with a Leica HC PL Fluotar 10x 0.3 NA objective. Due to the momentum conservation, SHG signal is especially directional and emitted mainly in the forward direction, being collected by a 0.9 NA condenser lens. The SHG signal was then filtered through a laser blocking filter (SP 680) and an SHG bandpass filter (440/20) and detected with a standard photomultiplier.

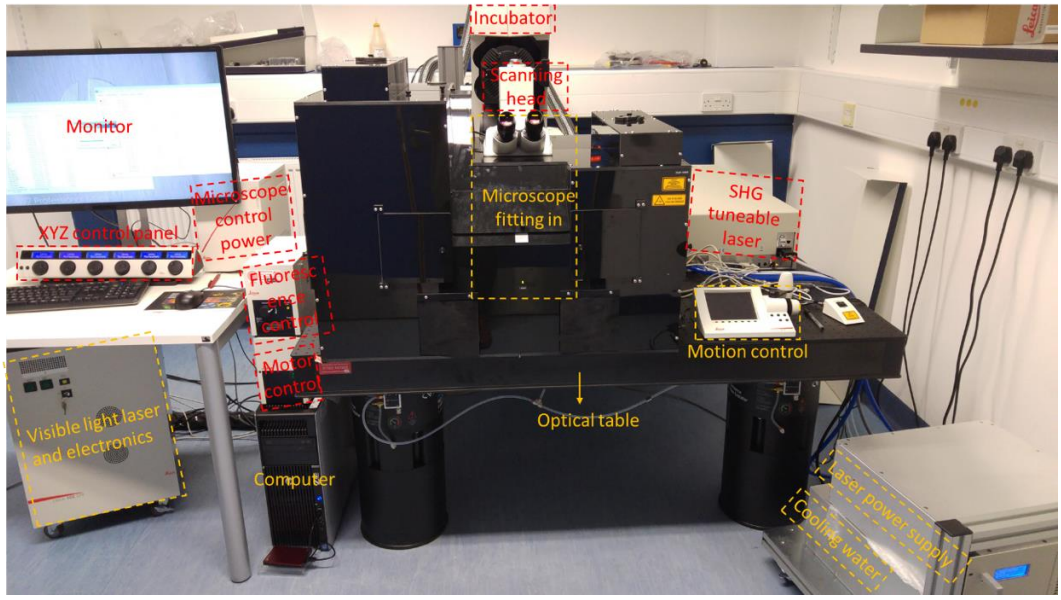

Figure 5.5 System configuration of the multiphoton microscope TCS SP8 MP (Leica).

The SHG laser power was adjusted to around 50 mW so that sufficient signal was obtained without any obvious damage to the sample. The transmitted light image was obtained from a 488 nm laser and collected in the forward transmitted light position using a 483/32 filter. A combination of z-stack and tile scan was used to acquire the whole area of the biopsy section automatically. Using identical settings, 12-bit images of 3352x3352 pixels were acquired using LAS X (Leica Application Suite X). A table with more details of the parameters applied in this study is demonstrated below.

Table 5.1 Parameters applied in the study of prostate biopsy using SHG microscopy.

Parameters	Value
Dimensions	
Logical size (X × Y)	3352 × 3352 pixels
Physical size (X × Y)	1.11 × 1.11 mm
Pixel size (X × Y)	330.39 × 330.39 nm
Z-step size	5 µm
Channels	
Cyan-scale SHG image	12 bits
Grey-scale transmitted light image	12 bits
Confocal settings	
Scan speed	400 Hz
Objective name	HC PL FLUOTAR 10x/0.30 DRY
Frame average	1
Line average	2

5.3.3 Image analysis of SHG images

The alignment of collagen fibres in each section was quantified using Fourier transform second harmonic generation (FT-SHG) adapted from the reported studies [172-178, 180]. The processing algorithms were developed in the Matlab platform (Matlab R2015b, the MathWorks).

Fourier transform SHG

Using a 2D Fourier transform (FT), the image contents were decomposed into a superposition of harmonic functions (of different amplitudes and angles) along two axes, where the spatial frequency is the modulation in intensity in the image per unit distance. This method is to identify the quantitative parameters that represent the collagen orientation in the prostate biopsies through assessment of the spatial frequencies in an image using a 2D-FT. In a given plane, the direction the majority of fibres tend to align along is defined as the preferred orientation. In 2D-FT, the high amplitudes on average orient perpendicularly to the preferred orientation.

As shown in Figure 5.6 (a), the regions where collagen fibres had preferential orientation were labelled as anisotropic (Figure 5.6 (b)) and regions with no preferential orientation (many different directions) were labelled as isotropic (Figure 5.6 (e)). The 2D-FT images (Figure 5.6 (c) and (f)) were created by applying fast Fourier transforms. It was integrated radially across different angles that resulted a plot of amplitude as a function of orientation angle. Gaussian fits were then applied to the plot. The centre of the fit illustrated the orientation of fibres as displayed in Figure 5.6 (d), and the width of the fits was the measurement of the randomness by which the fibres were distributed. In the angular power spectrum, the desired signal was selected with over -20dB of the highest amplitude in order to exclude background noise. Based on the experimental observation and the literature [26], the anisotropic region was represented by no more than four peaks, while isotropic region resulted in multiple peaks (Figure 5.6 (g)) at least five.

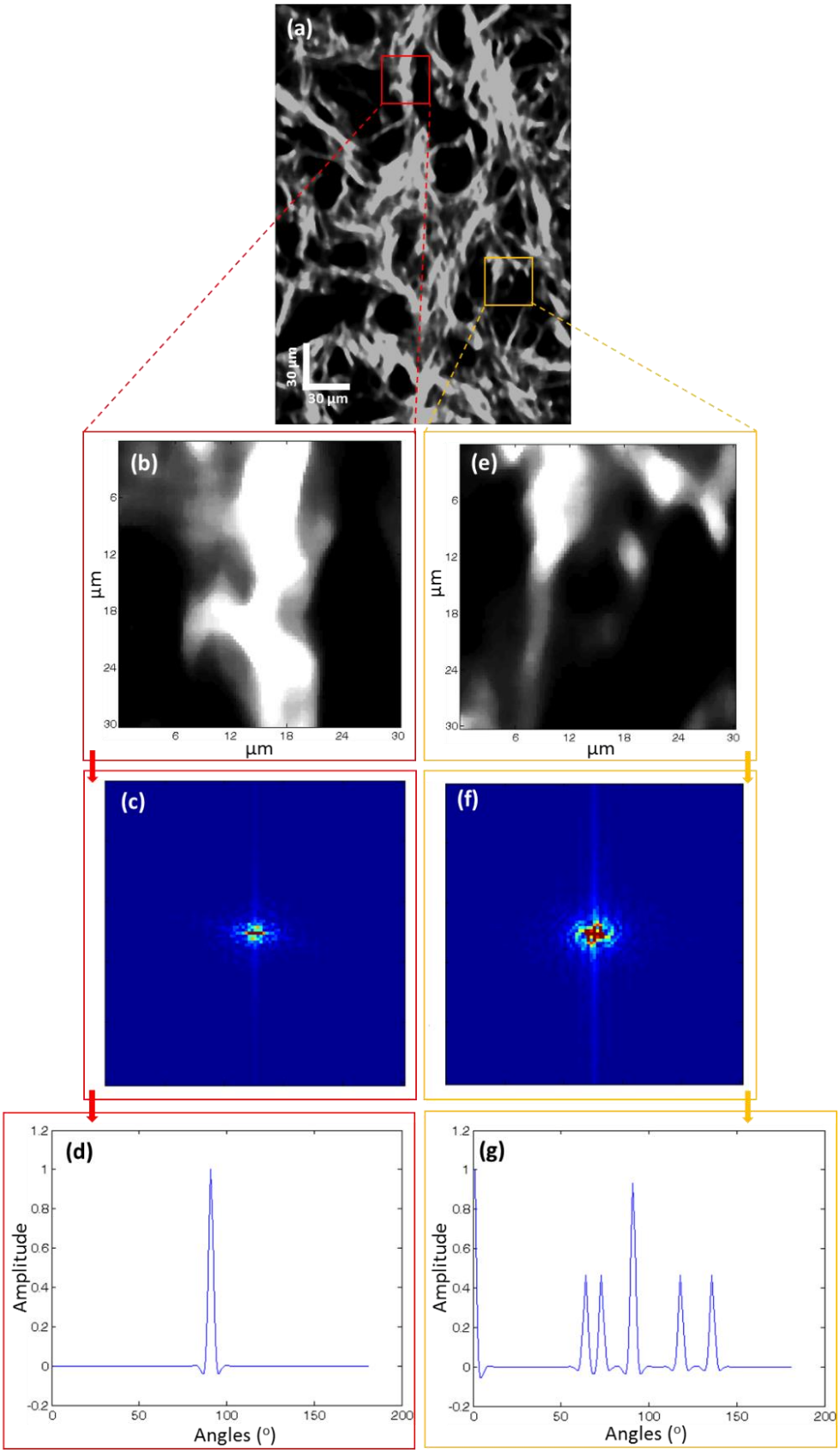

Figure 5.6 Imaging processing of SHG image of collagens in a malignant prostate biopsy. (a) Grey-scale image, typical (b) anisotropic and (e) isotropic collagen fibres after segmentation, 2D-FT images of the (c) anisotropic and (f) isotropic fibres, and the line plots of the orientation distribution of the (d) anisotropic and (g) isotropic fibres. Scale bar is 30 µm.

Orientation illustration

To calculate the preferred orientation more quickly, the original image was divided into subimages as illustrated in Figure 5.7 and categorized into three groups: negligible, anisotropic, or isotropic. Negligible (NN) was defined if the SHG intensity in the area was low or nearly dark. The sub-images where collagen fibres had preferential orientation were labelled as anisotropic (AA) and sub-images with many different directions were labelled as isotropic (II). In Figure 5.7, NN was labelled with blue, whilst II orange, and the rest of them were illustrated with the preferred orientation.

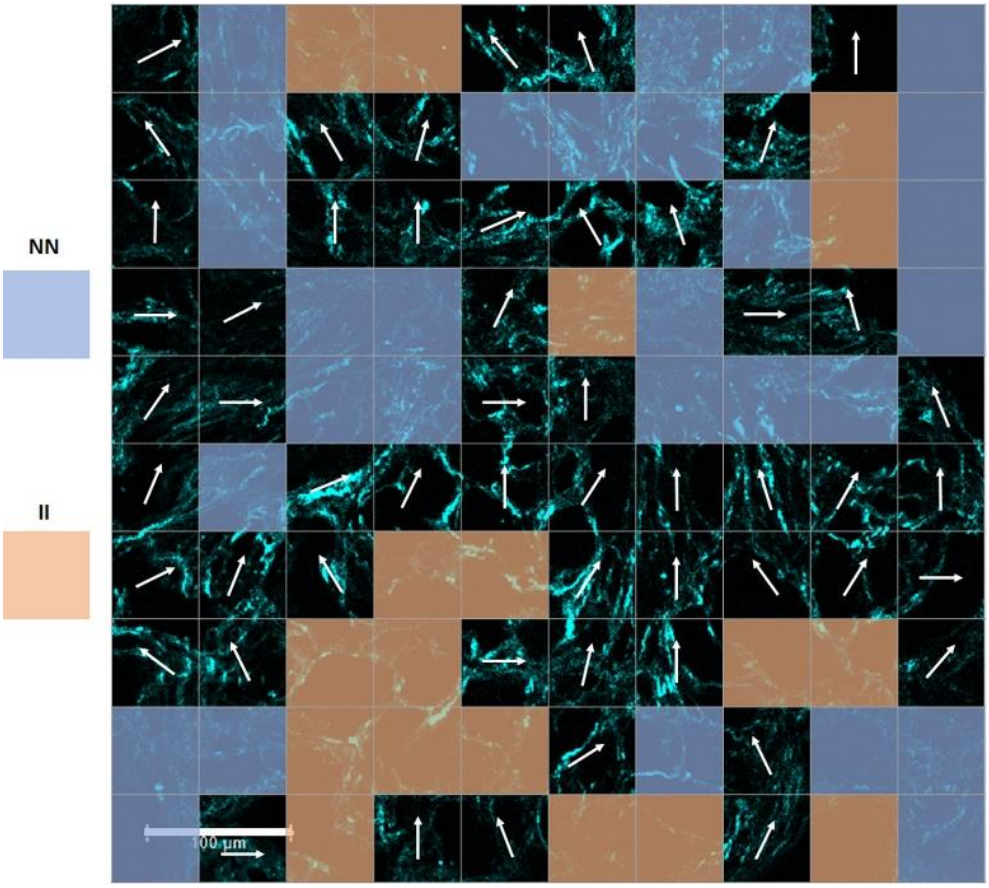

Figure 5.7 Sub-images analysis of collagen orientation in malignant prostate tissue. Dark or negligible (NN) ones are indicated in blue, and isotropic (II) ones are marked with orange. Scale bar is 100 µm.

Lastly, the overall orientation of the collagen fibres in each entire biopsy was quantified by applying A:I ratio (the ratio of the number of anisotropic (AA) to isotropic (II) subimages). The aim is to compute the regularity in collagen fibre orientation and compare it across the core biopsy samples of different Gleason score.

$$A{:}\,I\ ratio = \frac{Anisotropic\ subimages}{Isotropic\ subimages}$$

5.4 Results

5.4.1 Normal and malignant prostate biopsy

The fibromuscular stroma is about half volume of the gland, and mainly consisted of smooth muscle and connective tissue. The H&E staining method can depict the tissue structure and cellular details, while the molecular structure in the ECM is missing. In this study, the H&E stained images were used as the reference standard.

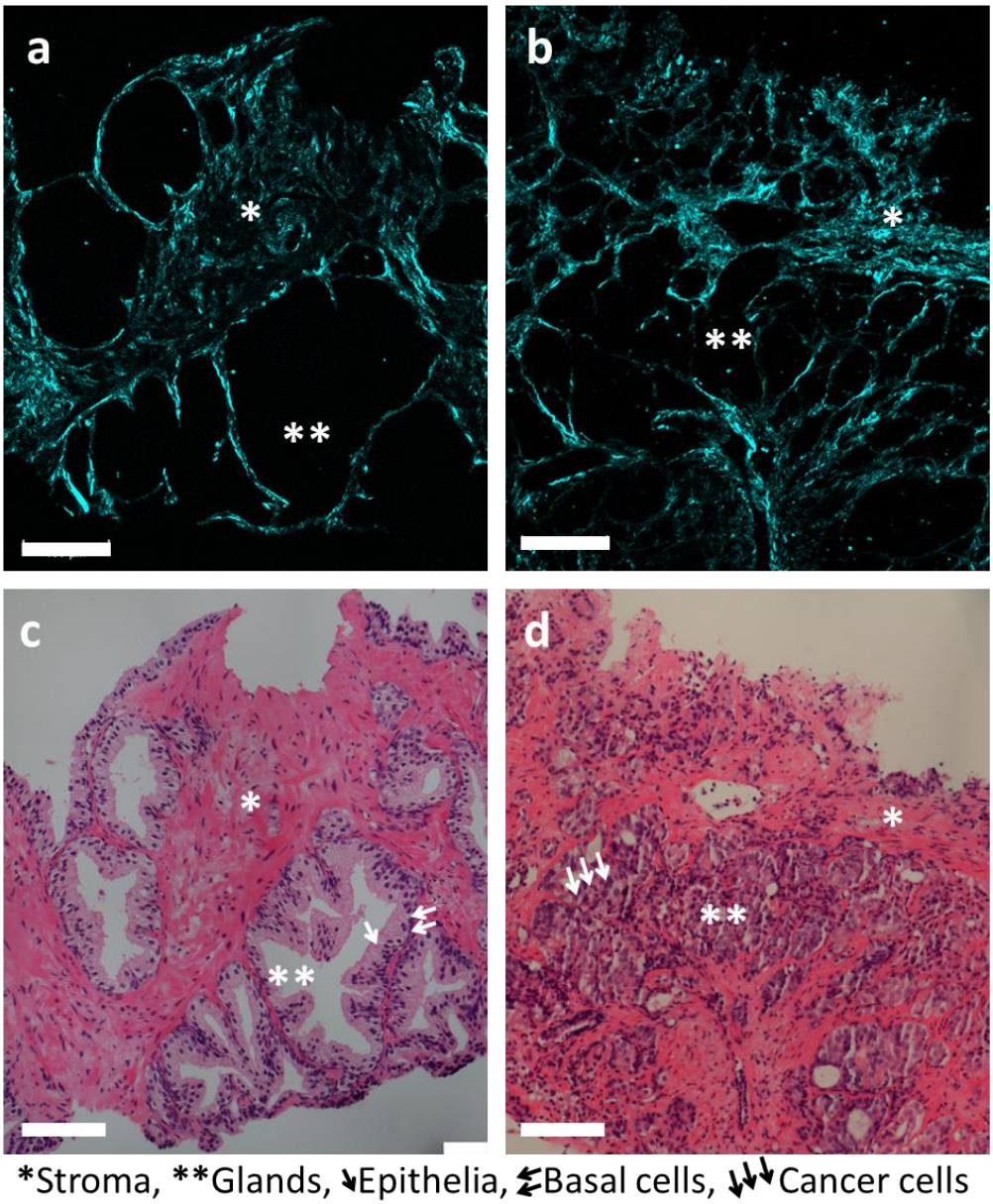

Figure 5.8 Comparison between benign and malignant prostate biopsy. SHG images of collagen alignment in (a) normal and (b) malignant prostate biopsy. Histological images of (c) normal glands and (d) fused glands occupied by cancer cells. Scale bar is 100 μm.

Figure 5.8 (a) demonstrates that the SHG imaging provides the collagen distribution across the whole tissue. As epithelia or basal cells do not produce a detectable SHG signal, only the fibromuscular stroma is evident in the SHG channel with a substantial number of collagen fibres at different orientations. As shown in Figure 5.8 (c), the normal prostate is composed of a gland and surrounded stroma. The normal gland has a papillary projection view, and is confined by two layers of cells. The inner layer is columnar epithelia and the outer layer is cuboidal basal cells. The epithelium is about two to four times of the height of the basal cell.

When cancer cells develop in the prostate, the basement membrane is lost and the epithelial layer is also disturbed. In some advanced cases of PCa, the cancer cells can even intrude into the stroma. By comparing Figure 5.8 (a) and (b), from normal to malignant prostate, the shape of the gland can change from papillary to reticular as the two layers that lined the gland are disrupted. In Figure 5.8 (b), the outlines of the glands are clearly observed to be fused together. The cancer cells are clustered and indicated by three arrows in Figure 5.8 (d). It is found that the collagen fibres tend to be more oriented in the malignant prostate biopsy in Figure 5.8 (b).

5.4.2 Characterization of Gleason pattern with SHG

The SHG images in Figure 5.9 (1a-4a) are presented with the corresponding transmitted-light images in Figure 5.9 (1b-4b) from a 488 nm laser from the same imaging area. The transmitted light detector produces a greyscale image in which the nuclei are dark and the rest of the tissue grey. Figure 5.9 (1c-4c) fuses the SHG channel and transmitted light data together to demonstrate both the cellular and surrounding matrix in a single image. Pathologically, the malignancy of PCa was categorized by Gleason score according to the cell pattern under the microscope. Thus the SHG results are also correlated with the images from traditional light microscope. As shown in Figure 5.9 (1d-4d), the transmitted-light images are similar to those from a conventional light microscope where the nuclei are blue and the cytoplasm and ECM are pink.

For Gleason 3+3, the SHG signal between the glands is more than that in the higher grade of core biopsies. Also the margins of glands of Gleason3+3 are still closed in shape, but these became fainter and even partially lost in Gleason 3+4 and 4+4. When the cancer is more aggressive, the cancer cells fill up the gland and some go into the stroma as well. The glands are fused together, and there are only sheets of cancer cells left in Gleason

4+5 with no glandular shape remaining. In SHG images, the different pattern of Gleason score can be distinguished by distribution and orientation of collagen fibrils. Across all the samples in the SHG images, the reticular pattern is observed as expected, but the size and shape vary from core to core and from region to region depending on tissue and cancer grade.

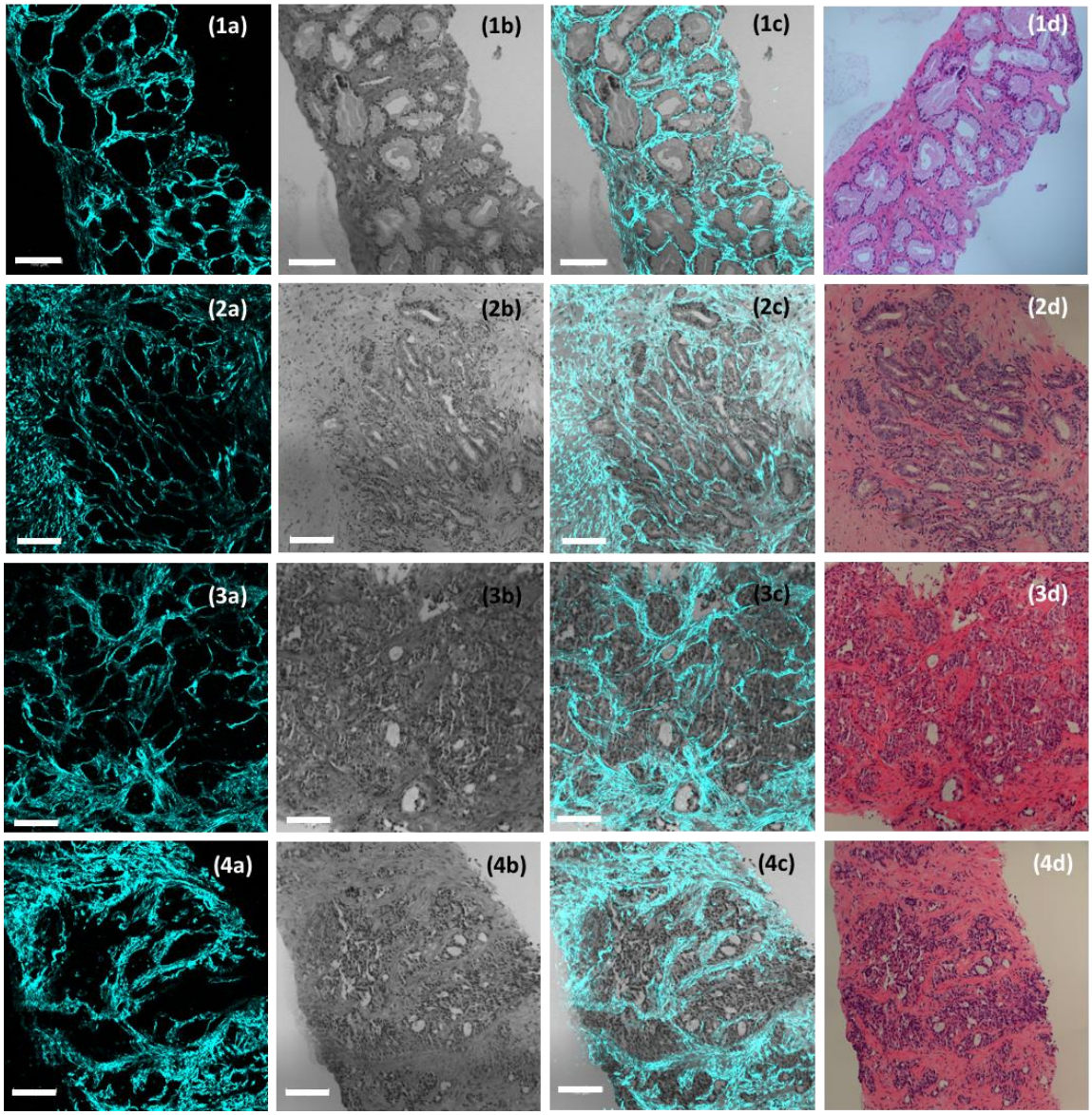

Figure 5.9 Core biopsies with increasing Gleason score. (a) SHG images, (b) transmitted-light images, (c) overlay images and (d) conventional light microscope of (1) Gleason 3+3, (2) 3+4, (3) 4+4, and (4) 4+5, respectively. Scale bar is 100 µm.

5.4.3 Statistical analysis

To quantify the accuracy of the method described above, a systematic statistical analysis was also carried out for all the prostate core biopsies obtained in the study. As shown in Figure 5.10, the orientation (A:I ratio) of malignant samples is 2.37 ± 1.34, approximately twice that of benign samples (1.34 ± 0.19). Hence, the malignant samples have a higher degree of preferred alignment along a single direction compared to the normal ones. The p-value between benign and malignant biopsies is 0.053.

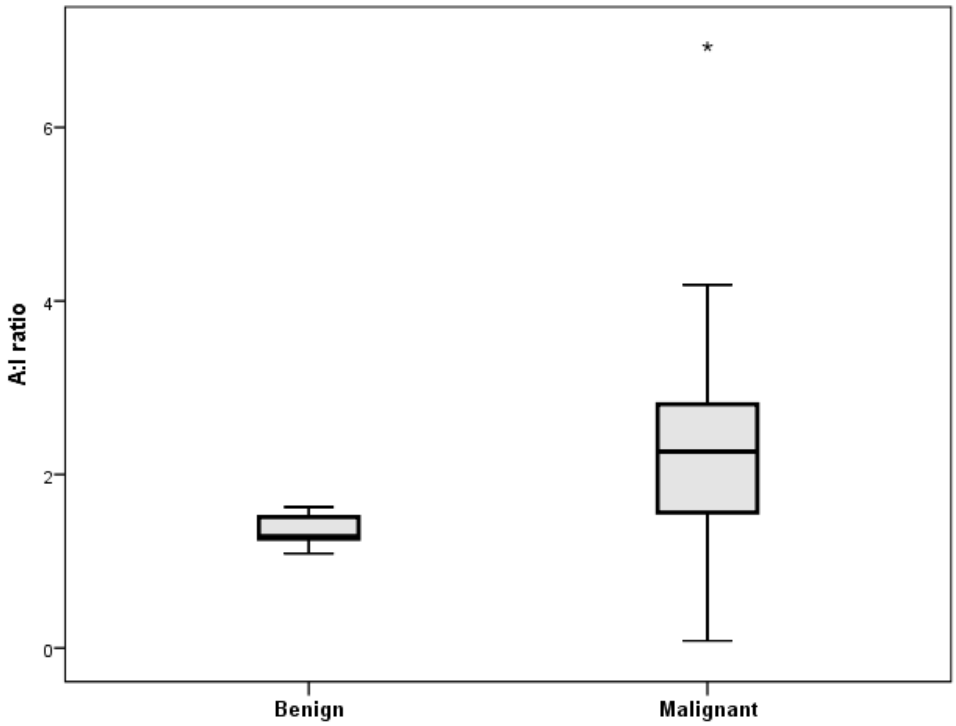

Figure 5.10 Whisker plot of the orientation (A:I ratio) in benign and malignant core biopsies.

Meanwhile, the biopsies diagnosed with the same Gleason sum but different primary and secondary Gleason grades were also analysed using FT-SHG method. As shown in the Whisker plot in Figure 5.11 (a), Gleason 4+3 is less anisotropic than Gleason 3+4. Gleason 4+5 also has a higher tendency of alignment than Gleason 5+4 in Figure 5.11 (b). It is found that among the biopsies with the same Gleason sum, the biopsy with a higher primary grade is likely to be less oriented than the one with a lower primary grade.

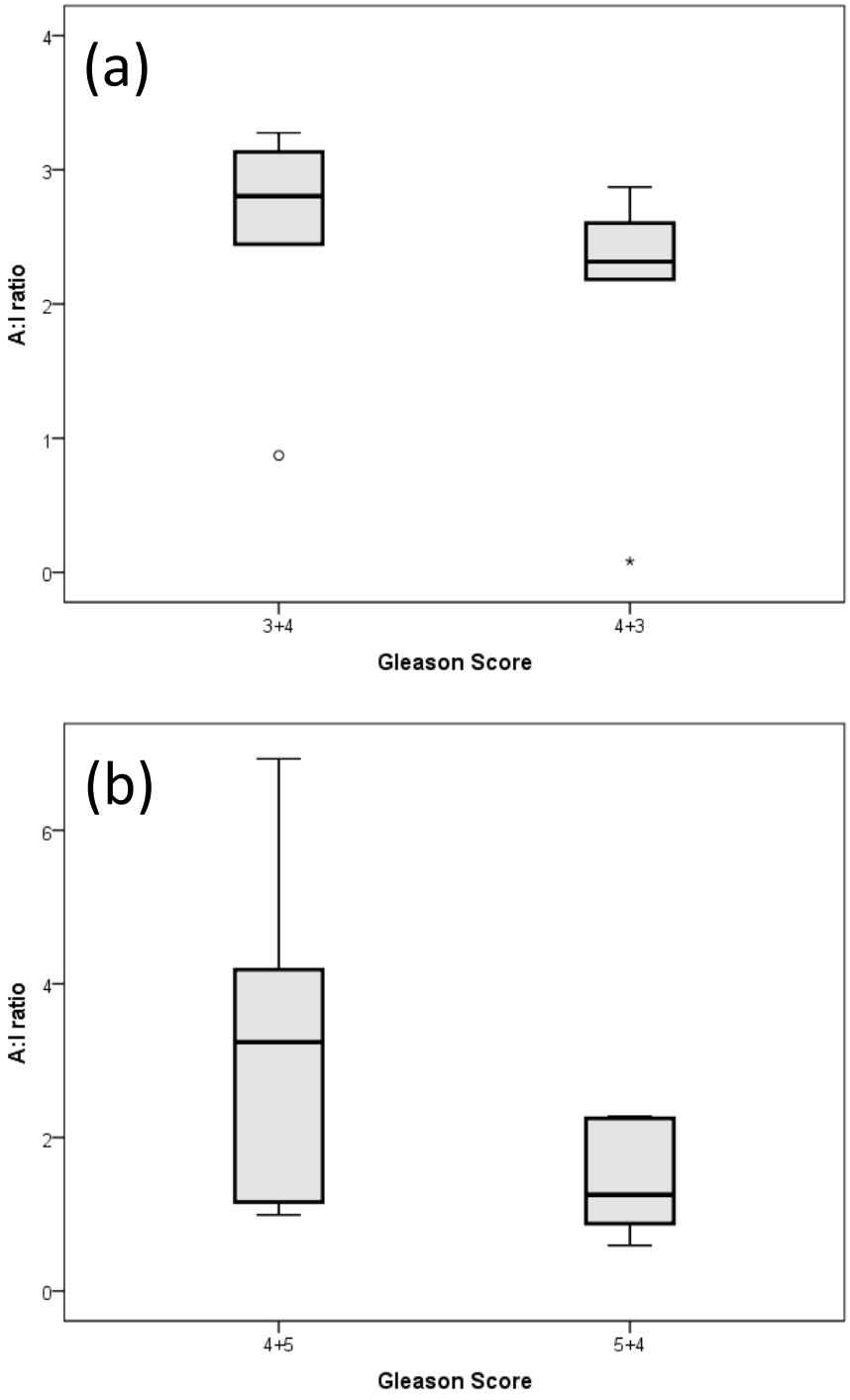

Figure 5.11 Whisker plots of the collagen orientation (A:I ratio) in (a) comparison between Gleason 3+4 and 4+3 and (b) comparison between Gleason 4+5 and 5+4.

In Figure 5.12, the orientation of the collagen fibres demonstrates a rising trend when the cancer aggressiveness increases, but it decreases for higher grade of malignancy such as Gleason 8 and 9. Among them, Gleason 9 is highly aligned, but the normal cores are almost isotropic.

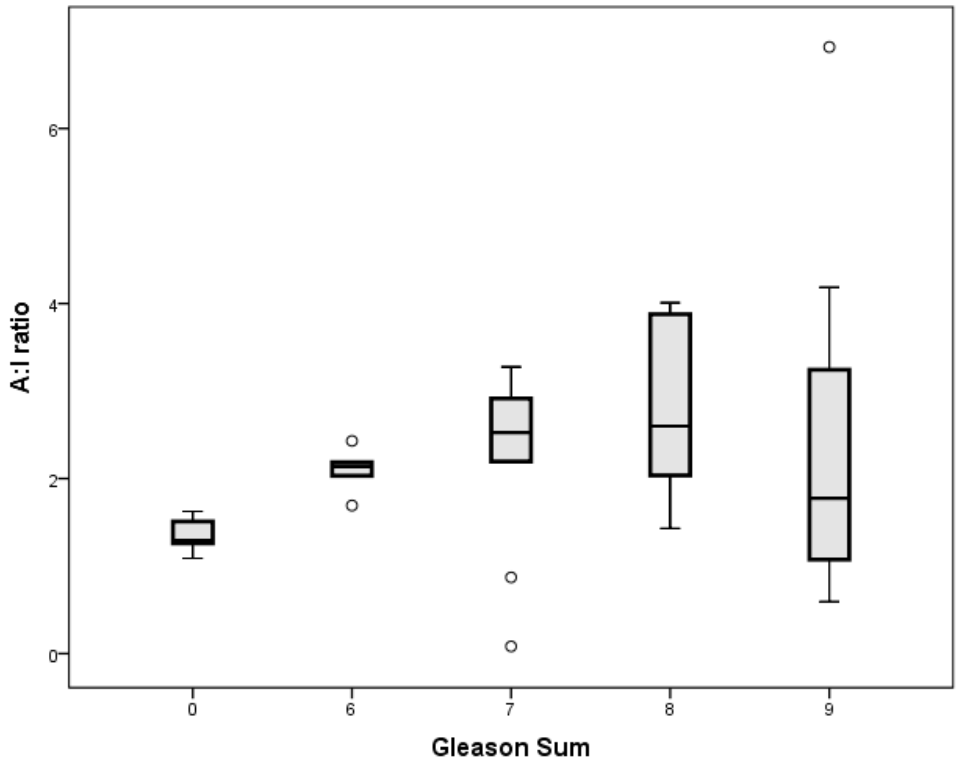

Figure 5.12 Whisker plot of the orientation (A:I ratio) among different Gleason sum.

5.4.4 Correlation between SHG and OCE

Elastography can detect subtle elasticity difference among the biopsies with a high-resolution OCE system, and SHG can illustrate collagen distribution and orientation with the multiphoton microscopy. The correlation between OCE and SHG is of significant interest. The prostate tissue stiffness acquired in Chapter 4 were correlated with the collagen orientation in this chapter.

As illustrated in Figure 5.13, in general, the lower Young's modulus, the less oriented the collagen fibres will be. However, no obvious linear or polynomial relationship was noticed between the fibre orientation and the tissue stiffness using average, maximum or threshold methods. The most important reason could be the unbalanced sample size of two studies. To further investigate the correlation between the two values, a larger number of biopsies is required. Notwithstanding, the combination of the images acquired from both modalities is illustrative to understand the relationship between the PCa cells and the extracellular matrix.

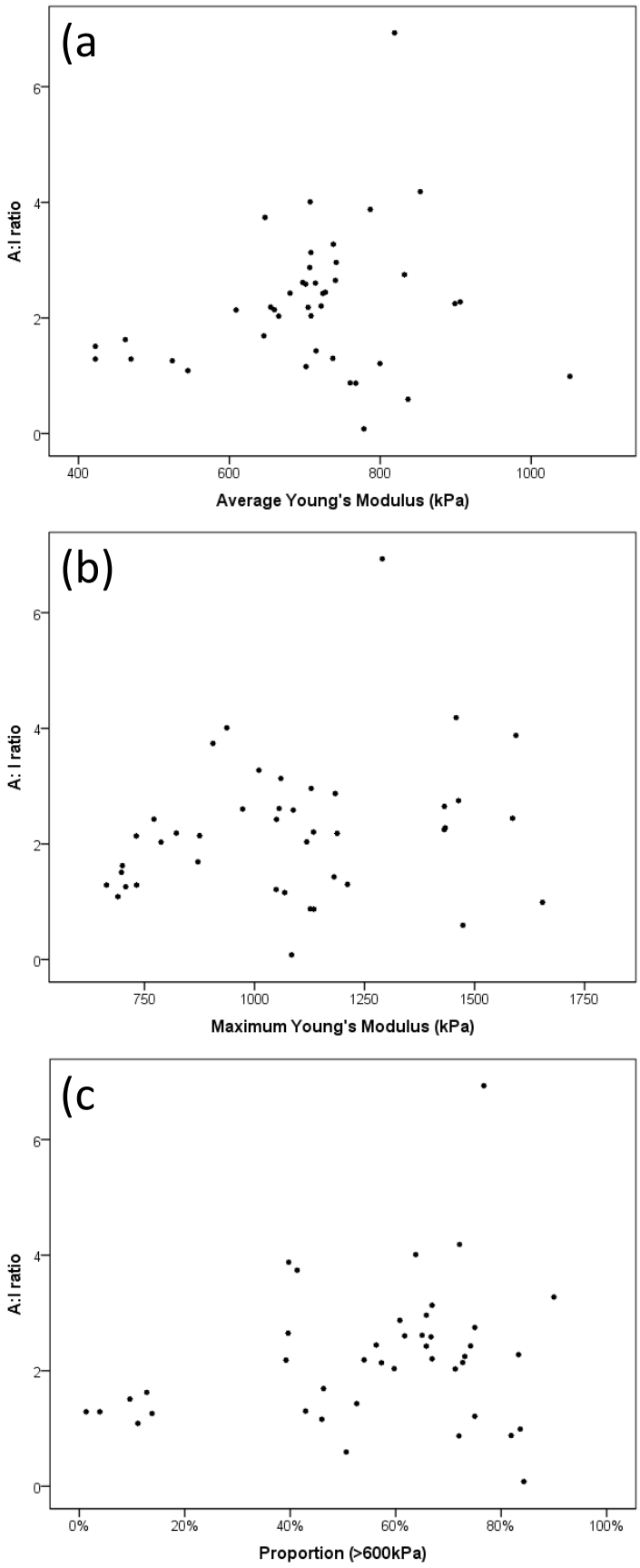

Figure 5.13 Scatterplots of the correlation of Young's modulus and collagen orientation (A:I ratio) using the (a) average method, (b) maximum method and (c) threshold method.

5.5 Conclusion and Discussion

The prostate has a fibromuscular stroma which is composed of fibroblast, smooth muscle cells, and an ECM rich in collagen fibres [165] that provides mechanical strength and flexibility to the tissue [14, 46]. Reactive stroma [14, 15, 46, 165] was reported to involve during early PCa development and promote tumorigenesis and progression with stromal cell phenotypes switching and ECM remodeling and stiffening. In normal prostate, a 3D ECM network is formed with collagenous fibres of different thicknesses and different directions. Under conditions of tissue remodeling, the metabolic turnover is increased in the carcinomatous stroma compared to the condition of tissue homeostasis [46]. Another important protein in the ECM is elastic fibre providing flexibility for many vertebrate tissues [187] to stretch and recoil without damage, including skin, blood vessels and lungs. In the prostatic stroma, elastic fibres are the least abundant elements. There are, however, only scant data [46] on the role of elastin or elastic fibres in benign prostatic hyperplasia (BPH) and tumour invasion in PCa.

Costa et al. [188] revealed a significant role of collagen reticular fibres in BPH while the difference of the volumetric density of elastic fibres in the control and BPH groups was not statistically significant. Zhang et al. [47] also suggested that the tissue hardness of prostatic tumours is mainly dependent on the collagen type I content. It was observed that the collagen type I was significantly more in the stiffer area of the prostate, whilst no significant difference in the area ratios of the elastic fibers between the soft and stiff groups. Also the ratio of collagen type I and type III was reported to be significantly higher in malignant than in benign lesions of the prostate. Therefore, only collagen was investigated in this study rather than elastic fibres. Moreover, an increase in collagen crosslinking was found to contribute to the overall stiffening of the sounding microenvironment of breast cancer [189]. Reoriented collagen fibres have been reported in the stroma of breast cancer tissue to facilitate cell invasion [166, 167]. However, little is known about the role of orientation of collagen fibres in PCa progression.

The collection of collagen fibres produce strong SHG signal. In this study, the prostate biopsy was scanned with a multiphoton microscopy with the SHG signal collected in the forward direction to compare the SHG images of normal and malignant prostate biopsies, and investigate those with different Gleason scores. All the samples were correlated with histological images using H&E staining, which is the golden standard for confirming presence or absence of prostate cancer. Note that epithelial layer and cancer cells are missing in the SHG images since they do not produce a detectable SHG signal. It is found

that collagen in malignant prostate cancer has a reticular instead of papillary pattern. However, the reticular pattern disappears in the highly advanced cancer such as Gleason 4+5. When the cancer cells are proliferating in an uncontrolled manner, the basement membrane is broken down, the glands are fused together and the cancer cells invade the gland and even the stroma. As a result, the SHG signal between glands is gradually lost.

Apart from morphologically different collagen patterns, we applied the FT-SHG to quantify the preferred orientation of collagen fibres in each biopsy. Generally, malignant cores are found to be more aligned than the normal ones. Besides, the higher the Gleason score, the larger the A:I ratio. It means that the collagen fibres tend to be more oriented as the prostate cancer becomes more aggressive. Note that there is a small fluctuation in the advanced grade of cancer. Among the groups, the value for the Gleason 8 is similar to Gleason 9. Moreover, Gleason 4+3 is more isotropic than Gleason 3+4 with a lower A:I ratio. Similarly, Gleason 4+5 also has a higher tendency of alignment than Gleason 5+4. Therefore, a higher primary grade leads to less oriented collagen fibres and a lower A:I ratio for the scenario of the biopsies with the same Gleason sum.

The A:I ratio acquired from breast biopsies in [176] was 2.8 ± 1.5 for normal samples and 11.6 ± 6.7 for malignant ones. Both of them are at least twice the values obtained from the prostate biopsies. There could be several reasons for this discrepancy. The first is the nature of target tissue and the breast tissue is better differentiated in comparison to prostate tissue. Breast tissue contains much more collagen, and a different type of collagen structure could lead to a higher level of alignment. The second reason could be the FT-SHG method we utilized in this study is slightly different, such as the threshold, size of the sub-images, and resolution of the original images. Another possible reason is the sampling size of the study that is quite important in considering the differences. In this study, the sample diversity is still limited which has 24 biopsies for the preliminary study [190] and 42 biopsies for the overall study [191]. To overcome the weakness, a future study with a larger sample number is necessary.

Though the collagen alignment is proved to be correlated with the malignancy of cancer, there is no noticeable relationship between the tissue stiffness and the collagen assembly in the cancer matrix. It could be due to the unbalanced sampling size of using OCE and SHG, as this research thesis include 720 biopsies with OCE measurement but only 42 biopsies with SHG quantification. To further investigate the correlation between the tissue stiffness and collagen orientation, a larger sampling size of prostate biopsies is required. It appears that the tissue stiffening is a comprehensive result of various cells,

ECM molecules, intra- and inter- cellular or molecular architecture, etc. rather than collagen alone. Future works are also needed to investigate the role of other components, such as smooth muscle cells and elastin that provide tissue strength and flexibility together with collagen. These will add significant value to understand the role of tissue rigidity in PCa progression.

In summary, SHG provides high-resolution images of collagen distribution in prostate core biopsies. It is a noninvasive imaging method without the need for staining or ionizing radiation, but it can feasibly be applied to versatile types of biological samples with high-contrast morphological details of collagen fibres. The collagen orientation details provided an answer for the tissue stiffness increase in the malignant prostate compared with the benign one. Moreover, quantitative FT-SHG demonstrated that the A:I ratio can be used as a biomarker for the diagnosis of PCa. There is significant potential to develop a systematic correlation between the Gleason score and the preferred orientation of the collagen fibres with a large number of patients recruited.

Chapter 6. Conclusion and Perspectives

Prostate cancer (PCa), the most common cancer in men across the UK, is a multifocal disease with characteristic heterogeneity and foci that can range from low-grade indolent to aggressive disease. In current clinical care, serum prostate-specific antigen (PSA) level and digital rectal examination (DRE) are not reliable enough to suspect PCa, albeit commonly used as routine diagnostic methods for PCa. Moreover, the well-established diagnosis, trans-rectal ultrasound (TRUS) guided biopsies, is based on Gleason scoring that usually requires the expertise of a trained histopathologist. However, an inter-observer variation exists between two histopathologists besides a large discrepancy existing on initial biopsy and after the final radical prostatectomy (RP).

A reliable diagnosis is of high demand to make an optimal decision for PCa treatment. Photonics, especially vibration optical coherence elastography (OCE) and second harmonic generation harmonic (SHG) are novel high-resolution imaging modality for characterisation of biological tissues. This research thesis presented original works implementing these two photonic modalities in characterization of the microstructural details of prostate tissue obtained from a large number of TRUS guided biopsies. The two complementary methods appeared to be highly accurate in differentiating cancer from normal benign prostatic tissue. It also provided accurate characterisation of Gleason grade based on the measurement of Young's modulus (tissue stiffness) and orientation of collagen around malignant lesions.

This chapter summarizes the main research outcomes, discusses some limitations of the current studies, and recommends some future works that could be generated from this research thesis, as well as a final remark that comes at last.

6.1 Research Outcomes

This research thesis aims at searching a reliable and quantitative diagnostic modality to achieve higher diagnostic accuracy. It starts with a thorough literature study of the current PCa diagnostic methods and the varied sensitivity and specificity have been discussed. Optical imaging modalities were selected for this research owing to the super high resolution over traditional ultrasound imaging. Optical coherence tomography (OCT) imaging with resolution in the micro scale stands out from the other light imaging

instruments. The merit of using OCT is also contributed to the reasonable imaging depth compared to the conventional microscope. Another advantage of OCT is the feasibility to perform elastography on the biological tissues. Mechanical properties of tissues have are related to the pathological process of breast disease and cancer.

6.1.1 Study of fixative effects on the tissue stiffness using vibration OCE

To enable elastography, a shaker was utilized to generate vibration to the tissues. The generated vibration signal was analysed and tuned to achieve optimal performance for the use in the detection of prostate biopsies. Before testing on the prostate tissues, this system setup was first applied for the monitoring stiffness change of tissues embedded in the fixatives. One of the aims is to verify the capability of the new setup for the measurement of biological tissues in small scale. The other aim is to study the time required for the prostate biopsy tissue to achieve full fixation as the prostate biopsy is usually deposited immediately in the formalin solution after biopsy procedure but little is known about the fixative effects on the tissue stiffness. Additionally, this study is of significant clinical impact as many fixed or preserved tissues has been used for clinical training and biomedical instrument design.

Therefore, the effect of tissue stiffness change from two commonly used fixative or preservative were included in this study, namely formalin and Thiel solution. Formalin is the most commonly used fixative across the laboratory or clinics in the world for either short-term or long-term storage of tissues, while Thiel cadavers are normally kept in a tank for at least 3-6 months before use. To replicate the fixation process, their time effect had been tested on five different tissue types which were trimmed to the size similar to the prostate biopsy for a long period up to 6 months with a precisely controlled timeline.

It is found that all the different kinds of tissues immersed in 10% formalin dilution display an ascending trend of the elasticity changes, while those immersed in Thiel solutions almost remain constant Young's Modulus for all tissue types with only small fluctuations. That is to say, Thiel solution is more likely to retain lifelike textures and properties of tissues, enabling surgical and clinical training more approaching to the reality compared to traditional rigid formalin fixed specimens. Most of the stiffness changes of tissues embedded in the formalin solution ceased after 6 hours of fixation, but some fluctuations were noticed. After 24 hours, the tissues are fully fixed without noticing change of elasticity. This is a crucial guideline for the following study of prostate biopsies. Besides,

the porcine fat tissue was not sensitive to the fixation effect of formalin. This is probably due to the main component of adipocytes.

In this study, the new OCE setup using vibration method is proved to be a powerful imaging technique in characterizing fine tissue structure and elasticity distribution simultaneously. These findings provide a thorough understanding of the effect of formalin and Thiel solution on tissue stiffness, which will be beneficial for the future design of fixed or preserved tissue for the training in both clinical and biomedical field.

6.1.2 Evaluation of prostate malignancy using vibration OCE

Based on the abovementioned work, this study further explores the potential of the vibration OCE in a large clinical study including 70 patients suspected with PCa. With the agreement with the local committee and the consent from each patient, this study incorporates both cross-sectional 2D and *en face* 3D imaging of the biopsy tissue with high resolution. The illustrated biopsy structural image and elastogram are highly correlated with the results from the histological photos and reports, respectively. It is manifested that OCE can reliably differentiate benign and malignant prostate tissues with high diagnostic accuracy (AUC > 90%). Statistically, the stiffness of cancer biopsies was approximately 57.63% higher than that of benign ones with corresponding stiffness values of 698.43 ± 125.29 kPa versus 443.07 ± 88.95 kPa. This technique also demonstrated potential in characterising different aggressiveness of PCa based on the change of tissue morphology and quantitative mechanical properties. This is the first *ex vivo* study using vibration OCE in identifying PCa and characterising degree of malignancy with such a high diagnostic accuracy.

With the results generated from this large clinical studies using *ex vivo* prostate tissues, it will form a complete basis for future research using these techniques in *in vivo* assessment of PCa and intraoperative assessment of tumour margins. In summary, this study utilized the vibration OCE to estimate the Young's modulus of prostate biopsies, differentiate benign from malignant biopsies, as well as quantify the degree of malignancy. Thus, the Young's modulus of the prostate biopsy is potential to be used as a mechanical biomarker to detect PCa and distinguish cancer with different aggressiveness.

6.1.3 Investigation of prostate collagen matrix using SHG

Tissue stiffness increase is associated with the pathological change of the disease, and the second study of this research thesis has just proved this. The observed tissue stiffness is known as a result of cell density and remodeling of extracellular matrix (ECM). Collagen as the major structural and mechanical component in the ECM plays a key role in regulating tissue stiffness. This study pokes into the stroma of prostate tissue to investigate the interaction between the cancer cell and the surrounding ECM using SHG microscopy. It is a noninvasive imaging method without the need for staining or ionizing radiation, but it can feasibly be applied to versatile types of biological samples with high-contrast morphological details of collagen fibres. In this study, the SHG images of normal and malignant prostate biopsies were compared, as well as those with different Gleason scores. All the samples were correlated with histological images using H&E staining, which is the golden standard for confirming presence or absence of prostate cancer.

It was found that the collagen in malignant prostate cancer has a reticular instead of papillary pattern of benign biopsy. However, the reticular pattern disappears in the highly advanced cancer such as Gleason 4+5. When the cancer cells are proliferating in an uncontrolled manner, the basement membrane is broken down, the glands are fused together and the cancer cells invade the gland and even the stroma. As a result, the SHG signal between glands is gradually lost. Apart from morphologically different collagen patterns, the FT-SHG was utilized to quantify the preferred orientation of collagen fibres in each biopsy. In this study, A:I ratio adapted from previous study [176] was developed for the orientation of collagen fibres.

This ratio was proved to be powerful in revealing the alignment of collagen matrix. Generally, malignant cores are found to be more aligned than the normal ones. Besides, the higher the Gleason score, the larger the A:I ratio. It means that the collagen fibres tend to be more oriented as PCa becomes more aggressive. A small fluctuation is noted in the advanced grade of cancer. It is also found that a higher primary grade leads to less oriented collagen fibres and a lower A:I ratio for the scenario of the biopsies with the same Gleason sum. In summary, high-resolution images of collagen distribution were provided using SHG in prostate core biopsies. Moreover, quantitative FT-SHG demonstrated that the A:I ratio can be used as another biomarker for the diagnosis of PCa.

6.2 Limitations and Future Works

6.2.1 Study of fixative effects on the tissue stiffness using vibration OCE

Although the tissue was vacuum-packed before transferring to the OCE lab, there had been autolysis and decomposition to a certain extent. In addition, there was evaporation, especially on the surface of the tissue while preparing and scanning the sample. As a result, there might be some tissues partially dried that could result in an increased level of stiffness. This could also be attributed to the biochemical reactions and manual operation.

When preparing the porcine liver sample, the process of cutting and trimming the sample took considerably longer than the other tissues did as the liver sample was too soft to handle. In comparison, the preparation time for the chicken breast and porcine fat using a biopsy needle took less than one minute. The loss of moisture was minimised and well controlled in the other tissues, but relatively worse in the liver due to the nature of the tissue. As a result, the original value of elasticity of the liver was further increased and higher than literature reports [145, 146].

In the case of future work, fresh tissues obtained from the slaughter as soon as after mortem would be preferred where *ex vivo* studies of other tissues are required. After acquiring the tissues, they should be stored in the saline solution and kept on ice immediately to minimise tissue degradation before the scanning. If possible, the room temperature and moisture should be monitored as a reference parameter which might give rise to some difference of the acquired and real tissue stiffness.

6.2.2 Evaluation of prostate malignancy using vibration OCE

It was noted that the Young's modulus obtained from this study was higher than literature [71, 72] and the *ex vivo* verification of the stiffness value of the human prostate tissue is lacking. Following the requirements of a routine histopathological examination, the human prostate biopsy samples in this study were fixed in formalin before the OCE experiment, which ensures the accuracy of the following histopathological analysis of the cellular structure of the fixed biopsy. The formalin increases the tissue stiffness which, to some extent, can bring bias to the final elasticity of prostate biopsies. Nevertheless, it was not feasible to perform an *ex vivo* verification of the human prostate tissue stiffness using traditional tensile or compressive test. Such invasive mechanical tests can cause damage to the tissue and as a consequence make the histopathological analysis of the tissue

impossible. In our experiment, however, timeline was precisely controlled to finish every experiment. Since all the 720 samples were fully fixed [160] in the formalin for 24 hours before the OCE scanning, the extent of stiffness increase should be the same for all the benign and malignant prostate tissues.

For the future work, *ex vivo* mechanical verification using porcine prostate would be suggested here. Using the same biopsy needle, 12 biopsies can be taken from different regions of the porcine prostate in accordance with the transrectal ultrasound guided biopsy (TRUS) protocol. Then the results from vibration OCE on each porcine prostate biopsy can be correlated with the results from the mechanical test in order to verify the Young's modulus value obtained from vibration OCE. Also, a new recruitment of patient underwent RP is necessary to generate a solid data for the prediction of the histological grade of the RP using OCE. Though promising results have already presented, it is a preliminary study with only limited number of participants. Also, with the improvement of system configuration and synchronization program, the acquisition time for the 3D data will be much faster.

On the basis of the findings from this study, another future perspective is the *in vivo* study with the OCE needle probe to realise real-time diagnosis of PCa and accurate characterisation of the malignancy. Although the penetration depth of OCT is limited due to the attenuation from light scattering, the instrument can be integrated with optical fibre probes in catheters, endoscopes, laparoscopes, and needles to access tissues deep within the body. It is required to perform an *in vivo* feasibility study of such design equipped with an elastography function in a porcine model first before the plan of a human clinical study. After the realization of such an *in vivo* instrument, not only *in situ* detection and characterisation of PCa is possible to allow a more precise focal treatment, but intraoperative examination of excised prostate tissue is feasible to provide the surgeon with an assessment of tumour margins within minutes of prostate removal.

6.2.3 Investigation of prostate collagen matrix using SHG

In the study of collagen orientation using SHG, the A:I ratio acquired from breast biopsies in [176] was 2.8 ± 1.5 for normal samples and 11.6 ± 6.7 for malignant ones. Both of them are at least twice the values obtained from the prostate biopsies. There could be several reasons for this discrepancy. The first is the nature difference of target tissue and the breast tissue is better differentiated in comparison to prostate tissue. Breast tissue

contains much more collagen, and a different type of collagen structure could lead to a higher level of alignment. The second reason could be the FT-SHG method we utilized in this study is slightly different, such as the threshold, size of the sub-images, and resolution of the original images. Another possible reason is the sampling size of the study that is quite important in considering the differences.

Though the collagen alignment is proved to be correlated with the malignancy of cancer, there is no noticeable relationship between the tissue stiffness and the collagen assembly in the cancer matrix. It could be due to the unbalanced sampling size of using OCE and SHG, as this research thesis include 720 biopsies with OCE measurement but only 42 biopsies with SHG quantification. This is also possibly because of the intrinsic complexity of the collagen-cell interaction. It could suggest that the stiffness increase is partially contributed by the collagen alignment, and partially by the cell density and intra- and inter- cellular force, etc. To further investigate the correlation between the tissue stiffness and collagen orientation, a larger sampling size of prostate biopsies is required.

Previous studies [47, 188] have revealed the role of the density of collagen fibres and type I collagen in the prostate elasticity increase. For the future perspective, the results of the collagen orientation using SHG can be cross correlated with collagen density and the type of collagen using picric acid-sirius red with polarized light microscopy. The prostate consists of epithelia, fibroblasts, smooth muscle cells, and various molecules of ECM. It appears that the tissue stiffening is a comprehensive result of various cells, ECM molecules, intra- and inter- cellular or molecular architecture, etc. rather than collagen alone. However, there are few limited studies reported on the importance of other components in the prostate tissue stiffening [47, 188]. Future works are also needed to investigate the role of other components, such as smooth muscle cells and elastin that provide tissue strength and flexibility together with collagen. These will add significant value to understand the role of tissue rigidity in PCa progression.

6.3 Final Remarks

In conclusion, this research thesis presented two novel optical imaging modalities aiming at increasing the diagnostic accuracy of current PCa detection, namely vibration OCE and FFT SHG. The overall study consists of three complementary sub-studies, which are inherently related to each other. In the one hand, promising results have manifested that the use of vibration OCE in detecting PCa with a high accuracy of 93.9% and can

differentiate malignancy with a significant difference. In the other hand, FFT-SHG can illustrate the different matrix structure between benign and malignant prostate tissues with an effective ratio parameter to quantify the collagen alignment. With the development of needle probe and the advancement of technology, the fuse of these two complementary modalities OCE/SHG is potential to be a powerful multimodal imaging tool in the *in vivo* assessment of PCa with small size and intraoperative examination of tumour margin, as well as improve the patient satisfaction.

References

[1] J. M. Correas, A. M. Tissier, A. Khairoune, G. Khoury, D. Eiss, and O. Hélénon, "Ultrasound elastography of the prostate: State of the art," *DIAGNOSTIC AND INTERVENTIONAL IMAGING*, vol. 94, pp. 551-560, 5// 2013.

[2] F. May, T. Treumann, P. Dettmar, R. Hartung, and J. Breul, "Limited value of endorectal magnetic resonance imaging and transrectal ultrasonography in the staging of clinically localized prostate cancer," *BRITISH JOURNAL OF UROLOGY INTERNATIONAL*, vol. 87, pp. 66-69, Jan 2001.

[3] M. S. Cohen, R. S. Hanley, T. Kurteva, R. Ruthazer, M. L. Silverman, A. Sorcini, *et al.*, "Comparing the Gleason prostate biopsy and Gleason prostatectomy grading system: The Lahey Clinic Medical Center experience and an international meta-analysis," *EUROPEAN UROLOGY*, vol. 54, pp. 371-81, Aug 2008.

[4] E. C. Serefoglu, S. Altinova, N. S. Ugras, E. Akincioglu, E. Asil, and M. D. Balbay, "How reliable is 12-core prostate biopsy procedure in the detection of prostate cancer?," *CANADIAN UROLOGICAL ASSOCIATION JOURNAL*, vol. 7, pp. E293-8, May-Jun 2013.

[5] P. A. Humphrey, "Gleason grading and prognostic factors in carcinoma of the prostate," *MODERN PATHOLOGY*, vol. 17, pp. 292-306, Mar 2004.

[6] T. A. Krouskop, T. M. Wheeler, F. Kallel, B. S. Garra, and T. Hall, "Elastic moduli of breast and prostate tissues under compression," *ULTRASON IMAGING*, vol. 20, pp. 260-74, Oct 1998.

[7] T. Shiina, K. R. Nightingale, M. L. Palmeri, T. J. Hall, J. C. Bamber, R. G. Barr, *et al.*, "WFUMB guidelines and recommendations for clinical use of ultrasound elastography: Part 1: Basic principles and terminology," *ULTRASOUND IN MEDICINE & BIOLOGY*, vol. 41, pp. 1126-1147, 5// 2015.

[8] J. Ophir, I. Cespedes, H. Ponnekanti, Y. Yazdi, and X. Li, "Elastography: A quantitative method for imaging the elasticity of biological tissues," *ULTRASON IMAGING*, vol. 13, pp. 111-34, Apr 1991.

[9] T. Varghese, "Quasi-static ultrasound elastography," *ULTRASOUND CLINICS*, vol. 4, pp. 323-338, Jul 2009.

[10] A. Sarvazyan, T. J. Hall, M. W. Urban, M. Fatemi, S. R. Aglyamov, and B. S. Garra, "An overview of elastography - an emerging branch of medical imaging," *CURRENT MEDICAL IMAGING REVIEWS*, vol. 7, pp. 255-282, Nov 2011.

[11] B. F. Kennedy, K. M. Kennedy, and D. D. Sampson, "A review of optical coherence elastography: Fundamentals, techniques and prospects," *SELECTED TOPICS IN QUANTUM ELECTRONICS, IEEE JOURNAL OF*, vol. 20, pp. 272-288, 2014.

[12] G. Guan, C. Li, Y. Ling, Y. Yang, J. B. Vorstius, R. P. Keatch, *et al.*, "Quantitative evaluation of degenerated tendon model using combined optical coherence elastography and acoustic radiation force method," *JOURNAL OF BIOMEDICAL OPTICS*, vol. 18, p. 111417, Nov 2013.

[13] A. Y. Liu and L. D. True, "Characterization of prostate cell types by CD cell surface molecules," *THE AMERICAN JOURNAL OF PATHOLOGY*, vol. 160, pp. 37-43, Jan 2002.

[14] J. A. Tuxhorn, G. E. Ayala, and D. R. Rowley, "Reactive stroma in prostate cancer progression," *THE JOURNAL OF UROLOGY*, vol. 166, pp. 2472-2483, 12// 2001.

[15] J. A. Tuxhorn, G. E. Ayala, M. J. Smith, V. C. Smith, T. D. Dang, and D. R. Rowley, "Reactive stroma in human prostate cancer: Induction of myofibroblast phenotype and extracellular matrix remodeling," *CLINICAL CANCER RESEARCH*, vol. 8, pp. 2912-2923, September 1, 2002 2002.

[16] P. Chiarugi, P. Paoli, and P. Cirri, "Tumor microenvironment and metabolism in prostate cancer," *SEMINARS IN ONCOLOGY*, vol. 41, pp. 267-280, 4// 2014.

[17] G. T. Mellinger, D. Gleason, and J. Bailar, 3rd, "The histology and prognosis of prostatic cancer," *THE JOURNAL OF UROLOGY*, vol. 97, pp. 331-7, Feb 1967.

[18] D. F. Gleason and G. T. Mellinger, "Prediction of prognosis for prostatic adenocarcinoma by combined histological grading and clinical staging," *THE JOURNAL OF UROLOGY*, vol. 111, pp. 58-64, Jan 1974.

[19] J. I. Epstein, W. C. Allsbrook, M. B. Amin, L. L. Egevad, S. Bastacky, A. L. Beltran, *et al.*, "The 2005 International Society of Urological Pathology (ISUP) consensus conference on Gleason grading of prostatic carcinoma," *AMERICAN JOURNAL OF SURGICAL PATHOLOGY*, vol. 29, pp. 1228-1242, Sep 2005.

[20] J. I. Epstein, L. Egevad, M. B. Amin, B. Delahunt, J. R. Srigley, P. A. Humphrey, *et al.*, "The 2014 International Society of Urological Pathology (ISUP) consensus conference on Gleason grading of prostatic carcinoma definition of grading patterns and proposal for a new grading system," *AMERICAN JOURNAL OF SURGICAL PATHOLOGY*, vol. 40, pp. 244-252, Feb 2016.

[21] J. I. Epstein, M. J. Zelefsky, D. D. Sjoberg, J. B. Nelson, L. Egevad, C. Magi-Galluzzi, *et al.*, "A contemporary prostate cancer grading system: A validated

alternative to the Gleason score," *EUROPEAN UROLOGY,* vol. 69, pp. 428-435, Mar 2016.

[22] N. Mottet, J. Bellmunt, M. Bolla, E. Briers, M. G. Cumberbatch, M. De Santis, *et al.*, "EAU-ESTRO-SIOG guidelines on prostate cancer. Part 1: Screening, diagnosis, and local treatment with curative intent," *EUROPEAN UROLOGY,* vol. 71, pp. 618-629, Apr 2017.

[23] M. J. Barry, "Screening for prostate cancer - the controversy that refuses to die," *NEW ENGLAND JOURNAL OF MEDICINE,* vol. 360, pp. 1351-1354, Mar 26 2009.

[24] T. J. Wilt and H. U. Ahmed, "Prostate cancer screening and the management of clinically localized disease," *BRITISH MEDICAL JOURNAL,* vol. 346, p. f325, Jan 29 2013.

[25] G. L. Andriole, E. D. Crawford, R. L. Grubb, 3rd, S. S. Buys, D. Chia, T. R. Church, *et al.*, "Mortality results from a randomized prostate-cancer screening trial," *NEW ENGLAND JOURNAL OF MEDICINE,* vol. 360, pp. 1310-9, Mar 26 2009.

[26] G. L. Andriole, E. D. Crawford, R. L. Grubb, 3rd, S. S. Buys, D. Chia, T. R. Church, *et al.*, "Prostate cancer screening in the randomized prostate, lung, colorectal, and ovarian cancer screening trial: Mortality results after 13 years of follow-up," *JOURNAL OF THE NATIONAL CANCER INSTITUTE,* vol. 104, pp. 125-32, Jan 18 2012.

[27] F. H. Schroder, J. Hugosson, M. J. Roobol, T. L. Tammela, S. Ciatto, V. Nelen, *et al.*, "Screening and prostate-cancer mortality in a randomized european study," *NEW ENGLAND JOURNAL OF MEDICINE,* vol. 360, pp. 1320-8, Mar 26 2009.

[28] F. H. Schroder, J. Hugosson, M. J. Roobol, T. L. J. Tammela, M. Zappa, V. Nelen, *et al.*, "Screening and prostate cancer mortality: Results of the european randomised study of screening for prostate cancer (ERSPC) at 13 years of follow-up," *LANCET,* vol. 384, pp. 2027-2035, Dec 6 2014.

[29] P. F. Pinsky, A. Blacka, B. S. Kramer, A. Miller, P. C. Prorok, and C. Berg, "Assessing contamination and compliance in the prostate component of the prostate, lung, colorectal, and ovarian (PLCO) cancer screening trial," *CLINICAL TRIALS,* vol. 7, pp. 303-11, Aug 2010.

[30] R. M. Hoffman, "Screening for prostate cancer," *NEW ENGLAND JOURNAL OF MEDICINE,* vol. 365, pp. 2013-2019, 2011.

[31] D. J. Rosario, J. A. Lane, C. Metcalfe, J. L. Donovan, A. Doble, L. Goodwin, *et al.*, "Short term outcomes of prostate biopsy in men tested for cancer by prostate

specific antigen: Prospective evaluation within ProtecT study," *BRITISH MEDICAL JOURNAL*, vol. 344, Jan 9 2012.

[32] S. Loeb, A. Vellekoop, H. U. Ahmed, J. Catto, M. Emberton, R. Nam, *et al.*, "Systematic review of complications of prostate biopsy," *EUROPEAN UROLOGY*, vol. 64, pp. 876-92, Dec 2013.

[33] J. A. Lane, F. C. Hamdy, R. M. Martin, E. L. Turner, D. E. Neal, and J. L. Donovan, "Latest results from the UK trials evaluating prostate cancer screening and treatment: The CAP and ProtecT studies," *EUROPEAN JOURNAL OF CANCER*, vol. 46, pp. 3095-101, Nov 2010.

[34] J. L. Donovan, F. C. Hamdy, J. A. Lane, M. Mason, C. Metcalfe, E. Walsh, *et al.*, "Patient-reported outcomes after monitoring, surgery, or radiotherapy for prostate cancer," *NEW ENGLAND JOURNAL OF MEDICINE*, vol. 375, pp. 1425-1437, Oct 13 2016.

[35] F. C. Hamdy, J. L. Donovan, J. A. Lane, M. Mason, C. Metcalfe, P. Holding, *et al.*, "10-year outcomes after monitoring, surgery, or radiotherapy for localized prostate cancer," *NEW ENGLAND JOURNAL OF MEDICINE*, vol. 375, pp. 1415-1424, Oct 13 2016.

[36] K. K. Hodge, J. E. McNeal, M. K. Terris, and T. A. Stamey, "Random systematic versus directed ultrasound guided transrectal core biopsies of the prostate," *THE JOURNAL OF UROLOGY*, vol. 142, pp. 71-4; discussion 74-5, Jul 1989.

[37] K. Eichler, S. Hempel, J. Wilby, L. Myers, L. M. Bachmann, and J. Kleijnen, "Diagnostic value of systematic biopsy methods in the investigation of prostate cancer: A systematic review," *THE JOURNAL OF UROLOGY*, vol. 175, pp. 1605-12, May 2006.

[38] R. K. Nam, R. Saskin, Y. Lee, Y. Liu, C. Law, L. H. Klotz, *et al.*, "Increasing hospital admission rates for urological complications after transrectal ultrasound guided prostate biopsy," *THE JOURNAL OF UROLOGY*, vol. 183, pp. 963-8, Mar 2010.

[39] (2017, 02/05). *Rectal examination*. Available: https://en.wikipedia.org/wiki/Rectal_examination

[40] W. J. Catalona, J. P. Richie, F. R. Ahmann, M. A. Hudson, P. T. Scardino, R. C. Flanigan, *et al.*, "Comparison of digital rectal examination and serum prostate-specific antigen in the early detection of prostate-cancer - results of a multicenter clinical-trial of 6,630 men," *JOURNAL OF UROLOGY*, vol. 151, pp. 1283-1290, May 1994.

[41] J. M. Croswell, B. S. Kramer, and E. D. Crawford, "Screening for prostate cancer with PSA testing: Current status and future directions," *ONCOLOGY*, vol. 25, pp. 452-60, 463, May 2011.

[42] S. Phipps, T. H. J. Yang, F. K. Habib, R. L. Reuben, and S. A. McNeill, "Measurement of the mechanical characteristics of benign prostatic tissue: A novel method for assessing benign prostatic disease," *UROLOGY*, vol. 65, pp. 1024-1028, May 2005.

[43] S. Phipps, T. H. J. Yang, F. K. Habib, R. L. Reuben, and S. A. McNeill, "Measurement of tissue mechanical characteristics to distinguish between benign and malignant prostatic disease," *UROLOGY*, vol. 66, pp. 447-450, Aug 2005.

[44] M. Zhang, P. Nigwekar, B. Castaneda, K. Hoyt, J. V. Joseph, A. D. Agnese, *et al.*, "Quantitative characterization of viscoelastic properties of human prostate correlated with histology," *ULTRASOUND IN MEDICINE AND BIOLOGY*, vol. 34, pp. 1033-1042, Jul 2008.

[45] G. A. Holzapfel, "Biomechanics of soft tissue," *THE HANDBOOK OF MATERIALS BEHAVIOR MODELS*, vol. 3, pp. 1049-1063, 2001.

[46] B. F. Gonçalves, S. G. P. d. Campos, C. F. P. Costa, W. R. Scarano, R. M. Góes, and S. R. Taboga, "Key participants of the tumor microenvironment of the prostate: An approach of the structural dynamic of cellular elements and extracellular matrix components during epithelial–stromal transition," *ACTA HISTOCHEMICA*, vol. 117, pp. 4-13, 2015.

[47] Y. Zhang, J. Tang, H. D. Liang, F. Q. Lv, and Z. G. Song, "Transrectal real-time tissue elastography - an effective way to distinguish benign and malignant prostate tumors," *ASIAN PACIFIC JOURNAL OF CANCER PREVENTION*, vol. 15, pp. 1831-5, 2014.

[48] K. Hoyt, B. Castaneda, M. Zhang, P. Nigwekar, P. A. di Sant'Agnese, J. V. Joseph, *et al.*, "Tissue elasticity properties as biomarkers for prostate cancer," *CANCER BIOMARKERS : SECTION A OF DISEASE MARKERS*, vol. 4, pp. 213-225, 2008.

[49] D. L. Cochlin, R. H. Ganatra, and D. F. R. Griffiths, "Elastography in the detection of prostatic cancer," *CLINICAL RADIOLOGY*, vol. 57, pp. 1014-1020, 11// 2002.

[50] P. N. T. Wells and H. D. Liang, "Medical ultrasound: Imaging of soft tissue strain and elasticity," *JOURNAL OF THE ROYAL SOCIETY INTERFACE*, vol. 8, pp. 1521-1549, Nov 7 2011.

[51] J. L. Gennisson, T. Deffieux, M. Fink, and M. Tanter, "Ultrasound elastography: Principles and techniques," *DIAGNOSTIC AND INTERVENTIONAL IMAGING*, vol. 94, pp. 487-495, 5// 2013.

[52] R. G. Barr, D. Cosgrove, M. Brock, V. Cantisani, J. M. Correas, A. W. Postema, *et al.*, "WFUMB guidelines and recommendations on the clinical use of ultrasound elastography: Part 5. Prostate," *ULTRASOUND IN MEDICINE AND BIOLOGY*, vol. 43, pp. 27-48, Jan 2017.

[53] D. W. Good, G. D. Stewart, S. Hammer, P. Scanlan, W. Shu, S. Phipps, *et al.*, "Elasticity as a biomarker for prostate cancer: A systematic review," *BRITISH JOURNAL OF UROLOGY INTERNATIONAL*, vol. 113, pp. 523-534, Apr 2014.

[54] M. Tsutsumi, T. Miyagawa, T. Matsumura, T. Endo, S. Kandori, T. Shimokama, *et al.*, "Real-time balloon inflation elastography for prostate cancer detection and initial evaluation of clinicopathologic analysis," *AMERICAN JOURNAL OF ROENTGENOLOGY*, vol. 194, pp. W471-W476, Jun 2010.

[55] C. R. Giurgiu, C. Manea, N. Crisan, C. Bungardean, I. Coman, and S. M. Dudea, "Real-time sonoelastography in the diagnosis of prostate cancer," *MEDICAL ULTRASONOGRAPHY*, vol. 13, pp. 5-9, Mar 2011.

[56] R. M. S. Sigrist, J. Liau, A. E. Kaffas, M. C. Chammas, and J. K. Willmann, "Ultrasound elastography: Review of techniques and clinical applications," *THERANOSTICS*, vol. 7, pp. 1303-1329, 2017.

[57] L. Pallwein, M. Mitterberger, G. Pinggera, F. Aigner, F. Pedross, J. Gradl, *et al.*, "Sonoelastography of the prostate: Comparison with systematic biopsy findings in 492 patients," *EUROPEAN JOURNAL OF RADIOLOGY*, vol. 65, pp. 304-310, Feb 2008.

[58] L. Pallwein, M. Mitterberger, P. Struve, G. Pinggera, W. Horninger, G. Bartsch, *et al.*, "Real-time elastography for detecting prostate cancer: Preliminary experience," *BRITISH JOURNAL OF UROLOGY INTERNATIONAL*, vol. 100, pp. 42-46, Jul 2007.

[59] G. Salomon, J. Kollermann, I. Thederan, T. Schlomm, L. H. Budaus, H. Isbarn, *et al.*, "Evaluation of prostate cancer detection with real-time-elastography: A comparison with step section pathological analysis after radical prostatectomy," *EUROPEAN UROLOGY SUPPLEMENTS*, vol. 7, pp. 75-75, Mar 2008.

[60] J. Walz, M. Marcy, J. T. Pianna, S. Brunelle, G. Gravis, N. Salem, *et al.*, "Identification of the prostate cancer index lesion by real-time elastography:

Considerations for focal therapy of prostate cancer," *WORLD JOURNAL OF UROLOGY,* vol. 29, pp. 589-594, Oct 2011.

[61] M. Brock, C. von Bodman, R. J. Palisaar, B. Loppenberg, F. Sommerer, T. Deix, *et al.*, "The impact of real-time elastography guiding a systematic prostate biopsy to improve cancer detection rate: A prospective study of 353 patients," *THE JOURNAL OF UROLOGY,* vol. 187, pp. 2039-43, Jun 2012.

[62] J. F. Teng, M. Chen, Y. Gao, Y. C. Yao, L. Chen, and D. F. Xu, "Transrectal sonoelastography in the detection of prostate cancers: A meta-analysis," *BRITISH JOURNAL OF UROLOGY INTERNATIONAL,* vol. 110, pp. E614-E620, Dec 2012.

[63] B. L. Zhang, X. L. Ma, W. L. Zhan, F. P. Zhu, M. M. Li, J. Huang, *et al.*, "Real-time elastography in the diagnosis of patients suspected of having prostate cancer: A meta-analysis," *ULTRASOUND IN MEDICINE AND BIOLOGY,* vol. 40, pp. 1400-1407, Jul 2014.

[64] K. Kamoi, K. Okihara, A. Ochiai, O. Ukimura, Y. Mizutani, A. Kawauchi, *et al.*, "The utility of transrectal real-time elastography in the diagnosis of prostate cancer," *ULTRASOUND IN MEDICINE AND BIOLOGY,* vol. 34, pp. 1025-1032, Jul 2008.

[65] F. Aigner, L. Pallwein, D. Junker, G. Schafer, G. Mikuz, F. Pedross, *et al.*, "Value of real-time elastography targeted biopsy for prostate cancer detection in men with prostate specific antigen 1.25 ng/ml or greater and 4.00 ng/ml or less," *JOURNAL OF UROLOGY,* vol. 184, pp. 913-917, Sep 2010.

[66] M. Brock, C. von Bodman, F. Sommerer, B. Loppenberg, T. Klein, T. Deix, *et al.*, "Comparison of real-time elastography with grey-scale ultrasonography for detection of organ-confined prostate cancer and extra capsular extension: A prospective analysis using whole mount sections after radical prostatectomy," *BRITISH JOURNAL OF UROLOGY INTERNATIONAL,* vol. 108, pp. E217-E222, Oct 2011.

[67] Y. Zhang, J. Tang, Y. M. Li, X. Fei, F. Q. Lv, E. H. He, *et al.*, "Differentiation of prostate cancer from benign lesions using strain index of transrectal real-time tissue elastography," *EUROPEAN JOURNAL OF RADIOLOGY,* vol. 81, pp. 857-62, May 2012.

[68] M. Brock, T. Eggert, R. J. Palisaar, F. Roghmann, K. Braun, B. Löppenberg, *et al.*, "Multiparametric ultrasound of the prostate: Adding contrast enhanced ultrasound to real-time elastography to detect histopathologically confirmed cancer," *THE JOURNAL OF UROLOGY,* vol. 189, pp. 93-98, 2013.

[69] Y. Zhu, Y. Chen, T. Qi, J. Jiang, J. Qi, Y. Yu, *et al.*, "Prostate cancer detection with real-time elastography using a bi-plane transducer: Comparison with step

section radical prostatectomy pathology," *WORLD JOURNAL OF UROLOGY*, vol. 32, pp. 329-333, April 01 2014.

[70] J. M. Correas, A. M. Tissier, A. Khairoune, V. Vassiliu, A. Mejean, O. Helenon, *et al.*, "Prostate cancer: Diagnostic performance of real-time shear-wave elastography," *RADIOLOGY*, vol. 275, pp. 280-289, Apr 2015.

[71] R. G. Barr, R. Memo, and C. R. Schaub, "Shear wave ultrasound elastography of the prostate initial results," *ULTRASOUND QUARTERLY*, vol. 28, pp. 13-20, Mar 2012.

[72] S. Ahmad, R. Cao, T. Varghese, L. Bidaut, and G. Nabi, "Transrectal quantitative shear wave elastography in the detection and characterisation of prostate cancer," *SURGICAL ENDOSCOPY AND OTHER INTERVENTIONAL TECHNIQUES*, vol. 27, pp. 3280-3287, Sep 2013.

[73] K. Boehm, G. Salomon, B. Beyer, J. Schiffmann, K. Simonis, M. Graefen, *et al.*, "Shear wave elastography for localization of prostate cancer lesions and assessment of elasticity thresholds: Implications for targeted biopsies and active surveillance protocols," *JOURNAL OF UROLOGY*, vol. 193, pp. 794-800, Mar 2015.

[74] S. Woo, S. Y. Kim, J. Y. Cho, and S. H. Kim, "Shear wave elastography for detection of prostate cancer: A preliminary study," *KOREAN JOURNAL OF RADIOLOGY*, vol. 15, pp. 346-355, 6/ 2014.

[75] A. Arani, D. Plewes, A. Krieger, and R. Chopra, "The feasibility of endorectal MR elastography for prostate cancer localization," *MAGNETIC RESONANCE IN MEDICINE*, vol. 66, pp. 1649-57, Dec 2011.

[76] G. Thormer, M. Reiss-Zimmermann, J. Otto, K. T. Hoffmann, M. Moche, N. Garnov, *et al.*, "Novel technique for MR elastography of the prostate using a modified standard endorectal coil as actuator," *JOURNAL OF MAGNETIC RESONANCE IMAGING*, vol. 37, pp. 1480-5, Jun 2013.

[77] R. Chopra, A. Arani, Y. Huang, M. Musquera, J. Wachsmuth, M. Bronskill, *et al.*, "In vivo MR elastography of the prostate gland using a transurethral actuator," *MAGNETIC RESONANCE IN MEDICINE*, vol. 62, pp. 665-71, Sep 2009.

[78] D. M. McGrath, W. D. Foltz, A. Al-Mayah, C. J. Niu, and K. K. Brock, "Quasi-static magnetic resonance elastography at 7 T to measure the effect of pathology before and after fixation on tissue biomechanical properties," *MAGNETIC RESONANCE IN MEDICINE*, vol. 68, pp. 152-65, Jul 2012.

[79] J. Kemper, R. Sinkus, J. Lorenzen, C. Nolte-Ernsting, A. Stork, and G. Adam, "MR elastography of the prostate: Initial in-vivo application," *FORTSCHRITTE AUF*

DEM GEBIET DER RÖNTGENSTRAHLEN UND BILDGEBENDEN VERFAHREN, vol. 176, pp. 1094-9, Aug 2004.

[80] S. Y. Li, M. Chen, W. C. Wang, W. F. Zhao, J. Y. Wang, X. N. Zhao, *et al.*, "A feasibility study of MR elastography in the diagnosis of prostate cancer at 3.0T," *ACTA RADIOLOGICA*, vol. 52, pp. 354-358, Apr 2011.

[81] A. Arani, M. Da Rosa, E. Ramsay, D. B. Plewes, M. A. Haider, and R. Chopra, "Incorporating endorectal mr elastography into multi-parametric MRI for prostate cancer imaging: Initial feasibility in volunteers," *JOURNAL OF MAGNETIC RESONANCE IMAGING*, vol. 38, pp. 1251-60, Nov 2013.

[82] R. S. Sahebjavaher, A. Baghani, M. Honarvar, R. Sinkus, and S. E. Salcudean, "Transperineal prostate MR elastography: Initial in vivo results," *MAGNETIC RESONANCE IN MEDICINE*, vol. 69, pp. 411-420, Feb 2013.

[83] R. S. Sahebjavaher, S. Frew, A. Bylinskii, L. ter Beek, P. Garteiser, M. Honarvar, *et al.*, "Prostate MR elastography with transperineal electromagnetic actuation and a fast fractionally encoded steady-state gradient echo sequence," *NUCLEAR MAGNETIC RESONANCE IN BIOMEDICINE*, vol. 27, pp. 784-94, Jul 2014.

[84] R. S. Sahebjavaher, G. Nir, M. Honarvar, L. O. Gagnon, J. Ischia, E. C. Jones, *et al.*, "MR elastography of prostate cancer: Quantitative comparison with histopathology and repeatability of methods," *NUCLEAR MAGNETIC RESONANCE IN BIOMEDICINE*, vol. 28, pp. 124-39, Jan 2015.

[85] J. Schiffmann, M. Grindei, Z. Tian, D. J. Yassin, T. Steinwender, S. R. Leyh-Bannurah, *et al.*, "Limitations of elastography based prostate biopsy," *JOURNAL OF UROLOGY*, vol. 195, pp. 1731-1736, Jun 2016.

[86] J. Schmitt, "OCT elastography: Imaging microscopic deformation and strain of tissue," *OPTICS EXPRESS*, vol. 3, pp. 199-211, Sep 14 1998.

[87] J. G. Fujimoto, M. E. Brezinski, G. J. Tearney, S. A. Boppart, B. Bouma, M. R. Hee, *et al.*, "Optical biopsy and imaging using optical coherence tomography," *NATURE MEDICINE*, vol. 1, pp. 970-2, Sep 1995.

[88] E. C. Faria, N. Ma, E. Gazi, P. Gardner, M. Brown, N. W. Clarke, *et al.*, "Measurement of elastic properties of prostate cancer cells using afm," *ANALYST*, vol. 133, pp. 1498-500, Nov 2008.

[89] M. Lekka, D. Gil, K. Pogoda, J. Dulińska-Litewka, R. Jach, J. Gostek, *et al.*, "Cancer cell detection in tissue sections using afm," *ARCHIVES OF BIOCHEMISTRY AND BIOPHYSICS*, vol. 518, pp. 151-156, 2/15/ 2012.

[90] T. J. Harvey, E. C. Faria, A. Henderson, E. Gazi, A. D. Ward, N. W. Clarke, *et al.*, "Spectral discrimination of live prostate and bladder cancer cell lines using raman optical tweezers," *JOURNAL OF BIOMEDICAL OPTICS*, vol. 13, Nov-Dec 2008.

[91] W. Drexler and J. G. Fujimoto, *OPTICAL COHERENCE TOMOGRAPHY: TECHNOLOGY AND APPLICATIONS*: Springer, 2015.

[92] D. Huang, E. A. Swanson, C. P. Lin, J. S. Schuman, W. G. Stinson, W. Chang, *et al.*, "Optical coherence tomography," *SCIENCE*, vol. 254, pp. 1178-81, Nov 22 1991.

[93] A. F. Fercher, C. K. Hitzenberger, G. Kamp, and S. Y. Elzaiat, "Measurement of intraocular distances by backscattering spectral interferometry," *OPTICS COMMUNICATIONS*, vol. 117, pp. 43-48, May 15 1995.

[94] R. Leitgeb, C. K. Hitzenberger, and A. F. Fercher, "Performance of fourier domain vs. Time domain optical coherence tomography," *OPTICS EXPRESS*, vol. 11, pp. 889-894, Apr 21 2003.

[95] W. Drexler, "Ultrahigh-resolution optical coherence tomography," *JOURNAL OF BIOMEDICAL OPTICS*, vol. 9, pp. 47-74, Jan-Feb 2004.

[96] K. V. Larin and D. D. Sampson, "Optical coherence elastography - OCT at work in tissue biomechanics [invited]," *BIOMEDICAL OPTICS EXPRESS*, vol. 8, pp. 1172-1202, 2017/02/01 2017.

[97] Y. H. Zhao, Z. P. Chen, C. Saxer, S. H. Xiang, J. F. de Boer, and J. S. Nelson, "Phase-resolved optical coherence tomography and optical doppler tomography for imaging blood flow in human skin with fast scanning speed and high velocity sensitivity," *OPTICS LETTERS*, vol. 25, pp. 114-116, Jan 15 2000.

[98] B. F. Kennedy, S. H. Koh, R. A. McLaughlin, K. M. Kennedy, P. R. T. Munro, and D. D. Sampson, "Strain estimation in phase-sensitive optical coherence elastography," *BIOMEDICAL OPTICS EXPRESS*, vol. 3, pp. 1865-1879, Aug 1 2012.

[99] C. Li, G. Guan, X. Cheng, Z. Huang, and R. K. Wang, "Quantitative elastography provided by surface acoustic waves measured by phase-sensitive optical coherence tomography," *OPTICS LETTERS*, vol. 37, pp. 722-4, Feb 15 2012.

[100] X. Liang and S. A. Boppart, "Biomechanical properties of in vivo human skin from dynamic optical coherence elastography," *IEEE TRANSACTIONS ON BIOMEDICAL ENGINEERING*, vol. 57, pp. 953-959, Apr 2010.

[101] C. H. Li, G. Guan, Z. Huang, M. Johnstone, and R. K. Wang, "Noncontact all-optical measurement of corneal elasticity," *OPTICS LETTERS*, vol. 37, pp. 1625-1627, May 15 2012.

[102] C. Li, Z. Huang, and R. K. Wang, "Elastic properties of soft tissue-mimicking phantoms assessed by combined use of laser ultrasonics and low coherence interferometry," *OPTICS EXPRESS*, vol. 19, pp. 10153-63, May 23 2011.

[103] S. Wang, J. S. Li, R. K. Manapuram, F. M. Menodiado, D. R. Ingram, M. D. Twa, *et al.*, "Noncontact measurement of elasticity for the detection of soft-tissue tumors using phase-sensitive optical coherence tomography combined with a focused air-puff system," *OPTICS LETTERS*, vol. 37, pp. 5184-5186, Dec 15 2012.

[104] D. S. D. A. Bedford, *INTRODUCTION TO ELASTIC WAVE PROPAGATION*, 1996.

[105] S. Z. Song, Z. H. Huang, T. M. Nguyen, E. Y. Wong, B. Arnal, M. O'Donnell, *et al.*, "Shear modulus imaging by direct visualization of propagating shear waves with phase-sensitive optical coherence tomography," *JOURNAL OF BIOMEDICAL OPTICS*, vol. 18, Dec 2013.

[106] S. Z. Song, Z. H. Huang, and R. K. K. Wang, "Tracking mechanical wave propagation within tissue using phase-sensitive optical coherence tomography: Motion artifact and its compensation," *JOURNAL OF BIOMEDICAL OPTICS*, vol. 18, Dec 2013.

[107] S. Wang, A. L. Lopez, Y. Morikawa, G. Tao, J. S. Li, I. V. Larina, *et al.*, "Noncontact quantitative biomechanical characterization of cardiac muscle using shear wave imaging optical coherence tomography," *BIOMEDICAL OPTICS EXPRESS*, vol. 5, pp. 1980-1992, Jul 1 2014.

[108] M. Razani, T. W. H. Luk, A. Mariampillai, P. Siegler, T. R. Kiehl, M. C. Kolios, *et al.*, "Optical coherence tomography detection of shear wave propagation in inhomogeneous tissue equivalent phantoms and ex-vivo carotid artery samples," *BIOMEDICAL OPTICS EXPRESS*, vol. 5, pp. 895-906, Mar 1 2014.

[109] M. Razani, A. Mariampillai, C. R. Sun, T. W. H. Luk, V. X. D. Yang, and M. C. Kolios, "Feasibility of optical coherence elastography measurements of shear wave propagation in homogeneous tissue equivalent phantoms," *BIOMEDICAL OPTICS EXPRESS*, vol. 3, pp. 972-980, May 1 2012.

[110] T. M. Nguyen, S. Z. Song, B. Arnal, E. Y. Wong, Z. H. Huang, R. K. K. Wang, *et al.*, "Shear wave pulse compression for dynamic elastography using phase-sensitive optical coherence tomography," *JOURNAL OF BIOMEDICAL OPTICS*, vol. 19, Jan 2014.

[111] B. F. Kennedy, T. R. Hillman, R. A. McLaughlin, B. C. Quirk, and D. D. Sampson, "In vivo dynamic optical coherence elastography using a ring actuator," *OPTICS EXPRESS*, vol. 17, pp. 21762-72, Nov 23 2009.

[112] B. F. Kennedy, X. Liang, S. G. Adie, D. K. Gerstmann, B. C. Quirk, S. A. Boppart, *et al.*, "In vivo three-dimensional optical coherence elastography," *OPTICS EXPRESS*, vol. 19, pp. 6623-34, Mar 28 2011.

[113] K. M. Kennedy, C. Ford, B. F. Kennedy, M. B. Bush, and D. D. Sampson, "Analysis of mechanical contrast in optical coherence elastography," *JOURNAL OF BIOMEDICAL OPTICS*, vol. 18, pp. 121508-121508, 2013.

[114] A. L. Boskey, M. L. Cohen, and P. G. Bullough, "Hard tissue biochemistry - a comparison of fresh-frozen and formalin-fixed tissue samples," *CALCIFIED TISSUE INTERNATIONAL*, vol. 34, pp. 328-331, 1982.

[115] J. D. Currey, K. Brear, P. Zioupos, and G. C. Reilly, "Effect of formaldehyde fixation on some mechanical-properties of bovine bone," *BIOMATERIALS*, vol. 16, pp. 1267-1271, Nov 1995.

[116] M. Abe, M. Takahashi, K. Horiuchi, and A. Nagano, "The changes in crosslink contents in tissues after formalin fixation," *ANALYTICAL BIOCHEMISTRY*, vol. 318, pp. 118-123, 7/1/ 2003.

[117] M. Srinivasan, D. Sedmak, and S. Jewell, "Effect of fixatives and tissue processing on the content and integrity of nucleic acids," *THE AMERICAN JOURNAL OF PATHOLOGY*, vol. 161, pp. 1961-71, Dec 2002.

[118] R. J. Buesa and M. V. Peshkov, "How much formalin is enough to fix tissues?," *ANNALS OF DIAGNOSTIC PATHOLOGY*, vol. 16, pp. 202-9, Jun 2012.

[119] R. Eisma, C. Lamb, and R. W. Soames, "From formalin to Thiel embalming: What changes? One anatomy department's experiences," *CLINICAL ANATOMY*, vol. 26, pp. 564-71, Jul 2013.

[120] K. D. Wolff, M. Kesting, T. Mucke, A. Rau, and F. Holzle, "Thiel embalming technique: A valuable method for microvascular exercise and teaching of flap raising," *MICROSURGERY*, vol. 28, pp. 273-8, 2008.

[121] W. Thiel, "Ergänzung für die konservierung ganzer leichen nach W. Thiel," *ANNALS OF ANATOMY - ANATOMISCHER ANZEIGER*, vol. 184, pp. 267-269, 5// 2002.

[122] D. G. McLeod, D. R. Eisma, A. Schwab, P. G. Corner, P. R. Soames, and D. S. Cochran, "An evaluation of Thiel-embalmed cadavers for ultrasound-based regional anaesthesia training and research," *ULTRASOUND*, vol. 18, pp. 125-129, 2010.

[123] S. Eljamel, A. Volovick, T. Saliev, R. Eisma, and A. Melzer, "Evaluation of thiel cadaveric model for MRI-guided stereotactic procedures in neurosurgery," *SURGICAL NEUROLOGY INTERNATIONAL*, vol. 5, pp. S404-9, 2014.

[124] J. McElhaney, J. Fogle, E. Byars, and G. Weaver, "Effect of embalming on the mechanical properties of beef bone," *JOURNAL OF APPLIED PHYSIOLOGY,* vol. 19, pp. 1234-6, Nov 1964.

[125] E. D. Sedlin, "A rheologic model for cortical bone. A study of the physical properties of human femoral samples," *ACTA ORTHOPAEDICA SCANDINAVICA. SUPPLEMENTUM,* pp. Suppl 83:1-77, 1965.

[126] J. C. H. Goh, E. J. Ang, and K. Bose, "Effect of preservation medium on the mechanical-properties of cat bones," *ACTA ORTHOPAEDICA SCANDINAVICA,* vol. 60, pp. 465-467, Aug 1989.

[127] C. I. C. Tan., S. Dunn., G. N. Kent., A. G. Randall., S. J. Edmondston., and K. P. Singer., "Does formalin-fixation alter the extent of collagen and elastin crosslinks in human spinal intervertebral discs and ligamentum flava?," *JOURNAL OF MUSCULOSKELETAL RESEARCH,* vol. 6, pp. 89-99, 2002.

[128] H. Kikugawa and T. Asaka, "Effect of long-term formalin preservation on the bending properties and fracture toughness of bovine compact bone," *JOURNAL OF THE JAPAN INSTITUTE OF METALS,* vol. 69, pp. 267-271, Feb 2005.

[129] G. J. Tearney, M. E. Brezinski, J. F. Southern, B. E. Bouma, S. A. Boppart, and J. G. Fujimoto, "Optical biopsy in human urologic tissue using optical coherence tomography," *JOURNAL OF UROLOGY,* vol. 157, pp. 1915-1919, May 1997.

[130] A. V. D'Amico, M. Weinstein, X. D. Li, J. P. Richie, and J. Fujimoto, "Optical coherence tomography as a method for identifying benign and malignant microscopic structures in the prostate gland," *UROLOGY,* vol. 55, pp. 783-787, May 2000.

[131] J. Welzel, "Optical coherence tomography in dermatology: A review," *SKIN RESEARCH AND TECHNOLOGY,* vol. 7, pp. 1-9, Feb 2001.

[132] R. C. Chan, A. H. Chau, W. C. Karl, S. Nadkarni, A. S. Khalil, N. Iftimia, *et al.*, "OCT-based arterial elastography: Robust estimation exploiting tissue biomechanics," *OPTICS EXPRESS,* vol. 12, pp. 4558-4572, Sep 20 2004.

[133] J. Rogowska, N. A. Patel, J. G. Fujimoto, and M. E. Brezinski, "Optical coherence tomographic elastography technique for measuring deformation and strain of atherosclerotic tissues," *HEART,* vol. 90, pp. 556-62, May 2004.

[134] P. H. Tomlins and R. K. Wang, "Theory, developments and applications of optical coherence tomography," *JOURNAL OF PHYSICS D-APPLIED PHYSICS,* vol. 38, pp. 2519-2535, Aug 7 2005.

[135] R. K. K. Wang, Z. H. Ma, and S. J. Kirkpatrick, "Tissue doppler optical coherence elastography for real time strain rate and strain mapping of soft tissue," *APPLIED PHYSICS LETTERS*, vol. 89, Oct 2 2006.

[136] H. J. Ko, W. Tan, R. Stack, and S. A. Boppart, "Optical coherence elastography of engineered and developing tissue," *TISSUE ENGINEERING*, vol. 12, pp. 63-73, Jan 2006.

[137] S. J. Kirkpatrick, R. K. Wang, and D. D. Duncan, "OCT-based elastography for large and small deformations," *OPTICS EXPRESS*, vol. 14, pp. 11585-97, Nov 27 2006.

[138] R. K. Wang, S. Kirkpatrick, and M. Hinds, "Phase-sensitive optical coherence elastography for mapping tissue microstrains in real time," *APPLIED PHYSICS LETTERS*, vol. 90, p. 164105, 2007.

[139] X. Liang, A. L. Oldenburg, V. Crecea, E. J. Chaney, and S. A. Boppart, "Optical micro-scale mapping of dynamic biomechanical tissue properties," *OPTICS EXPRESS*, vol. 16, pp. 11052-65, Jul 21 2008.

[140] A. F. Fercher, "Optical coherence tomography - development, principles, applications," *ZEITSCHRIFT FUR MEDIZINISCHE PHYSIK*, vol. 20, pp. 251-276, 2010.

[141] C. Sun, B. Standish, and V. X. Yang, "Optical coherence elastography: Current status and future applications," *JOURNAL OF BIOMEDICAL OPTICS*, vol. 16, p. 043001, Apr 2011.

[142] R. K. Wang and A. L. Nuttall, "Phase-sensitive optical coherence tomography imaging of the tissue motion within the organ of Corti at a subnanometer scale: A preliminary study," *JOURNAL OF BIOMEDICAL OPTICS*, vol. 15, p. 056005, Sep-Oct 2010.

[143] C. Li, G. Guan, Y. Ling, Y. T. Hsu, S. Song, J. T. Huang, *et al.*, "Detection and characterisation of biopsy tissue using quantitative optical coherence elastography (OCE) in men with suspected prostate cancer," *CANCER LETTERS*, vol. 357, pp. 121-8, Feb 1 2015.

[144] C. Li, G. Guan, R. Reif, Z. Huang, and R. K. Wang, "Determining elastic properties of skin by measuring surface waves from an impulse mechanical stimulus using phase-sensitive optical coherence tomography," *JOURNAL OF THE ROYAL SOCIETY INTERFACE*, vol. 9, pp. 831-41, May 7 2012.

[145] S. Chen, M. W. Urban, C. Pislaru, R. Kinnick, and J. F. Greenleaf, "Liver elasticity and viscosity quantification using shearwave dispersion ultrasound vibrometry (SDUV)," in *CONFERENCE PROCEEDINGS : ANNUAL INTERNATIONAL*

CONFERENCE OF THE IEEE ENGINEERING IN MEDICINE AND BIOLOGY SOCIETY., Minneapolis, MN, 2009, pp. 2252-5.

[146] N. Frulio and H. Trillaud, "Ultrasound elastography in liver," *DIAGNOSTIC AND INTERVENTIONAL IMAGING*, vol. 94, pp. 515-534, 5// 2013.

[147] A. Chandra, "Study of damage to peripheral nerves caused by anaesthetic needles during regional anaesthesia.," MSc by Research A thesis for the degree of MSc, University of Dundee, 2014.

[148] R. Arora, M. O. Koch, J. N. Eble, T. M. Ulbright, L. Li, and L. Cheng, "Heterogeneity of Gleason grade in multifocal adenocarcinoma of the prostate," *CANCER*, vol. 100, pp. 2362-6, Jun 1 2004.

[149] G. W. Chien, J. M. Slezak, T. N. Harrison, H. Jung, J. S. Gelfond, C. Zhang, *et al.*, "Health-related quality of life outcomes from a contemporary prostate cancer registry in a large diverse population," *BRITISH JOURNAL OF UROLOGY INTERNATIONAL*, Apr 19 2017.

[150] J. F. Waljee, E. S. Hu, L. A. Newman, and A. K. Alderman, "Predictors of re-excision among women undergoing breast-conserving surgery for cancer," *ANNALS OF SURGICAL ONCOLOGY*, vol. 15, pp. 1297-303, May 2008.

[151] N. Cabioglu, K. K. Hunt, A. A. Sahin, H. M. Kuerer, G. V. Babiera, S. E. Singletary, *et al.*, "Role for intraoperative margin assessment in patients undergoing breast-conserving surgery," *ANNALS OF SURGICAL ONCOLOGY*, vol. 14, pp. 1458-71, Apr 2007.

[152] A. L. Nunez, G. A. Giannico, F. Mukhtar, V. Dailey, R. El-Galley, and O. Hameed, "Frozen section evaluation of margins in radical prostatectomy specimens: A contemporary study and literature review," *ANNALS OF DIAGNOSTIC PATHOLOGY*, vol. 24, pp. 11-8, Oct 2016.

[153] F. T. Nguyen, A. M. Zysk, E. J. Chaney, J. G. Kotynek, U. J. Oliphant, F. J. Bellafiore, *et al.*, "Intraoperative evaluation of breast tumor margins with optical coherence tomography," *CANCER RESEARCH*, vol. 69, pp. 8790-6, Nov 15 2009.

[154] A. S. Haka, Z. Volynskaya, J. A. Gardecki, J. Nazemi, J. Lyons, D. Hicks, *et al.*, "In vivo margin assessment during partial mastectomy breast surgery using raman spectroscopy," *CANCER RESEARCH*, vol. 66, pp. 3317-22, Mar 15 2006.

[155] M. H. Zaman, L. M. Trapani, A. L. Sieminski, D. Mackellar, H. Gong, R. D. Kamm, *et al.*, "Migration of tumor cells in 3D matrices is governed by matrix stiffness along with cell-matrix adhesion and proteolysis," in *PROCEEDINGS OF THE*

NATIONAL ACADEMY OF SCIENCES OF THE UNITED STATES OF AMERICA, 2006, pp. 10889-94.

[156] J. Tang, Y. Zhang, M. B. Zhang, Y. M. Li, X. Fei, and Z. G. Song, "Tissue elasticity displayed by elastography and its correlation with the characteristics of collagen type I and type III in prostatic stroma," *ASIAN JOURNAL OF ANDROLOGY*, vol. 16, pp. 305-8, Mar-Apr 2014.

[157] K. M. Kennedy, B. F. Kennedy, R. A. McLaughlin, and D. D. Sampson, "Needle optical coherence elastography for tissue boundary detection," *OPTICS LETTERS*, vol. 37, pp. 2310-2312, 2012/06/15 2012.

[158] A. H. Chau, R. C. Chan, M. Shishkov, B. MacNeill, N. Iftimia, G. J. Tearney, *et al.*, "Mechanical analysis of atherosclerotic plaques based on optical coherence tomography," *ANNALS OF BIOMEDICAL ENGINEERING*, vol. 32, pp. 1494-503, Nov 2004.

[159] N. Sheikh, C. Wei, M. Szewczyk-Bieda, A. Campbell, S. Memon, S. Lang, *et al.*, "Combined T2 and diffusion-weighted MR imaging with template prostate biopsies in men suspected with prostate cancer but negative transrectal ultrasound-guided biopsies," *WORLD JOURNAL OF UROLOGY*, vol. 35, pp. 213-220, Feb 2017.

[160] Y. Ling, C. Li, K. Feng, R. Duncan, R. Eisma, Z. Huang, *et al.*, "Effects of fixation and preservation on tissue elastic properties measured by quantitative optical coherence elastography (OCE)," *JOURNAL OF BIOMECHANICS*, vol. 49, pp. 1009-1015, May 03 2016.

[161] M. D. Shoulders and R. T. Raines, "Collagen structure and stability," *ANNUAL REVIEW OF BIOCHEMISTRY*, vol. 78, pp. 929-58, 2009.

[162] E. Sadoun, "Collagen I: A potential therapeutic target for prostate cancer," in *QATAR FOUNDATION ANNUAL RESEARCH FORUM PROCEEDINGS*, 2013, p. BIOP 0205.

[163] N. Burns-Cox, N. C. Avery, J. C. Gingell, and A. J. Bailey, "Changes in collagen metabolism in prostate cancer: A host response that may alter progression," *THE JOURNAL OF UROLOGY*, vol. 166, pp. 1698-701, Nov 2001.

[164] C. Morrison, J. Thornhill, and E. Gaffney, "The connective tissue framework in the normal prostate, BPH and prostate cancer: Analysis by scanning electron microscopy after cellular digestion," *UROLOGICAL RESEARCH*, vol. 28, pp. 304-7, Oct 2000.

[165] D. A. Barron and D. R. Rowley, "The reactive stroma microenvironment and prostate cancer progression," *ENDOCRINE-RELATED CANCER*, vol. 19, pp. R187-204, Dec 2012.

[166] M. W. Conklin, J. C. Eickhoff, K. M. Riching, C. A. Pehlke, K. W. Eliceiri, P. P. Provenzano, *et al.*, "Aligned collagen is a prognostic signature for survival in human breast carcinoma," *THE AMERICAN JOURNAL OF PATHOLOGY*, vol. 178, pp. 1221-32, Mar 2011.

[167] P. Provenzano, K. Eliceiri, J. Campbell, D. Inman, J. White, and P. Keely, "Collagen reorganization at the tumor-stromal interface facilitates local invasion," *BIOMED CENTRAL MEDICINE*, vol. 4, pp. 1-15, 2006/12/26 2006.

[168] P. Campagnola, "Second harmonic generation imaging microscopy: Applications to diseases diagnostics," *ANALYTICAL CHEMISTRY*, vol. 83, pp. 3224-3231, 2011.

[169] A. Keikhosravi, J. S. Bredfeldt, A. K. Sagar, and K. W. Eliceiri, "Second-harmonic generation imaging of cancer," *METHODS IN CELL BIOLOGY*, vol. 123, pp. 531-546, 2014.

[170] T. M. Bauman, T. M. Nicholson, L. L. Abler, K. W. Eliceiri, W. Huang, C. M. Vezina, *et al.*, "Characterization of fibrillar collagens and extracellular matrix of glandular benign prostatic hyperplasia nodules," *PUBLIC LIBRARY OF SCIENCE ONE*, vol. 9, p. e109102, 10/02 2014.

[171] Y. Huang and Z. Zhuang, "Second harmonic microscopic imaging and spectroscopic characterization in prostate pathological tissue," *SCANNING*, vol. 36, pp. 334-7, May-Jun 2014.

[172] P. J. Campagnola, A. C. Millard, M. Terasaki, P. E. Hoppe, C. J. Malone, and W. A. Mohler, "Three-dimensional high-resolution second-harmonic generation imaging of endogenous structural proteins in biological tissues," *BIOPHYSICAL JOURNAL*, vol. 82, pp. 493-508, Jan 2002.

[173] R. M. Williams, W. R. Zipfel, and W. W. Webb, "Interpreting second-harmonic generation images of collagen i fibrils," *BIOPHYSICAL JOURNAL*, vol. 88, pp. 1377-1386, Feb 2005.

[174] R. A. R. Rao, M. R. Mehta, and K. C. Toussaint, "Fourier transform-second-harmonic generation imaging of biological tissues," *OPTICS EXPRESS*, vol. 17, pp. 14534-14542, 2009/08/17 2009.

[175] P. Matteini, F. Ratto, F. Rossi, R. Cicchi, C. Stringari, D. Kapsokalyvas, *et al.*, "Photothermally-induced disordered patterns of corneal collagen revealed by shg imaging," *OPTICS EXPRESS*, vol. 17, pp. 4868-78, Mar 16 2009.

[176] R. Ambekar, T.-Y. Lau, M. Walsh, R. Bhargava, and K. C. Toussaint, "Quantifying collagen structure in breast biopsies using second-harmonic generation imaging," *BIOMEDICAL OPTICS EXPRESS*, vol. 3, pp. 2021-2035, 2012/09/01 2012.

[177] P. Matteini, R. Cicchi, F. Ratto, D. Kapsokalyvas, F. Rossi, M. de Angelis, *et al.*, "Thermal transitions of fibrillar collagen unveiled by second-harmonic generation microscopy of corneal stroma," *BIOPHYSICAL JOURNAL*, vol. 103, pp. 1179-87, Sep 19 2012.

[178] R. Cicchi, D. Kapsokalyvas, M. Troiano, P. Campolmi, C. Morini, D. Massi, *et al.*, "In vivo non-invasive monitoring of collagen remodelling by two-photon microscopy after micro-ablative fractional laser resurfacing," *JOURNAL OF BIOPHOTONICS*, vol. 7, pp. 914-25, Nov 2014.

[179] P. Pantazis, J. Maloney, D. Wu, and S. E. Fraser, "Second harmonic generating (SHG) nanoprobes for in vivo imaging," in *PROCEEDINGS OF THE NATIONAL ACADEMY OF SCIENCES OF THE UNITED STATES OF AMERICA*, 2010, pp. 14535-14540.

[180] R. Ambekar, "Quantification of collagen fiber organization in biological tissues at cellular and molecular scales using second-harmonic generation imaging," University of Illinois at Urbana-Champaign, 2012.

[181] I. Freund, M. Deutsch, and A. Sprecher, "Connective tissue polarity. Optical second-harmonic microscopy, crossed-beam summation, and small-angle scattering in rat-tail tendon," *BIOPHYSICAL JOURNAL*, vol. 50, pp. 693-712, Oct 1986.

[182] A. T. Yeh, N. Nassif, A. Zoumi, and B. J. Tromberg, "Selective corneal imaging using combined second-harmonic generation and two-photon excited fluorescence," *OPTICS LETTERS*, vol. 27, pp. 2082-2084, 2002/12/02 2002.

[183] S.-P. Tai, T.-H. Tsai, W.-J. Lee, D.-B. Shieh, Y.-H. Liao, H.-Y. Huang, *et al.*, "Optical biopsy of fixed human skin with backward-collected optical harmonics signals," *OPTICS EXPRESS*, vol. 13, pp. 8231-8242, 2005/10/03 2005.

[184] A. Zoumi, X. Lu, G. S. Kassab, and B. J. Tromberg, "Imaging coronary artery microstructure using second-harmonic and two-photon fluorescence microscopy," *BIOPHYSICAL JOURNAL*, vol. 87, pp. 2778-2786, 2004/10/01/ 2004.

[185] A.-M. Pena, A. Fabre, D. Débarre, J. Marchal-Somme, B. Crestani, J.-L. Martin, *et al.*, "Three-dimensional investigation and scoring of extracellular matrix remodeling during lung fibrosis using multiphoton microscopy," *MICROSCOPY RESEARCH AND TECHNIQUE*, vol. 70, pp. 162-170, 2007.

[186] C. Odin, Y. Le Grand, A. Renault, L. Gailhouste, and G. Baffet, "Orientation fields of nonlinear biological fibrils by second harmonic generation microscopy," *JOURNAL OF MICROSCOPY*, vol. 229, pp. 32-38, 2008.

[187] M. J. Sherratt, "Tissue elasticity and the ageing elastic fibre," *AGE (DORDR)*, vol. 31, pp. 305-25, Dec 2009.

[188] W. S. Costa, A. M. de Carvalho, M. A. Babinski, M. A. Chagas, and F. J. B. Sampaio, "Volumetric density of elastic and reticular fibers in transition zone of controls and patients with benign prostatic hyperplasia," *UROLOGY*, vol. 64, pp. 693-697, 2004.

[189] K. R. Levental, H. Yu, L. Kass, J. N. Lakins, M. Egeblad, J. T. Erler, *et al.*, "Matrix crosslinking forces tumor progression by enhancing integrin signaling," *CELL*, vol. 139, pp. 891-906, 2009.

[190] Y. Ling, C. Li, K. Feng, S. Palmer, P. L. Appleton, S. Lang, *et al.*, "Second harmonic generation (SHG) imaging of cancer heterogeneity in ultrasound guided biopsies of prostate in men suspected with prostate cancer," *JOURNAL OF BIOPHOTONICS*, vol. 10, pp. 911-918, Jun 2017.

[191] Y. Ling, C. Li, K. Zhou, G. Guan, P. L. Appleton, S. Lang, *et al.*, "Microscale characterization of prostate biopsies tissues using optical coherence elastography and second harmonic generation imaging," *LABORATORY INVESTIGATION*, 2017.